Structure Formation Mechanism of Isoporous Block copolymer Membranes

Dissertation

zur Erlangung des Grades
eines Doktors der Naturwissenschaften
(Dr. rer. nat)
am Lehrstuhl für Physikalische Chemie I
der Fakultät für Biologie, Chemie und Geowissenschaften
der Universität Bayreuth

vorgelegt von

Dipl.-Chem. Corinna Stegelmeier
geboren in Buxtehude

Bayreuth, 2015

Die vorliegende Arbeit wurde in der Zeit von Juli 2010 bis Oktober 2014 in Bayreuth am Lehrstuhl für Physikalische Chemie I unter Betreuung von Herrn Professor Dr. Stephan Förster angefertigt.

Vollständiger Abdruck der von der Fakultät für Biologie, Chemie und Geowissenschaften der Universität Bayreuth genehmigten Dissertation zur Erlangung des akademischen Grades Doktor der Naturwissenschaften (Dr. rer. nat.).

Dissertation eingereicht am:	20.03.2015
Zulassung durch die Promotionskommission:	26.03.2015
Wissenschaftliches Kolloquium:	23.07.2015

Amtierender Dekan: Prof. Dr. Rhett Kempe

Prüfungsausschuss:

Prof. Dr. Stephan Förster	(Erstgutachter)
Prof. Dr. Hans-Werner Schmidt	(Zweitgutachter)
Prof. Dr. Birgit Weber	(Vorsitz)
Prof. Dr. Matthias Breuning	

Contents

Summary

This thesis deals with the microphase separation of poly(styrene-*b*-vinylpyridine) block copolymers in highly concentrated solutions induced by evaporation of a binary solvent mixture of a high and low boiling solvent.

During self-assembly and non-solvent induced phase separation by immersion in water, asymmetric membranes consisting of a thin top layer with closely packed pore channels with diameters below 100 nm above a much thicker macroporous supporting layer are formed. These membranes can be used for filtration purposes of, e.g., biomolecules. The aim of this thesis was to discover the fundamental principles according to which these materials are developed in order to optimize the preparation conditions for future large-scale membrane productions.

The first part of the thesis focused on the experimental and theoretical investigation of the compositional changes of the polymer/binary solvent mixture during evaporation. The calculated polymer/solvent volume fractions were used to construct compositional trajectories in a ternary phase diagram. The calculations revealed a peculiar region of the phase diagram where the PVP-volume fraction is sufficiently high to induce morphological transitions. The block copolymer morphologies resulting from microphase separation in this region were systematically investigated by AFM and SEM as a function of polymer concentration, solvent composition and evaporation times before immersion in water. Several characteristic morphologies during solvent evaporation were identified, such as spinodal networks (SpN), sphere percolation networks (SN), disordered cylinders (DC) and the desired highly symmetric pore network (PN). A general structure growth during film formation was observed and further confirmed by *in situ* synchrotron SAXS measurements.

From these investigations basic conclusions for optimized membrane preparation in terms of solvent and polymer composition and immersion times could be drawn. Porous membrane formation was shown to occur only in semi-dilution (polymer concentration 20wt.% or larger) where polymer-polymer interactions dominate instead of solvent-polymer interactions. Furthermore, the starting amount of THF should be high to follow a trajectory crossing the PN phase in a broad time frame.

Using a newly designed automatic film casting apparatus, the kinetics of ordered pore formation in the evaporating polymer film could be monitored *in situ* by synchrotron SAXS. Effects of molecular weight and relative composition of the block copolymer were investigated and gen-

eral similarities of the membrane formation process discovered. All kinetic studies revealed an exponential growth of the characteristic domain size until a saturation limit was reached. In a reduced plot using characteristic growth times and domain sizes for each of the block copolymers, all kinetic data as well as a theoretical prediction for two-dimensional domain growth superimposed onto a single curve. This also applied to block copolymer systems with added Cu^{2+}-salts which served to stabilize the pore structure. Only a slight compaction of the domains due to coordinative bonding of the metal cations to the vinylpyridine groups was observed. Also the water immersion process was investigated with the help of an inkjet printer. A rapid increase of the characteristic length scale to the saturation value of the above described evaporation experiments was observed. The expected freezing of the polymer domains did not occur, likely due to an insufficient excess of water which is necessary to completely trap the developing structure.

Finally, a route to nanocomposite membranes consisting of PS-PVP and inorganic nanoparticles was investigated with the example of Fe_2O_3-nanoparticles. To compatibilize the nanoparticles with either the PS- or the PVP-domains, the nanoparticles were coated with end-functionalized PS or PVP using a recently established ligand exchange procedure. Also mixed PS/PVP-compositions were used to investigate possible locations in the PS/PVP-interface. The addition of nanoparticles lead to a surprising stabilization of the desired cylindrical pore membrane structure. TEM-images showed the nanoparticles to be located in the PS- or PVP-domains depending on the type of coating. All particles with mixed shell compositions were located near the domain interface. Interestingly, the PVP-coated nanoparticles were depleted from the thin cylindrical pores in the top layer due to a size exclusion effect.

Future studies should focus on the *in situ* SAXS measurements. It would be interesting to perform experiments in grazing incidence configuration in order to get more detailed information about the top layer morphological changes discussed above. So far only transmission scattering patterns with information from the whole inhomogeneous film cross section were collected. Improved method to mimic the water bath in an *in situ* measurement should be developed.

Concerning the nanocomposite membranes, the next step would be to increase the nanoparticle concentration and try to find a way to place the particles in the pore channels close to the film surface.

Zusammenfassung

Diese Arbeit behandelt das Thema der Mikrophasenseparation von Poly(styrol-*b*-vinylpyridin)-Blockcopolymeren in hochkonzentrierten Lösungen eines binären Gemischs aus einem hoch- und einem niedrigsiedenden organischen Lösungsmittel.
Die Bildung asymmetrischer Blockcopolymermembranen erfolgt in einem Kombinationsprozess aus Selbstorganisation und Phaseninversion durch Eintauchen in ein Nicht-Lösungsmittel. Die auf diese Weise entstandenen Membranen besitzen eine asymmetrische Struktur aus einer dünnen, hochporösen Oberfläche mit dicht gepackten cylindrischen Poren, die durch eine grobe und viel dickere Schwammstruktur gestützt wird. Anwendung finden diese Materialien z.B. bei der Filtration von Biomolekülen. Das Ziel dieser Arbeit war es, die Umstände unter denen diese Membranen gebildet werden zu verstehen, um die Präparationsbedingungen für die Herstellung im Industrie-Format zu optimieren.
Im ersten Teil der Arbeit wurden die Änderungen der Zusammensetzung der Casting-Lösung während der Verdampfung des Lösemittels sowohl theoretisch als auch experimentell ermittelt. Berechnete Polymer Volumenanteile wurden zur Konstruktion von Verdampfungslinien in einem ternären Phasendiagramm genutzt, welches einen interessanten Bereich enthüllte, in dem der Volumenanteil des hydrophileren PVP-Blocks hoch genug ist, um Phasenübergänge zu induzieren. Dieser Bereich wurde mittels AFM und SEM unter Variation der Polymerkonzentration, der Lösungsmittelzusammensetzung und der Verdampfungszeit vor der Immersion in Wasser systematisch untersucht. Die Existenz verschiedener charakteristischer Morphologien während der Verdampfung des Lösungsmittels wurde bewiesen. Unter anderem trat ein spinodales Netzwerk (SpN) und ein sphärisches Perkolationsnetzwerk (SN) sowie ungeordnete Zylinder (DC) und das bei der Membranproduktion angestrebte hochsymmetrische Netzwerk aus geordneten Poren (PN) auf.
Aus diesen Ergebnissen konnten einige grundlegende Prinzipien für die Membranpräparation bezüglich der Polymerkonzentration, der Lösungsmittelzusammensetzung und der Immersionszeit abgeleitet werden. Membranen entstehen nur im halb-verdünnten Konzentrationsbereich, wenn Polymer-Lösungsmittel-Wechselwirkungen vernachlässigbar und Polymer-Polymer-Wechselwirkungen wichtig werden. Das Lösungsmittelgemisch sollte mehrheitlich aus THF bestehen, um ein Durchschreiten der PN-Phase in einem möglichst breiten Zeitfenster zu garantieren.

Mithilfe eines neu entwickelten Apparates zur automatischen Herstellung von Polymerfilmen wurde im zweiten Teil der Arbeit die Kinetik der Membranbildung im verdampfenden Polymerfilm *in situ* mit Röntgenkleinwinkelstreuung an einer Synchrotronquelle untersucht. Der Einfluss verschiedener Paprameter, wie Molekulargewicht und Blockcopolymer-Zusammensetzung, wurde erwittelt und eine allgemeine Ähnlichkeit zwischen den einzelnen Verdampfungsreihen entdeckt, da bei allen Experimenten ein exponentielles Domänen-Wachstum auf einen Sättigungswert d_∞ gefunden wurde. In einem reduzierten Plot mithilfe der charakteristischen Wachstumszeit und dem Sättigungswert für jedes Blockcopolymer wurde die Ähnlichkeit zwischen den Messreihen gezeigt, als diese zusammen mit einer theoretisch berechneten Kurve für zweidimensionales Domänenwachstum zu einer Kurve verschmolzen.
Auch Lösungen, die Kupfer(II)-Ionen enthielten, folgten diesem Schema und wiesen lediglich eine leichte Verdichtung der Domänen auf, die auf die koordinativen Bindungen zwischen den Stickstoffatomen des Vinylpyridin-Blocks und den Kupferionen zurückgeführt wurde.
Die Immersion in ein Wasserbad wurde mithilfe einer Inkjet Druckerpatrone ebenfalls simuliert. Zu beobachten war lediglich ein sprunghafter Anstieg der Domänengröße im Moment der Immersion, allerdings blieb die erwartete Fixierung der Porenstruktur aus. Dies wurde mit einer unzureichenden Wassermenge begründet und verdeutlicht die Relevanz der Wasser Immersion im Membran-Herstellungsprozess.
Schließlich wurde ein Weg zu Nanocompositmembranen bestehend aus PS-PVP und anorganischen Nanopartikeln vorgestellt. Um eine Einlagerung von Fe_2O_3-Nanopartikeln in eine ausgewählte Polymerdomäne zu erreichen, wurden die Partikel mit einem end-funktionalisierten Homopolymer der entsprechenden Domäne in einem neu etablierten Ligandenaustausch-Verfahren beschichtet.
Auch Nanopartikel mit einer gemischten Schalenzusammensetzung wurden auf diese Weise verwendet, um die Platzierung in der Domänen-Grenzfläche zu untersuchen.
Die Zugabe von Nanopartikeln bei der Membranpräparation erwirkte eine überraschende Stabilisierung der Porenstruktur. TEM-Aufnahmen bewiesen eine eindeutige Abhängigkeit der Positionierung der Nanopartikel von der Polymer-Hülle, wobei sich alle Partikel mit gemischter Schalenzusammensetzung in der Domänengrenzfläche angesammelt hatten. Auffällig war außerdem, dass die PVP-beschichteten Nanopartikel aus den Porenkanälen nahe der Oberfläche verdrängt wurden und sich ausschließlich in den größeren Domänen im Inneren des Films angelagert haben, was auf einen Größenausschlusseffekt zurückgeführt wurde.

Weiterführende Arbeiten sollten sich zuerst auf die *in situ* SAXS-Messungen konzentrieren. Experimente unter streifendem Einfall könnten Aufschluss über die Morphologie-Übergänge in der obersten Schicht der trocknenden Polymerlösung geben. Bisher wurden lediglich Transmissions Experimente durchgeführt, die einen hohen Streuhintergrund nach sich ziehen und auf diese Weise Informationen überdecken könnten. Des Weiteren ist die Optimierung der Untersuchung des Immersionsprozesses ein sinnvoller Ansatz, da dieser eine große Relevanz im Membranherstellungs Prozess darstellt.
Im Bereich der Nanocomposit Membranen ist der nächste Schritt die Erhöhung des Partikelgehalts sowie die Beladung der dünnen Porenkanäle besonders im Hinblick auf die Anwendungsmöglichkeiten dieser Materialien.

Glossary

AFM	Atomic Force Microscopy
BCC	Body Centered Cubic
CNTs	Carbon Nanotubes
CTAB	Cetyltrimethylammonium bromide
DC	Disordered Cylinders
DETA	Diethylenetriamine
DLS	Dynamic Light Scattering
DMF	*N,N*-Dimethylformamide
DNA	Desoxyribonucleic Acid
FCC	Face Centered Cubic
GISAXS	Grazing Incidence Small Angle X-ray Scattering
HEMA	Hydroxyethyl methacrylate
HEX	Hexagonally packed Cylinders
HSAB	Hard and Soft Acids and Bases
LAM	Lamellae
LAP	Living Anionic Polymerization
OMC	Ordered Mesoporous Carbons
OC	Ordered Cylinders
P2VP	Poly-2-vinylpyridine
P3HT	Poly-3-hexylthiophene
PCL	Poly(ϵ-caprolactone)
PDMAEMA	Poly(*N,N*-dimethylaminoethyl methacrylate
PEHA	Pentaethylenehexamine
PEO	Polyethylene oxide
PINC	Polymer-Inorganic Nanocomposites
PI-PS-P4VP	Poly(isoprene-*block*-styrene-*block*-4-vinylpyridine)
PMMA	Poly(methyl methacrylate)
PN	Ordered Pore Network
PNiPAM	Poly(*N*-isopropylacrylamide)
PPO	Polypropylene oxide

$PS_3 - PMOS_3 - PI_3$	(polystyrene)$_3$-(poly(4-methoxystyrene))$_3$-(polyisoprene)$_3$
PS-P2VP	Poly(styrene-*block*-2-vinylpyridine)
PS-P2VP-PEO	Poly(styrene-*block*-2-vinylpyridine-*block*-ethylene oxide)
PS-P4VP	Poly(styrene-*block*-4-vinylpyridine)
SANS	Small-angle Neutron Scattering
SAXS	Small-angle X-ray Scattering
SEM	Scanning Electron Microscopy
SN	Sphere Percolation Network
SpN	Spinodal Network
SSL	Strong Segregation Limit
TEM	Transmission Electron Microscopy
TEOS	Tetraethyl orthosilicate
TGA	Thermogravimetric Analysis
THF	Tetrahydrofuran
WSL	Weak Segregation Limit

1 Introduction

Self-assembly is a phenomenon found in every person's life in many different areas. Nature provides a large variety of complex examples both visible and invisible to the naked eye. The way migratory birds or a school of fish arrange are two of many examples on a very large dimension. Soap bubbles produced by laundry or dish detergent also are a phenomenon of self-assembly, obtained when bringing any kind of soap in contact with water.

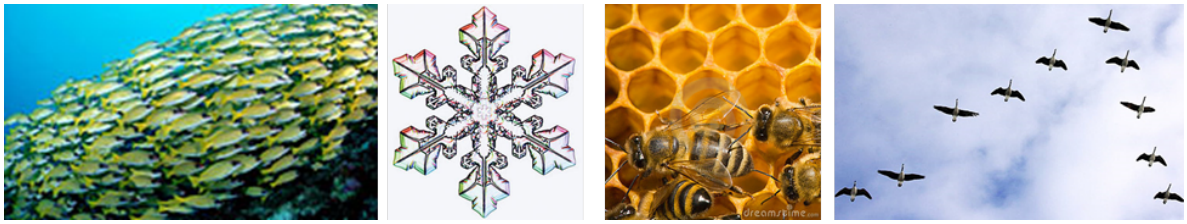

Figure 1.1. Common examples of self-assembly found in nature. A school of fish, a snow flake, a honeycomb as well as the flying conformation of migratory birds all underlie the basic principal of self-assembly because they resemble states of minimal energy.

Small length scale self-assembly is found in every living being. Each cell in the body contains a large amount of macromolecules which only exhibit their functionality after forming three dimensional supermolecular conformations directed by the principle of self-assembly.
Small amphiphilic molecules like phospho- or glycolipids make up the surrounding membrane of a cell allowing an exchange of metal ions or water and proteins through the cell wall.
The probably most important example of self-assembly in biological systems is the DNA, the origin of every functional molecule in the human body. Its sequence contains our genetic material, the genome, enabling transcription and translation processes finally leading to gene expression *via* the synthesis of proteins. Its double-helix structure develops by the self-assembly of two single DNA strands forming hydrogen bonds and making use of strong π-interactions between the nucleobases.
Other examples are the filament forming globular protein actin, the major component of the cytoskeleton or phospholipids, which assemble to form the lipid bilayers of cell membranes.
Humans have spend a great deal of time and effort to understand and copy nature's complex but intelligent behavior. Half a decade ago the concept of diblock copolymers as a useful substitute for nature's functional molecules was developed. These macromolecules provide a similar molecular geometry and easily form superstructures driven by the same principles.

Figure 1.2. Two examples for self-assembly on smaller length scales: The three dimensional structure of both Desoxyribonucleic acid (a) and a protein (b) is held together by hydrogen bonds and ionic interactions. Proteins for instance, consist of one or more long sequences of amino acids arranging in alpha helices and beta sheets making use of attractive interactions between carbonyl and amino groups as well as between different side chains.

The concept was explored in various fields, such as micelle and vesicle formation for drug delivery purposes in solution but also block copolymer mesophases were extensively studied. Section 2.2 deals with the theoretical background of block copolymer self-assembly and summarizes the commonly found examples.

Nowadays, water and air pollution have reached a dramatic level which requires the development of new filtration materials removing contaminants from water (rivers, oceans) and air especially near industrial areas or in large cities.

Among many, highly porous integral asymmetric membranes for filtration purposes are an example of how block copolymer self-assembly is used in today's material science. They are formed in thin films of highly concentrated solutions in a process involving solvent evaporation and fixation by a nonsolvent. Promising properties are provided by these materials, such as good mechanical stability and filtration performance, including high fluxes and improved size definition. This thesis gives an overview of how integral asymmetric membranes are formed and how they can be used to generate new functional materials in nanotechnology.

2 Literature Review

A central task in today's research is the development of mesostructured materials, which cover characteristic length scales between 1 and 100 nm. So far conventional lithographic and etching processes have produced structures of about 200 nm in size following "top-down" approaches. However, smaller dimensioned structures are needed for applications in modern technologies, e.g. magnetic storage devices or solar cells.
Numerous phenomenons found in nature are based on the concept of self-assembly. The formation of many highly functional superstructures is driven by energetic forces (see section 2.2) *via* the assembly of multifunctional macromolecules.[1]
In contrast to industrial methods to produce meso-structured materials, nature uses a spontaneous "bottom-up"-strategy which can serve as a model for material science.
A synthetic equivalent to natures multifunctional pool of molecules are block copolymers. Their geometry provides the opportunity to form extremely regular and stable superstructures in three dimensions on the nanometer length scale.
Spherical or cylindrical micelles are formed in dilute solution depending on the concentration (see left side of figure 2.1). Also, rather symmetric block copolymers assemble into disk-like particles which under certain circumstances form vesicles.[2,3] If biocompatible polymers are used, it is possible to use these structures for biomedical applications. Encapsulated hydrophobic drugs are transported in human blood vessels to be delivered at specific target positions.[4] More information can be found below (section 2.2.1).
Going from low to high concentrations and to the bulk state of block copolymer melts highly ordered three dimensional structures are observed which consist of similar structures brought in close proximity.[5,6] Among many, hexagonally packed cylinders, spheres arranged in a variety of different close packings and even bicontinuous interpenetrating networks are found which are also displayed in figure 2.1.

2.1 Block copolymers

Polymers are macromolecules consisting of a large number of covalently linked repeating units, the monomers. The simplest kind of polymer consists of only one monomer-type and is called homopolymer. Multiple monomer-sorts form copolymers, which are divided into four groups. The number and arrangement of different monomers determine which group a copoly-

mer belongs to. A schematic display of copolymers of different nature is shown in figure 2.2a-d.[7]

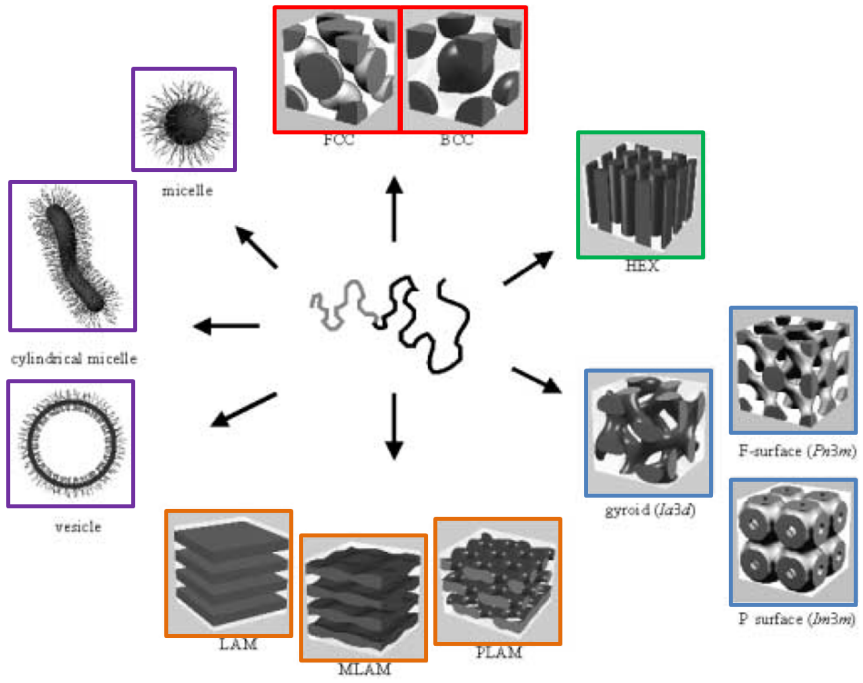

Figure 2.1. Different morphologies of block copolymers in solution (purple) and in the bulk. In diluted solution, amphiphilic bock copolymers assemble into spherical or cylindrical micelles as well as lamellae and vesicles respectively. Bulk structures include spheres arranged in either face- or body centered cubic lattices (FCC, BCC; red image frames) as well as ordinary, modulated or perforated lamellae (LAM, MLAM, PLAM; blue frames) and parallel cylindrical micelles aligned in a hexagonal lattice (HEX; green frame). Also, there are three types of structures needing minimal surface areas (gyroid, F surface, P surface; orange frames). According to[8]

Two or more randomly linked monomer-kinds make a statistical copolymer. A chain of two or more alternating monomer-sorts belongs to the group of alternating copolymers. Two or more linearly linked chemically different polymeric chains make a block copolymer and multiple chains diverging from one main chain are named branched copolymers.
Depending on the number of blocks they are divided into, block copolymers are classified as diblock, triblock or multiblock copolymers which are shown in figure 2.2e-h.

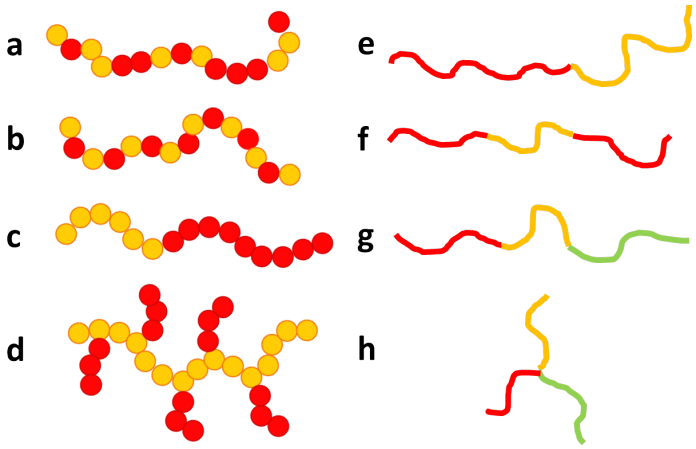

Figure 2.2. Schematic illustration of (a-d) different types of copolymers: (a) statistical, (b) alternating (c) block and (d) branched copolymer. Equally colored spheres represent the same monomer-type. (e-h) Monomer blocks arranged in multiple ways make different kinds of block copolymers. (e) simple AB-diblock copolymer, (f) ABA triblock copolymer, (g) ABC triblock terpolymer and (h) starblock copolymer. Differently colored lines represent different polymer blocks.[9]

Block copolymers composed of blocks with different polarity belong to the group of amphiphiles, because they show both hydrophilic and hydrophobic behavior at the same time. These macromolecules are particularly interesting because they combine the properties of different polymers like solubility, crystallinity or responsiveness to external stimuli like pH or temperature in one molecule.

In a solvent selective for one polymer block, insoluble chains show a very high surface energy which cannot be minimized by macroscopic phase separation because of the covalent linkage between the blocks. Thus, the system reacts by aggregating into domains of defined geometry like spherical or cylindrical micelles. The soluble blocks are located on the outside, while the insoluble blocks are hidden inside with a minimum interface to the solvent. Figure 2.3 gives a schematic illustration of micelle formation.

In order to get well separated polymer structures with narrow interfaces it is important to use polymers of uniform length, i.e. molecular weight. An ideal polymerization method is the living anionic polymerization (LAP) introduced by Swarc in 1956[10]. It is free of undesirable coupling or chain transfer reactions and also provides very low molecular weight distributions M_w/M_n even below 1.1.[11]

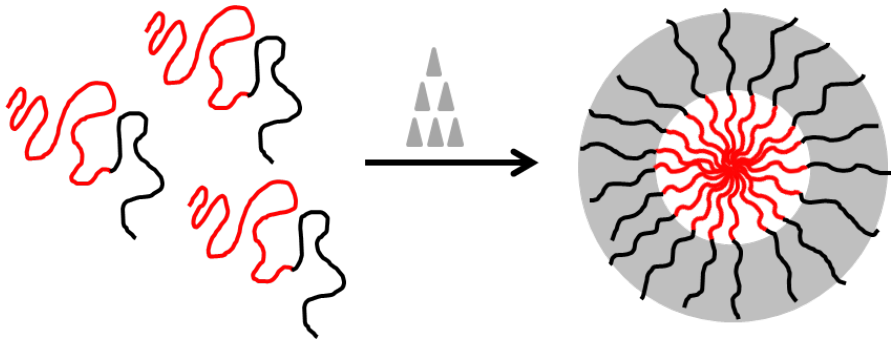

Figure 2.3. Schematic illustration of micelle formation. Upon contact with a solvent selective for the black polymer block (gray triangles) the red chains assemble in a spherical structure to minimize unfavorable solvent interactions.

Nowadays, amphiphilic block copolymers are used for a lot of different applications, such as foam stabilizers, structure directing agents during hybrid material synthesis (see section 2.4.1 and 2.5.3) as well as emulsifiers and dispersants.[12]

2.2 Self-assembly of amphiphilic diblock copolymers

Self-assembly is the spontaneous formation of well defined ordered superstructures from disordered objects of any size. It is frequently found in nature in large complexity on the microscopic or macroscopic length scale.

During the past decades many research groups focused on the self-assembly of amphiphilic block copolymers.[12,8] Similar to lipids or proteins, these macromolecules build highly symmetric and well ordered mesostructures which even show enhanced stability and durability and are therefore the perfect tool to fabricate nanostructured devices for a large variety of applications.

The self-assembly of any system is driven by energetic forces. Since in block copolymers two or more chemically different polymer blocks are connected *via* a covalent bond, short-range attractive interactions between the two blocks are provided. On longer scales, these chains repel each other, while similar blocks of separate molecules interact attractively.

This attraction can be of different kind, depending on the polymers. The simplest interaction would be hydrophobic, which is found for polymers without functional groups. Other possibilities are hydrogen bonding or electrostatic interactions. Depending on the type of interaction, polymers may crystallize or melt at a higher or lower temperatures.

The principle of self-assembly is illustrated in figure 2.4.

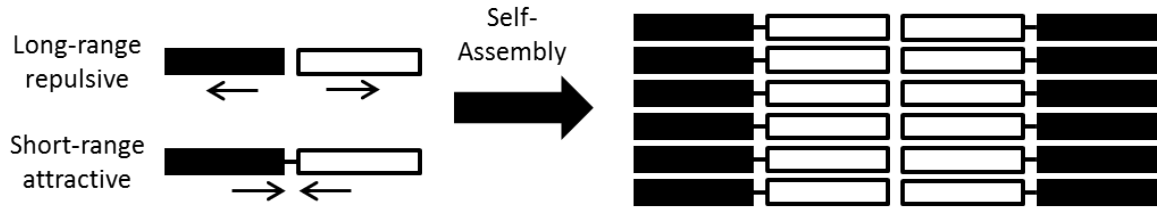

Figure 2.4. Schematic illustration of long-range repulsive and short-range attractive interactions affecting microphase separation of block copolymers.[8]

Energetically, homogeneous mixing of amphiphilic molecules usually shows an unfavorable (positive) enthalpy and only a small rise of entropy ($\Delta S \leq 0$), because polymer chains are conformationally restricted. The formation of ordered mesophases however is enthalpic much more convenient ($\Delta H < 0$), but entropically bad ($\Delta S < 0$), because the chains stretch and lose mobility. Depending on the kind of interaction between equal blocks, the enthalpy contribution often overweighs the negative entropy part leading to meso-structure formation.

2.2.1 Dilute block copolymer solutions

Since amphiphiles like block copolymers contain segments of opposite polarity, these substances show hydrophilic as well as hydrophobic behavior and can therefore be dissolved in both polar and nonpolar solvents. Dispersing in a segment-selective solvent leads to a high free energy for the incompatible block. The energetical driven response is a spontaneous assembly into domains of defined geometry, like spheres, cylinders or lamellae. Which geometry a system will aspire depends on multiple factors and is hard to predict. However, it is possible to narrow down feasible morphologies by using the packing parameter P which is introduced below.

The packing parameter P is a dimensionless value describing the geometry of an amphiphile in order to make assumptions about the morphology it is going to assemble into. For the calculation of P the length l_c and the volume V_c of the core forming block but also the surface area a_s demanded by the shell-forming block are taken into account. P is mathematically described in equation 2.1.

$$P = \frac{V_c}{l_c \cdot a_s} \tag{2.1}$$

In the simple case of a diblock copolymer the packing parameter depends on the relative block lengths. Symmetric block copolymers have relatively long core forming blocks together with a small surface area demand of the shell forming block. Therefore, the interface curvature is low and lamellae are formed ($\frac{1}{2} < P < 1$). This type of morphology is also found in vesicles as shown on the left side of figure 2.5. With increasing asymmetry of the blocks and larger surface area demands, smaller packing parameters are predicted. The developed interfaces are bent stronger, starting with cylinders ($\frac{1}{3} < P < \frac{1}{2}$) and moving into the regime of spheres with decreasing core size ($P < \frac{1}{3}$).[13,14]

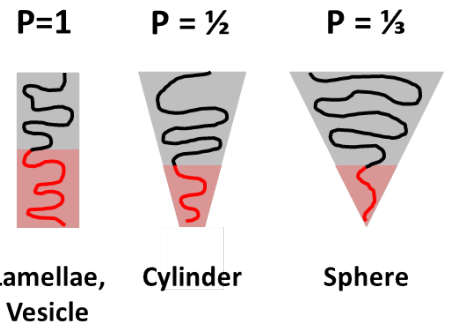

Figure 2.5. The influence of interfacial curvature on the formation of self-assembled morphologies.

2.2.2 Bulk morphologies

The same principles are applied in block copolymer melts. As described later in section 2.2.3 for homopolymer melts, the relative composition dictates the phase separation behavior of the block copolymer. Here, various morphologies shown in figure 2.6 are possible. Starting with closely packed spheres for very asymmetric block copolymers (S), with decreasing asymmetry hexagonally packed cylinders (C), bicontinuous networks (G) and lamellae (L) of the minor block in a matrix of the major block are formed. Inverse morphologies are developed when the volume fraction of the primary core forming block exceeds 0.5.

2.2.3 Polymer blends: The Flory-Huggins-Theory

The self-assembly of block copolymers can be modelled using the simplified model of a mixture of homopolymers. Enthalpic and entropic considerations have to be made in order to find

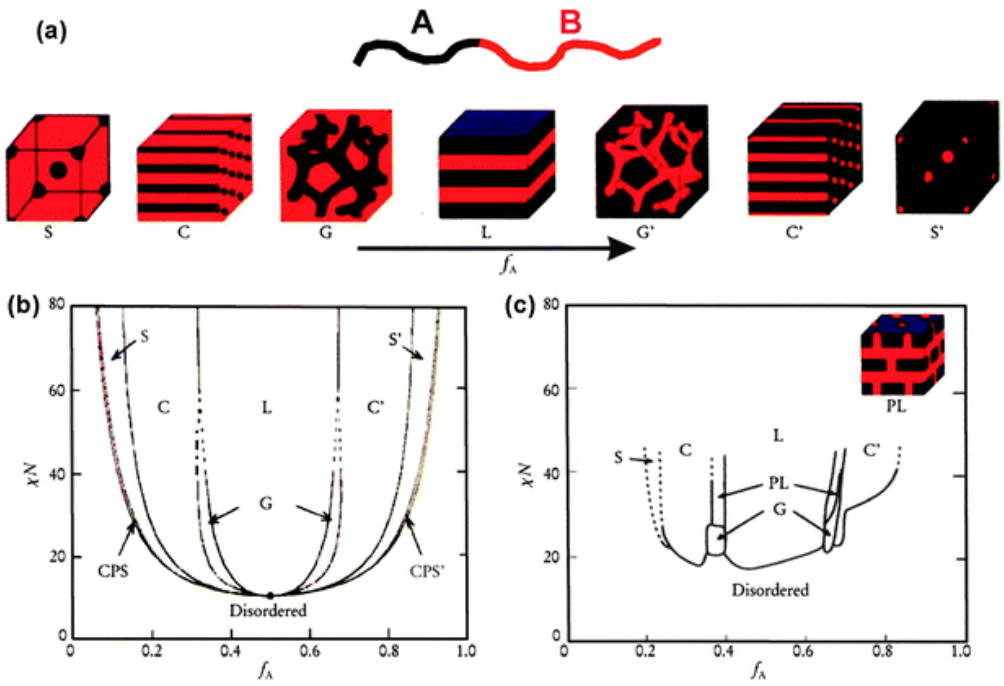

Figure 2.6. (a) Morphologies occurring in block copolymer melts varying with block copolymer composition. S=body-centered-cubic spheres; C=hexagonally packed cylinders; G= bicontinuous gyroid; L= Lamellae. The corresponding inverse morphologies are denoted S', C'.....[6] (b) Calculated phase diagram of a poly(styrene-isoprene) diblock copolymer melt by Matsen and Bates[15,16] using mean-field theory. CPS= closely packed spheres. (c) experimental phase diagram of PS-PI by Khandpur et al.[17] confirming the theoretical results. PL= perforated lamellae.

out if the components will mix spontaneously and in every composition.[18,19]

The physical quantity that combines both aspects, the molar free enthalpy of mixing ΔG_m, displays the energetic conditions of the system and is given by the Gibbs-Helmholtz-equation 2.2 where ΔH_m and ΔS_m are the molar enthalpy and entropy of mixing. Miscible components show a negative free enthalpy of mixing, while immiscibility is indicated by positive values.

$$\Delta G_m = \Delta H_m - T\Delta S_m \tag{2.2}$$

The change of entropy upon mixing of two components of any size depends on the number of possible arrangements in the available volume. For small molecules, the entropy is dominated only by the composition of the mixture assuming that each molecule is of comparable size, interchangeable and occupies only one lattice space. The entropy of mixing is given in the

following equation 2.3.

$$\Delta S_m = -R[\phi_1 ln\phi_1 + \phi_2 ln\phi_2] \tag{2.3}$$

Here, ϕ is the volume fraction of component 1 and 2 respectively, while R is the universal gas constant. Equation 2.3 shows, that blending of small molecules is always accompanied with a gain of entropy, i.e. disorder. Polymer blends on the other hand are conformationally restricted due to the covalent bonding of monomer segments. Thus, entropy plays a less important role in the mixing process. Mathematically the polymer volume fraction is reduced by the degree of polymerization P as shown in equation 2.4.

$$\Delta S_{m,Poly} = -R\left[\frac{\phi_1}{P_1} ln\phi_1 + \frac{\phi_2}{P_2} ln\phi_2\right] \tag{2.4}$$

The enthalpy of mixing of any two compounds (small or large) is given in equation 2.5.

$$\Delta(H_m) = RT\chi\phi_1\phi_2 \tag{2.5}$$

χ is the dimensionless Flory-Huggins interaction-parameter, describing the degree of compatibility between two components. Large and positive χ-values are found for strongly incompatible polymers. Attractively interacting polymers exhibit a negative χ-parameter, while values between 0 and 1 are found for slightly incompatible components. χ is temperature-dependent *via* the following expression.[5,6,13]

$$\chi_{AB} = \left(\frac{z}{k_B T}\right)\left[\epsilon_{12} - \frac{1}{2}\left(\epsilon_{11} + \epsilon_{22}\right)\right] \tag{2.6}$$

z is the number of nearest neighbors per monomer, k_B is Boltzmann's constant and ϵ is the interaction energy per monomer of each component.

Equation 2.4 and 2.5 can be summarized to an expression for the molar free enthalpy of mixing ΔG_m.

$$\Delta G_m = RT\left[\frac{\phi_1}{P_1} ln\phi_1 + \frac{\phi_2}{P_2} ln\phi_2 + \chi\phi_1\phi_2\right] \tag{2.7}$$

For large polymers ($P >> 1$), the entropic contribution to ΔG_m becomes insignificant and only the enthalpic considerations have to be made in order to determine, whether two polymers will

form a homogeneous blend. Eq. 2.7 is then reduced to the following expression.

$$\Delta G_m = RT\chi\phi_1\phi_2 \tag{2.8}$$

Figure 2.7 illustrates the developments of ΔS_m, ΔH_m and ΔG_m with the blend composition. Since temperature and χ are inversely linked, rising temperature eventually leads to enhanced polymer compatibility, i.e. immiscible polymers can become partly soluble when the temperature is increased. In this example the polymers are most likely to demix, because a

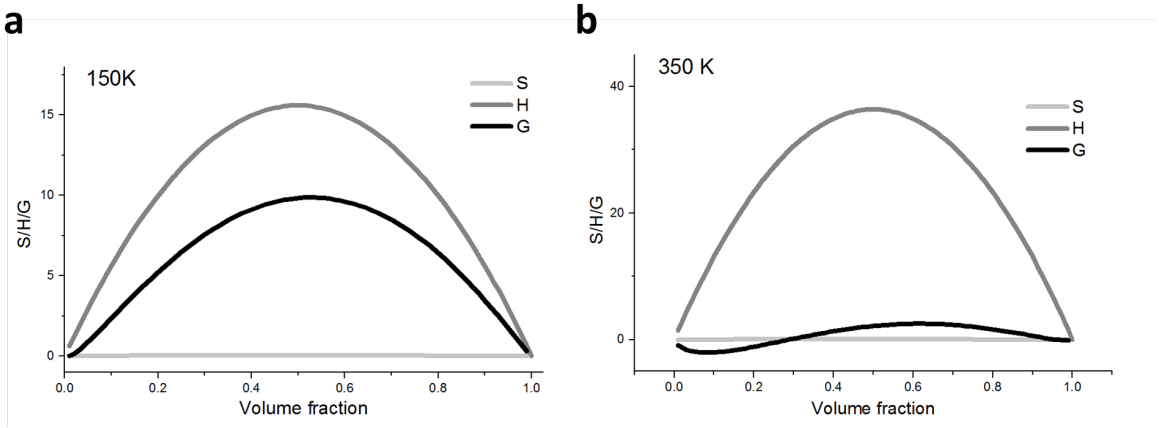

Figure 2.7. Progress of ΔG_m with varying blend composition at (a) 150K and (b) 350K. Parameters P_1 and P_2 are 100 and 300 respectively and the χ-parameter was chosen to be 0.05. For ϕ-values larger than 0.37 the components are immiscible and separate in two phases.

χ-parameter of 0.05 suggests medium compatibility. At 150 K, figure 2.7a shows complete immiscibility, meaning that for every composition the free enthalpy of the blend is higher than the sum of the pure components. However, at 350 K the polymers become partly soluble. Until a composition ϕ_1 of approximately 0.13, the polymers show a negative free enthalpy of mixing and form a homogeneous blend. Between 0.13 and 0.37, the blend is metastable until the free enthalpy reaches a turning point, after which it steadily rises and crosses over into the unstable, demixed region where the free enthalpy is positive. Many diagrams like this for different temperatures can be used to draw a phase diagram for the polymer blend by identifying the minima, maxima, and turning points and mapping them in a T-ϕ-diagram. An example phase diagram is shown in figure 2.8.

The Binodal is composed of the extremal values of a series of ΔG-diagrams marking the composition, where a stable polymer blend crosses over into the metastable region. Here,

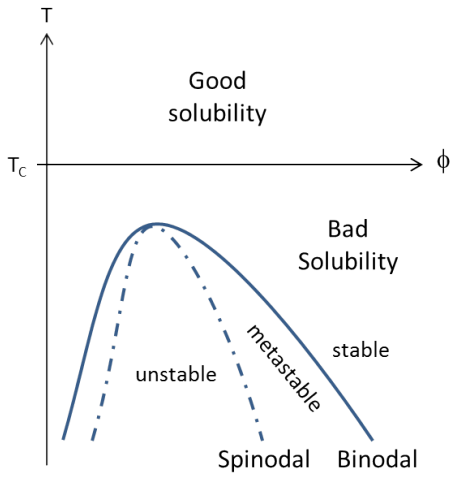

Figure 2.8. Phase diagram of a binary mixture of homopolymers exhibiting a miscibility gap marked by the binodal and spinodal line. Between binodal and spinodal the mixture is metastable.

decomposition occurs upon nucleation. The transition from the metastable to the unstable region is marked by the spinodal.

The theoretical considerations explained above can also be applied to self-assembling block copolymers. The formation of mesostructures resembles the process of demixing of a homopolymer blend in the region of a phase diagram where ΔG is above 0. Since the two compounds are chemically linked *via* a covalent bond, block copolymers cannot decompose in two separate phases (like water and oil). Instead, they are forced to minimize the segment interactions by forming block-rich domains with narrow interfaces on the mesoscopic length scale given by the degree of polymerization of the polymer segments.
Further, the shape of block copolymer bulk morphologies depends not only on the relative segment volume fractions f_v but also on the total degree of polymerization N and the Flory-Huggins interaction-parameter χ which is expressed in equation 2.6. Mesostructure formation occurs, if the interaction energy of different monomers strongly exceeds the average interaction energy of equal monomers, which is when χ becomes positive.
To categorize these systems, the so-called weak segregation limit (WSL) and the strong segregation limit (SSL) where introduced by Leibler[20] and Semenov[21].
Very incompatible polymer blocks ($\chi N >> 10$) are considered in the strong segregation

regime. Their corresponding melts show well defined three dimensional structures with length scales increasing with the polymer chain length. Among others, the most common examples are closely packed spheres, cylinders or lamellae (for comparison see figure 2.6).
Systems showing χ-values between 0 and 1 belong to the weak segregation regime ($\chi N << 1$) and are expected to show only slightly ordered melt structures with sinusoidal composition profiles, meaning no or only rough segregation and very broad, blurred interfaces. Since χ is inversely linked to the temperature, heating will eventually induce compatibility, meaning a transition from ordered, self-assembled structures into a disordered state (homogeneous solutions). The bottom of figures 2.6b and c corresponds this condition when the entropy contribution to the mixing process overweighs the enthalpy contribution.
A theoretical phase diagram was calculated using the block copolymer composition and χN as variables[16], the latter determining the degree of incompatibility.

2.3 Integral Asymmetric Block Copolymer-Membranes

In a thin film, the principle of block copolymer self-assembly can be used to fabricate highly porous membrane surfaces with closely packed nanochannels on top of a spongelike macroporous supporting layer. These membranes have very high pore densities and narrow pore size distributions and are used for water filtration and protein or gas separation. In 2007 this approach to a new kind of filtration material has first been introduced by Peinemann and Abetz[22] for the PS-P4VP block copolymer system and it has been the center of attention of several research groups for the following years until today.[23–25]
Due to their asymmetric geometry these materials show enhanced properties concerning separation efficiency and accuracy compared to other filtration devices. The separating layer of approximately 100-200 nm thickness consists of closely packed cylindrical to spherical pores with sizes in the nanometer range but upon looking further into the film's interior an increase in the structure dimensions becomes clear and can be observed particularly well in cross sectional SEM images like the one shown in figure 2.9.

2.3.1 Reference System PS-*b*-P4VP

The mesoporous structure of, e.g., PS-P4VP is formed by self-assembly in highly concentrated solutions in a non-selective solvent mixture consisting of DMF and THF. When the solution is

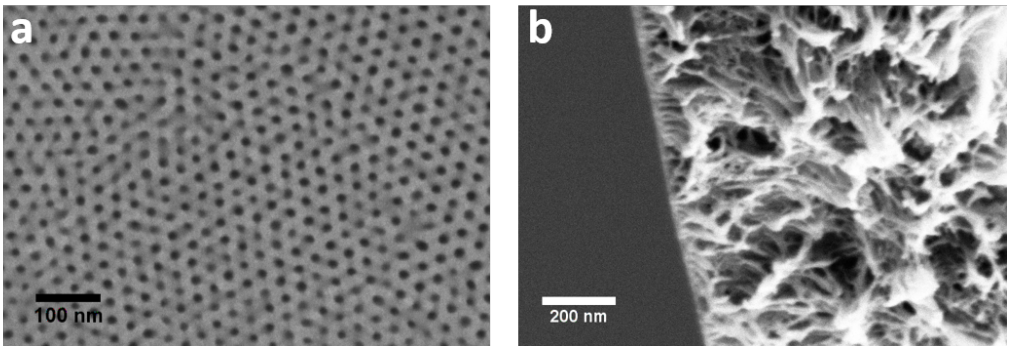

Figure 2.9. SEM image of (a) the surface and (b) of the cross section of an integral asymmetric membrane prepared from PS-*b*-P2VP diblock copolymer. The cross sectional image (b) was obtained by freeze-fracture.

cast into a film, solvent evaporation immediately begins and phase separation is induced.
The volatile solvent component THF is a particular good solvent for PS, PVP on the other hand is well soluble in DMF. The combination of both solvents provides highly swollen polymer blocks in solution. The initial mixture is therefore considered neutral. Figure 2.10 gives a schematic explanation of the solution's state prior to and after casting.
When THF evaporates from the solution, a concentration gradient develops vertically across the film and microphase separation is induced. Figure 2.11 points out the evaluations of the gradient in different layers. The bottom of the cast film (C) dries very slowly because of the large distance to the film surface. Therefore, the polymer concentration is constant and close to the casting concentration c_0 for a long period of time until finally the solvent evaporates. The top layer (A) on the other hand drys very fast and steady while the solvent in layers of medium depths evaporate more slowly but also steadily.
During film formation, the solvent mixture becomes selective for PVP ($\chi \geq 0$) and PS begins to demix from the solution and vitrifies. Simultaneously, it assembles into domains, here a continuous matrix with hexagonally ordered cylindrical channels as the primary structure, leaving the P4VP as the channel-surface polymer. Meanwhile the PVP block swells with DMF due to the change of solvent quality becoming more suitable for PVP.
During evaporation of THF the block copolymers χ-parameter continuously rises, starting from a homogeneous mixture, passing the regime of weak segregation and crossing over into the strong segregation regime for nearly dried films.
In order to prepare a membrane usable for filtration purposes, the porous matrix formed shortly

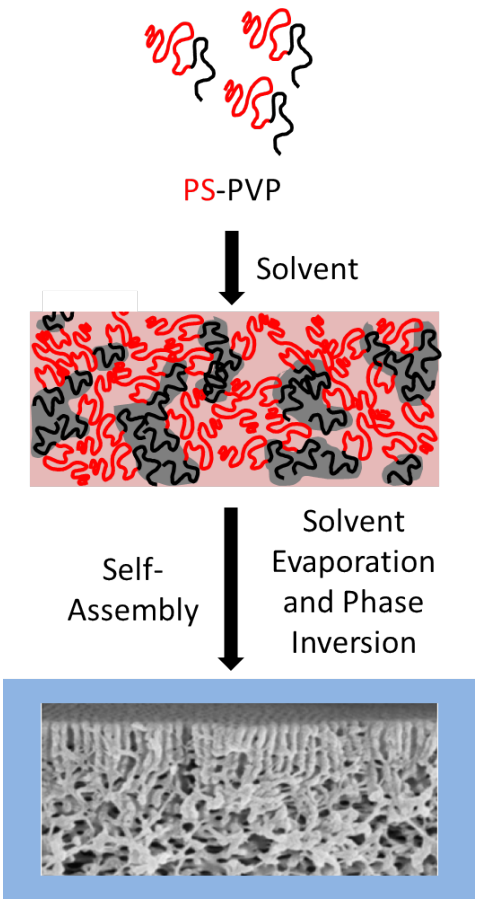

Figure 2.10. Schematic survey about the membrane system studied in this thesis. It is formed from a block copolymer (poly(styrene-*block*-vinylpyridine) (top) which is dissolved in a high concentration in a solvent mixture with two components, each selective for one polymer block (middle). After film casting and solvent evaporation a porous membrane surface structure develops and is fixed in a non-solvent bath (bottom).[22]

after casting has to be preserved. This is achieved by immobilizing the polymer chains at a specific moment during solvent evaporation using an excess of a non-solvent like water. It quickly diffuses into the still liquid PVP domains swollen with DMF and precipitates the polymer which collapses onto the PS matrix leaving behind hollow pores.

Broadening the time frame for the immersion step would significantly ease the preparation process, especially with regard to larger scale industrial membrane production. A way to realize this is to use the basic character of, for example, vinylpyridines nitrogen atoms for complexes with metal salts. The coordinative bonds restrict the chain dynamics and increase the temporal stability of the continuous matrix.[26–28]

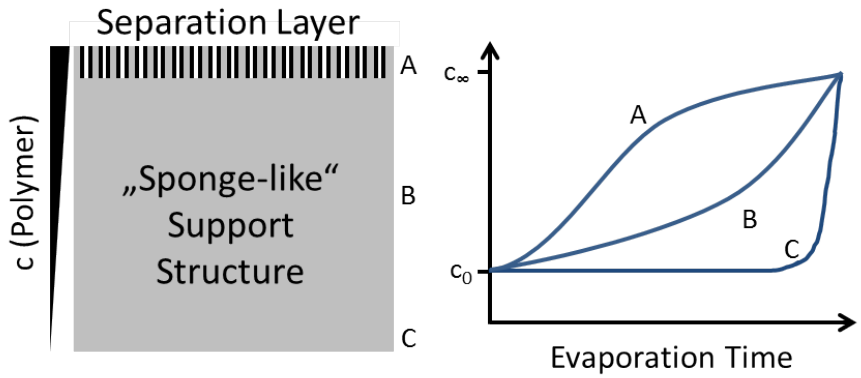

Figure 2.11. Schematic display of the developing concentration gradient during evaporation of solvent from the porous separation layer to the macroporous "sponge-like" support structure. The depths A-C represent layers of different temporal evolution of polymer concentration from the casting concentration c_0 to the final dry concentration c_∞.

2.3.2 External stimuli

Depending on the type of membrane polymer, certain properties can be triggered by external stimuli. For example the polymers poly-2- and -4-vinylpyridine reversibly respond to pH changes because of the alkaline nitrogen atoms in the aromatic side chains which are protonated in low pH solutions. Protonation leads to completely unfolded PVP chains lining the pore edges which results in pore diameters changing linearly with pH as shown in figure 2.12.[29]

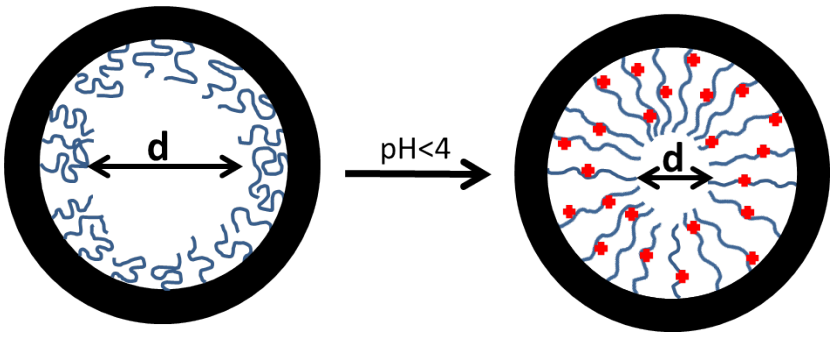

Figure 2.12. Schematic illustration of a shrinking pore radius upon pH decrease. The positive charges of the nitrogen atoms repel each other, leading to complete chain unfolding.

Temperature is another trigger to be used for polymers like poly(*N*-isopropylacrylamide, PNiPAM) also resulting in a change of pore diameter. Poly(*N,N*-dimethylaminoethyl methacrylate, (PDMAEMA) even responds to both stimuli.[23]

2.3.3 Post-Functionalization

The introduction of functional groups to membrane surfaces is useful to optimize membrane performance. Membrane fouling is a phenomenon ocurring during filtration causing membrane fluxes slowly to decrease with time. Figure 2.13 schematically illustrates the principal of fouling. Due to attractive interactions, such as hydrophobic, ionic or van der Waals interactions as well as hydrogen bonds large molecules adsorb to the membrane surface or within the material and block the channels.[30]

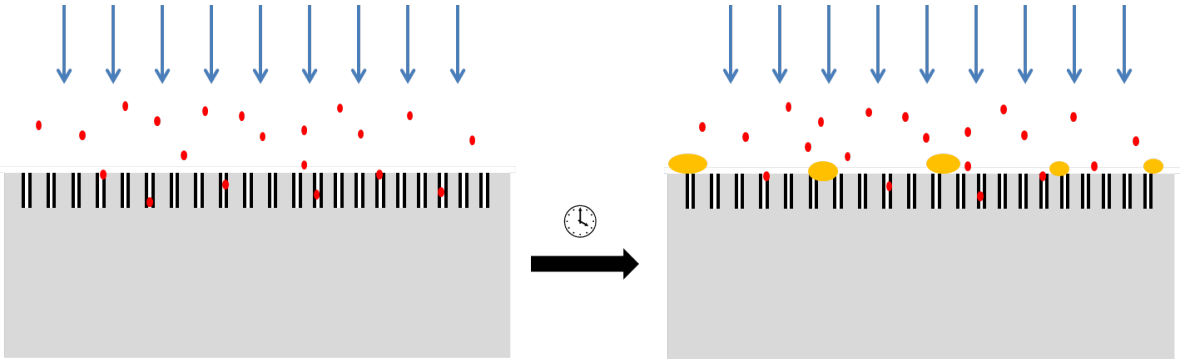

Figure 2.13. Schematic illustration of membrane fouling during filtration. The red dots represent proteins or other biomolecules small enough to pass through the narrow pores. The yellow objects originate from the liquid to be purified. Microorganisms, large proteins or inorganic substances like phosphates, hydroxides or silicates adsorb to the membrane surface closing the pores.

A large variety of modifications can be applied in order to prevent or postpone membrane fouling, some examples given in ref[31–33].

The introduction of functional groups into the pore lining polymer block provides many possibilities of modifications after membrane preparation which render new properties. This becomes important during the filtration of biomolecules having other functionalities complementary to the post-modification of the membrane. These molecules are held back during filtration and can later be washed out again. This represents an effective method for selective protein separation.

Polymers like PEO offer the opportunity of functionalization due to their hydroxyl end group directly after synthesis. Also it is possible to quaternize nitrogen atoms in P2VP or P4VP or to convert esters, like in PMMA. Functionalities can also be induced *via* coordinative bonds or supramolecular interactions.

2.4 *In Situ* Methods

With regard to exact, cost- and work-efficient membrane production procedures especially concerning future large-scale industrial applications, it is neccessary to learn about the kinetics of film formation.
Synchrotron small-angle X-ray scattering can serve as a useful tool to monitor structural evolutions during the development of a thin film. Nowadays high energy X-ray sources with high brilliance and beam diameters in the μm-range are available at synchrotron beamlines. These preconditions provide the possibility to study a large variety of systems. So far, low scattering contrast and fast evaporation kinetics have been limiting the pool of observable systems. However, state-of-the-art detectors are highly sensitive and provide read-out times down to milliseconds and thus are suitable for many kinds of weak or strong scattering samples even if the investigated process is completed in seconds. The following section summarizes some experiments published during the last decade making use of today's equipment for scattering methods to clarify morphological transitions in colloidal or polymeric systems.

2.4.1 Investigation of silica film formation

Porous silica films in various 3D lattices gained rising importance during the last years because of their optical and separation properties as well as their potential use as catalytic materials owed to their exceptionally high surface area.
The formation of these highly ordered structures is usually directed by organic surfactants assembling into micellar morphologies and templating the polycondensation of organosilicate precursors. In 2002 Grosso et al. used *in situ* synchrotron SAXS measurements to probe silica-film formation of dip-coated tetraethyl orthosilicate (TEOS) templated by cetyltrimethylammonium bromide (CTAB) in a water/ethanol mixture during the evaporation of solvent.[34,35]
A dip-coater was designed to fit in a synchrotron beam in order to probe the structural evaluation in the freshly cast film (see figure 2.14). The measurement was started right after pulling the dip-coater out of the solution and continued during solvent evaporation until a porous silicate phase had developed. The molecular geometry of the directing agent (here CTAB) determined the shape of the silicate structure.
The influences of many parameters, such as sol composition and aging time, withdrawal rate corresponding to film thickness and the surrounding humidity were determined.[36] On the ba-

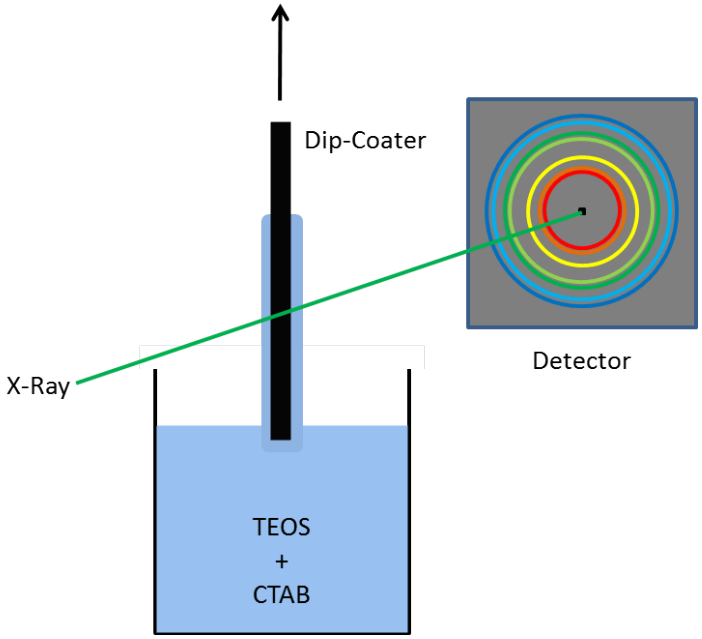

Figure 2.14. Drawing of a dip-coater placed in a synchrotron beam.

sis of their findings the presence of a modulable steady state was proposed providing the possibility to change the outcoming lattice or functionality of the resulting mesoporous structure.

Block copolymers were also used as directing agent for silica film formation by the same group in 2001 [37]. They used a symmetric triblock copolymer (PEO_{106}-PPO_{70}-PEO_{106}) to direct the formation of hexagonally arranged cylindrical mesopores from TEOS precursors. Film formation was investigated analogously during the first 5 minutes after dip-coating using *in situ* SAXS with a temporal resolution of one image per second.
Also, highly crystalline cubic mesoporous TiO_2 phases were prepared using PHB-PEO block copolymers as structure directing agents by Smarsly et al. The formation mechanism during solvent evaporation and subsequent heating was studied *in situ* using GISAXS on dip-coated samples. [39]

An alternative route to highly porous silica-materials is to simply blend silica precursors with a degradable porogen component and perform silica polycondensation around it. Subsequent decomposition of the latter by e.g. heating or UV exposure leaves behind a highly porous

silica-material. Because of their low dielectric constant, these materials are especially interesting for applications as interdielectrics.
Following this approach, in 2005 Lee et al. used homogeneous blends of poly(methylsilsesquioxane)-precursors and a large four-armed poly(ϵ-caprolactone) (PCL) to prepare nanoporous films and monitored the pore evolution during heating with constant power using *in situ* grazing incidence small-angle X-ray scattering.[40]. The principal set up is depicted in figure 2.15. In the beginning of the experiment, the silica precursor (light gray) was polymerized around the organic porogen particles (red dots) which were subsequently removed by thermal decomposition leaving behind hollow pores (white dots). During the whole process the sample was exposed to the X-ray beam to monitor the pore development. They were able to identify

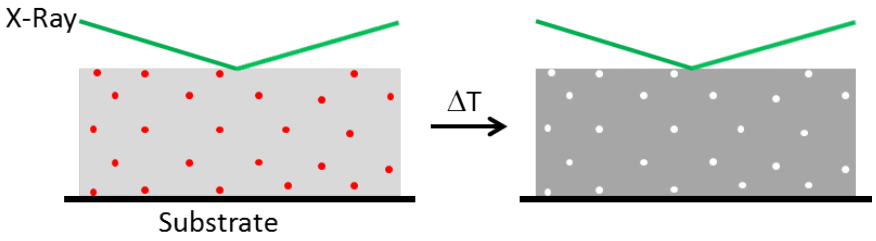

Figure 2.15. Illustration of the formation of a porous silicate structure. Here, the pore formation is guided by a degradable organic polymer dispersed in the silicate precursor solution.

exact temperatures of matrix development due to polycondensation and final decomposition of the PCL-porogen, leading to nanopores. Size distributions have shown to depend on the content of porogen in the initial blend, whereas high loadings resulted in broader pore size distributions.

2.4.2 Investigation of Latex Film Formation

Water soluble polymer-latex particles are an extensively investigated system of colloids, which form soft crystals arranged in various three dimensional lattices upon drying. Hu et al. used a styrene/*n*-butyl acrylate copolymer system to study the formation kinetics of fcc lattices during evaporation of water in a single droplet.[41]
Therefore a glass capillary was placed in a synchrotron beam, filled with latex-solution until a droplet protruded from the opening, meeting the X-ray beam. Figure 2.16 gives a schematic

overview of the experimental setup. In the first stages of the measurement the droplet merely contained single latex particles resulting in a scattering pattern of atomic formfactor oscillations. After some time the particles moved closer due to the evaporation of water and the first signs of ordering became evident. When evaporation continued, the scattering pattern of a closely packed particle lattice developed with rising degree of ordering.

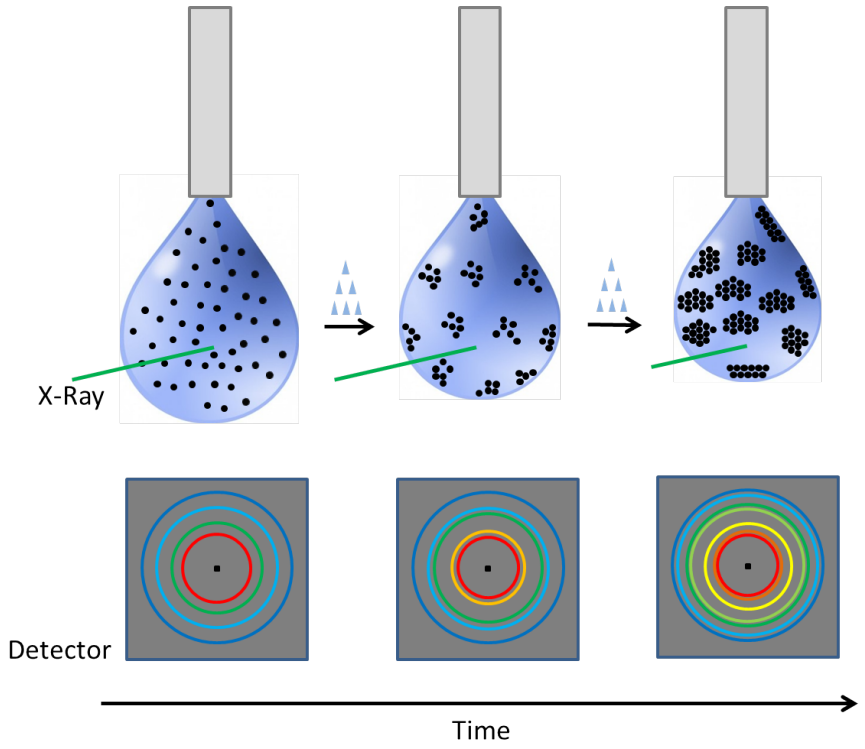

Figure 2.16. Schematic display of the experimental buildup of the measurement performed by Hu et al.[41] During progressing evaporation the droplet contracts and the particles approach each other (top), thereby slowly developing a scattering pattern (bottom) giving information about lattice type, particle distance, radius and domain size.

Three characteristic stages during water evaporation were defined and a mechanism of structure formation was proposed including water evaporation, particle ordering and particle deformation).

The same Latex-system was used in 2010 to investigate the interdiffusive behavior of polymer chains of adjacent latex-particles *in situ*.[42] Here, the investigation was both time- and temperature dependent. It was found that upon increase of temperature the polymer chains inside a

latex-particle become mobile and start to penetrate the stabilizing surfactant membrane leading to the fusion of adjacent particles. This became evident from the *in situ* experiments when the distinct scattering pattern of a highly ordered fcc lattice transformed into diffuse scattering of an amorphous structure.

A similar system of soft colloidal crystals was used to study the reaction of materials to external stress. Styrene/butadiene copolymer latex particles for instance represent a useful system to study the effect of tensile strength on particle ordering and deformation by *in situ* X-ray scattering.[43] Men et al. found that soft colloidal latex crystals deform upon medium tensile strength when a linear dependency of the lattice dimensions on the film extension was observed. Here, the particle interactions were described as “affine“. Upon applying stronger forces, the system responded with slippage of particle layers and grains in order to provide the stretched, elongated sample form. This behavior is usually expected for mechanically hard colloidal crystals and is described as nonaffine interaction.

2.4.3 *In situ* Investigation of Solvent Vapor and Temperature Annealing of Block copolymer thin Films

Nanostructured materials originating from block copolymer thin films have drawn significant attention for the fabrication of, e.g. templates or filtration materials. High ordering is often achieved only through annealing procedures *via* high temperatures or exposure to organic solvents.

In situ GISAXS is a feasible tool to monitor the annealing process. It facilitates the determination of multiple phenomenons, such as domain-swelling, rearrangements as well as transitions between morphologies or into the disordered state.

Solvent vapor annealing at room temperature of the poly(styrene-*block*-butadiene) system was intensively studied by Papadakis[44] and Di et al.[45,46] who used toluene and cyclohexane respectively as annealing solvents.

The structural changes of the poly(α-methylstyrene-*block*-4-hydroxystyrene) system upon solvent vapor annealing in two different solvents was investigated by Paik et al.[47] Also, Russell and coworkers have recently used *in situ* GISAXS to study the structural evolution of poly(styrene-*block*-2-vinylpyridine) block copolymers in thin films during vapor annealing with Tetrahydrofurane.[48]

Thin films of asymmetric $A_3B_3C_3$ star polymers assemble into complex hexagonal (HEX) morphologies after annealing in chloroform. In detail the structure consists of truncated cylinders and triangular prisms surrounded by a matrix oriented parallel to the film surface. Recent *in situ* grazing incidence X-ray scattering experiments by Rho et al. on a (polystyrene)$_3$-(poly(4-methoxystyrene))$_3$-(polyisoprene)$_3$ (PS_3-$PMOS_3$-PI_3) system revealed a partial 30°-rotation of the described hexagonal structure upon heating to a specific transition temperature. Both types of 3D hexagonal structure have proven to be very stable even well above the glass transition temperatures of the single polymer blocks. Surprisingly, the partly rotated structure remained after cooling the sample.[49]

2.4.4 Investigation of Nanoparticle Deposition and Ordering

It is possible to observe ordering of nanoparticles using X-ray scattering methods. Recently, Al-Hussein et al. used GISAXS to probe the structural evolution of gold nanoparticles with a temporal resolution of 20 ms.[50] The experimental setup consisted of an airbrush positioned directly above the X-ray beam spraying an aqueous nanoparticle solution on a polymer film consisting of poly-3-hexylthiophene (P3HT). In combination with *ex-situ* AFM measurements they found islands of gold monolayers after drying.
The ordering of polystyrene nanoparticles was observed *in situ* by Herzog et al. in 2013[51]. Here, also spray deposition was used to monitor the dewetting of a silicon substrate *in situ* with an experimental setup very similar to the one described above. Due to the evaporation of a water/ethanol solvent mixture, the solution progressively dewetted the substrate until small droplets were formed. The first aggregates of ordered nanoparticles showed when the solution had already broken up on the silicon surface, which became evident from an appearing side maximum in the scattering patterns. The aggregates were located on the surface of a single droplet due to a developing concentration gradient.

Nanoparticle aggregation monitored in the gas phase is a promising method of analysis because it involves low scattering background. The first group to report *in situ* SAXS studies on nanoparticle ordering in the gas phase were Sen et al. in 2007[52]. They designed a complex apparatus producing a mist of small droplets from a sample solution *via* ultrasound which was transported through a temperature-controllable tube *via* nitrogen gas flow. Several sensors

were added in order to maintain an adequate temperature gradient, mass flow and pressure inside the tube. X-ray transparent windows were integrated in six different places to provide measuring sites for the scattering experiments. It was found, that the drying speed strongly influences the arrangement of particles inside a droplet. Fast drying lead to a type of core-shell particle, where the major part of the particle density was located in the shell. Slow drying on the other hand produced homogeneous particles with a constant density distribution.
Using a similar apparatus, Shyjumon et al. studied silica film-formation using CTAB and TEOS *in situ* as described above upon heating and in the gas phase.[53] Interesting future experiments would include the formation of metal nanoparticles from their corresponding precursor materials.

2.4.5 Formation of ordered Mesoporous Carbons by Thermally Induced Self-Assembly

In situ SAXS has proven to be a useful tool for monitoring the formation of ordered mesoporous carbons (OMCs). Schuster et al. used PEO-PPO-PEO triblock copolymers to direct an ordered structure formation in thin films and in the pores of anodic alumina membranes. The structure developed when the polymerization of a Resol precursor was induced upon heating.[54] During all stages of carbon formation the structural evolution was investigated including solvent evaporation, heating to above $100\,^{\circ}\mathrm{C}$ where the ordered structure is formed and further heating to remove the template and carbonization above $1000\,^{\circ}\mathrm{C}$. During the last stage a shrinkage of the network dimensions was observed.

2.5 Hybrid Materials

Due to their diminutive size and large surface area, nanoparticles have interesting properties which their corresponding bulk materials do not have (size quantization effect[55,56]), such as improved optical, electrical, magnetic or catalytic qualities. A large diversity of nanoparticles (Au, Pt, Pd, Rh, Cu, $\mathrm{FeO_x}$ and ZnO among many others) is nowadays used in various fields of applications, e.g. catalysis, electronic devices, biomedicine (drug delivery), magnetic resonance imaging, waste water treatment and cosmetics.
Combining nanoparticle characteristics with those of a polymeric material provides an inter-

esting way to new multifunctional materials, the so called polymer-inorganic nanocomposites (PINC,[57]). For this purpose the nanoparticles need to be well dispersed in the polymer matrix, which implicates the problem of agglomeration. This issue is overcome by generating strong repulsive forces between the nanoparticles, keeping them at distance from each other. Modifying nanoparticle surfaces with certain organic molecules, e.g. short polymers, offers versatile solutions to prevent agglomeration and generate stable nanoparticles dispersible in a polymeric matrix.

2.5.1 Nanocomposites

The first nanocomposite reported was made of gold nanoparticles in a polymer matrix in the year 1833 by Lüdersdorff.[58] The following section deals with the challenges of polymer-nanocomposite synthesis followed by different approaches to distribute composite particles within hybrid materials.[57]

Nanoparticle Synthesis

Nanoparticles are generally synthesized *via* physical or chemical methods. The former involves techniques following “top-down“-approaches, such as milling or lithography. Here, a large bulk material is repeatedly divided into smaller pieces, which finally reach nanometer size. Physical methods yield relatively broad size distributed particles and are not consistent in the particle shape. Moreover they do not reach the diameters needed for nanotechnological applications.
Most chemical approaches are based on “bottom-up“-strategies involving precursor particles, such as metal ions, which are chemically reduced to the atomic state by an electron donor. Controlled agglomeration renders the actual nanoparticles, whereas stabilizers adsorb to the surface and prevent large-scale coagulation. Chemical synthesis methods have been chosen over physical methods, because they have proven to be more effective concerning particle diameter, shape and properties.[59]

Coating of nanoparticles

One possibility of nanoparticle surface modification is the formation of covalent bonds. TiO_2 or SiO_2 for example offer hydroxyl-groups on the surface which can react with hydrophobic

agents (e.g. silicon derivatives[60,61], alkoxides or epoxides) to modify nanoparticle solubility in organic solvents or polymeric matrices. Figure 2.17 gives a schematic example where a pre-hydrolized silica species is used to coat a surface bearing OH-groups. The nature of the group *R* not only enables to alter the solubility but also provides a facile way to introduce functionality.[62]

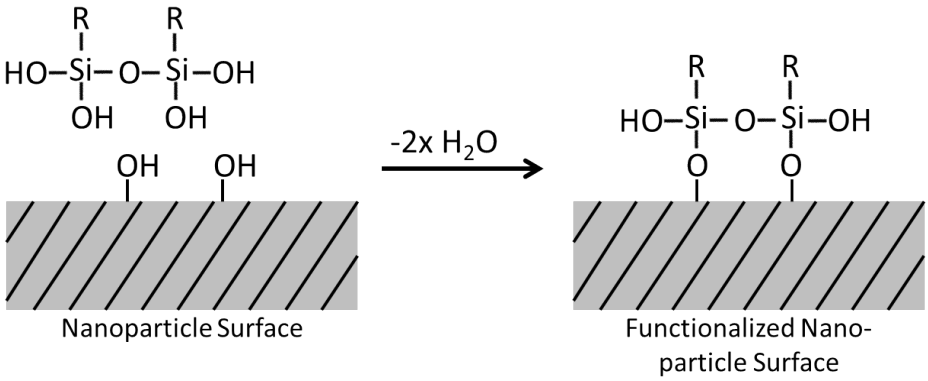

Figure 2.17. Schematic illustration of a surface modification using silane coupling agents. A pre-hydrolized organosilicate is used to be reacted with the hydroxyl groups localized on the surface of, e.g. SiO_2 or TiO_2 nanoparticles. The choice of the substituent *R* regulates not only particle solubility but can also introduce functionality.

Coordinative bonds are also used to modify nanoparticle surfaces, generating PINCs. Pre-synthesized polymers with functional groups containing Lewis bases at one end can be grafted to nanoparticle surfaces, leading to the formation of a dense brush layer. Another option is to grow polymer chains from the nanoparticle surface precoated with a monolayer containing an initiator group (grafting from).[63] Both principles are explained in figures 2.18 and 2.19.

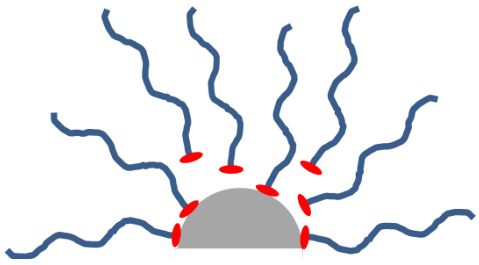

Figure 2.18. Schematic illustration of the grafting-to coating method. The polymer chains have been previously modified with an anchor group, such as amines or carboxylate groups and are attached to the nanoparticle surface *via* coordinative binding.

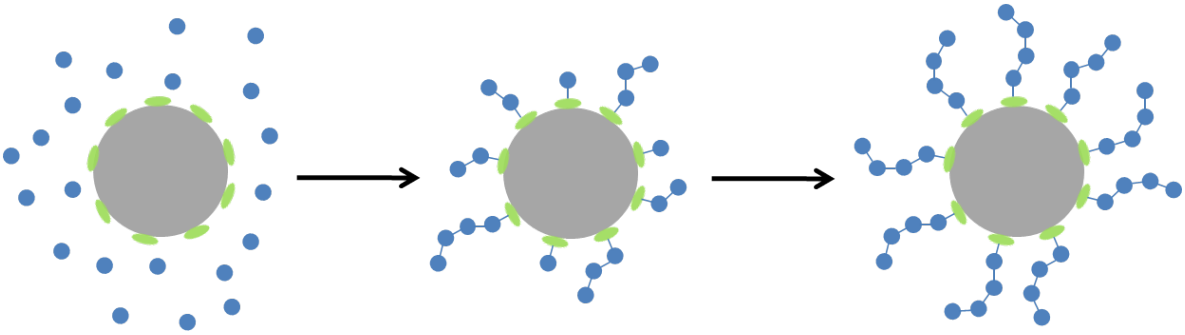

Figure 2.19. Another grafting method (grafting-from) where the polymer chain grows on to the nanoparticle surface functionalized with group initiating the polymerization (green oval).

Due to very fast agglomeration, some nanoparticles must be synthesized in the presence of stabilizers (e.g. oleic acid, hexadecylamine or trioctylphosphine).[64,65] If necessary for the application, these synthesis-ligands can be replaced by other ligands (e.g. pyridine), simply by refluxing in the pure ligand. To achieve maximum ligand substitution, washing steps prior to ligand exchange can be useful in order to generate a maximal efficient nanomaterial.[66]

2.5.2 Hybrid material synthesis

The most frequently used approaches to disperse nanoparticles in a polymeric matrix are explained here. The addition of nanoparticles very often improves the properties of the matrix material. For many examples, PINCs show better mechanical strength, hardness or elasticity than their corresponding unfilled matrix material. Also thermic or electric properties have shown to enhance upon nanoparticle addition. Moreover, properties given by the nanoparticles can also be improved, such as optical or conductive characteristics.

Sol-gel processing

A way to obtain continuous interpenetrating networks of inorganic and organic compounds under mild conditions is sol-gel processing. Here, the polycondensation of a pre-hydrolyzed precursor (e.g. tetraethyl orthosilicate or tetrabutyl titanate) is performed in a polymer solution. Extensive information is given in ref.[67].
Another method making use of the sol-gel principle was described by Hsiue et al. and uses a pre-formed silicate sol-gel network carrying polymerizable functionalities for radical or cationic

polymerization. When initiator was added, the polymer network formed around the existing inorganic network, resulting in the same structure as described above.[68–70] Also Hajji et al. performed a similar experiment when they simultaneously polymerized TEOS and hydroxyethyl methacrylate (HEMA).[71]

In situ growth of nanoparticles or polymer matrix

In situ methods for hybrid material fabrication were introduced by Ou et al., who polymerized nylon-6 around silica nanoparticles in a bulk-type ring-opening polymerization.[72]
Vice versa also nanoparticles can be grown from a previously polymerized matrix modified to contain nanoparticle precursor functionalities. These act as nucleation sites for the nanoparticles after transformation into the atomic state. Among other possibilities reductions can be performed chemically, thermally *via* decomposition or using photons as initiator.[73]
As a third approach, polymerizing a matrix material at the same time as nanoparticles are grown in the developing matrix was reported by Nakao et al.[74]. Inorganic nanoparticle precursors were dispersed in the organic monomers and nanoparticle growth was initiated. The growing metal surface can catalyze or even initialize the polymerization creating a self-dependent complex system.

Blending

The easiest method to prepare polymer-inorganic nanocomposite materials is achieved simply by mixing the two previously synthesized components either diluted with an appropriate solvent (*solution blending*) or without dilution in the melted state (*melt blending*). Solution blending is a frequently used method[75] providing excellent dispersion of both components but it is facing the challenges of solvent cost and recovery. Mixing nanoparticles to a polymer melt followed by extrusion of newly formed hybrid material was performed by Zhao et al[76] and Erdem et al.[77].

2.5.3 Block Copolymer Domain Loading

Besides homopolymer matrices, self-assembled block copolymer domains can also serve as scaffolds for nanoparticles, providing an opportunity for a controlled placement closely spaced

in three dimensions. Depending on the kind of particles used, the material finds application in, e.g., solar cells, magnetic data storage devices or catalysis.

Driving Forces

In order to assemble nanoparticles in block copolymer domains, adequate energetic preconditions are required or the nanoparticles demix from the block copolymers due to enthalpic and entropic reasons. Nanoparticle coating strongly influences the enthalpy of mixing upon incorporation into a polymer domain. Shells simply consisting of short polymer chains of the same kind as the domain provide a neutral enthalpy of mixing ($\Delta G \cong 0$) (see figure 2.22), while coating with a different polymer causes bad enthalpic mixing preconditions ($\Delta G > 0$) resulting in demixing and/or agglomeration.
Coatings bearing functional groups compatible with the domain polymer can even generate negative enthalpys due to e.g. H-bonds ($\Delta G \leq 0$).[78–80].
A very effective approach is to take advantage of the affinity of certain functional groups (e.g. amines) to some metals. By using a very low ligand surface density on gold nanoparticles Kim et al. were able to assemble the particles selectively in PVP domains, using the vinylpyridine's affinity to gold surfaces.[81] As depicted in figure 2.20 the polymer ligands on the particle surface (black chains) can relocate to make room for the pyridine ligands (red hexagons) originating from the polymer domain.

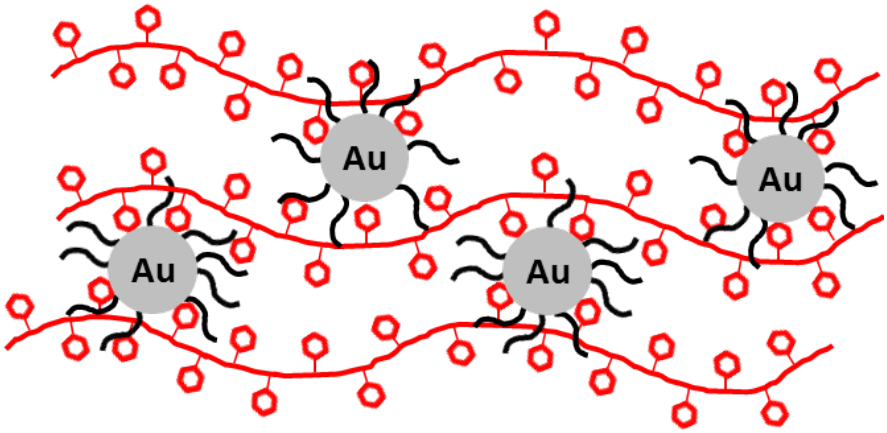

Figure 2.20. Schematic display of how interactions of certain functional groups with metal surfaces can be used to place nanoparticles in polymer domains.

Electrostatic interactions can be used similarly to bind nanoparticles to a certain spot in a block copolymer template. In 2012, Lunkenbein et al. used the negative charge of PMo^{3-}-ions for the interaction with PDMAEMA.[82]

A shell polymer bearing an ionic charge can be combined with a polymer domain bearing the opposite charge as depicted in figure 2.21. Here, the polymer domain bears functional groups with positively charged side chains. Besides the above mentioned PDMAEMA or PNIPAM further examples are block copolymers of poly-4- and -2-vinylpyridine (P4VP, P2VP) which are protonated under acidic conditions ($pH < 4.9$).[83] Adequate polymers with negative charges are polyesters like PMMA which are hydrolized under basic conditions to polyacrylic acid and poly(sodium styrene sulfonate). Also capillary forces have been used by Misner et al.[84] to

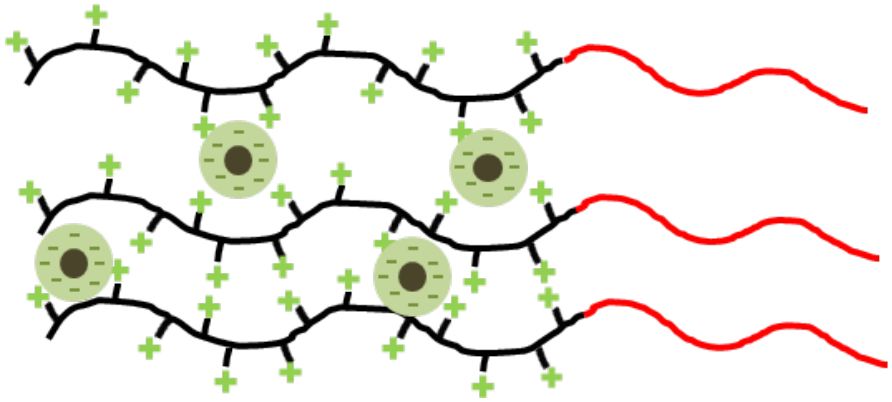

Figure 2.21. Illustration of negatively charged nanocomposite particles being placed in a polymer domain bearing positive charges.

"pull" CdSe nanoparticels size selective into porous polystyrene films by dip-coating.

In situ nanoparticle growth inside block copolymer domains has been reported by Thurn-Albrecht et al., who synthesized nanowires by direct current electrodeposition[85]. This way, self-assembled block copolymer morphologies can act as nanoscopic reactor spaces.[86]

Following the same goal, recently Madhavan et al. used the PS-P4VP membrane system mentioned above (section 2.3) to grow silver nanoparticles inside the pore channels. The metal precursors ($AgNO_3$) were introduced simply by immersing the pure membrane in an $AgNO_3$ solution. The silver ions were simultaneously bound by the basic nitrogen atoms of the pyridine side chains. Subsequent reduction using $NaBH_4$ yielded the nanoparticles.[87]

The entropy of mixing, on the other hand, is affected mostly by the particle size. Bending around large particles (relative to the domain size) implies a significant loss of conformational entropy, which usually results in the agglomeration of the particles in the domain center, where the polymer chains meet. Smaller particles are distributed inside the whole domain (dependent on the particle radius) because the chains can still arrange in a large variety of conformations, resulting in only a small decrease of entropy.[88,89] Figures 2.22a and b schematically illustrate the two described cases.

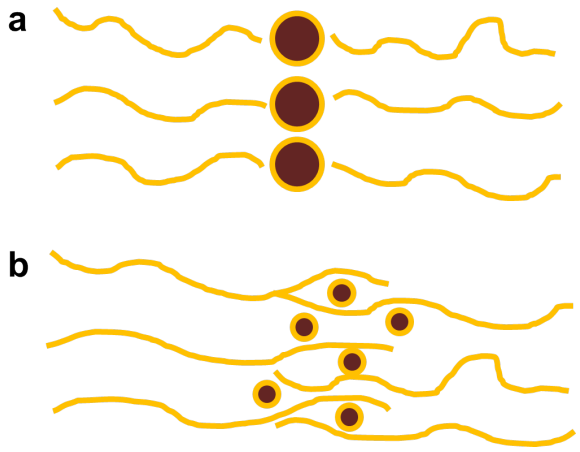

Figure 2.22. Influence of nanoparticle size on the placement inside a polymer domain consisting of the same kind of polymer as the ligand shell. Large particles (a) are located in the middle of a domain because of the great loss of conformational entropy upon deviating from the center. Small particles (b) can easily be enclosed by a polymer chain without losing a discernible amount of entropy. Thus, small particles are distributed all through the domain.

Nanoparticle shells consisting of two homopolymers

Mixed nanoparticle shells represent an interesting case, because it is not evident which domain the nanoparticle will assemble in. Assuming a self-assembly of the shell polymers in specific domains on the particle surface, a selective loading of the domain interface would be expected. Figure 2.23 shows an illustration, where the red shell polymers will reach into the red domain and *vice versa*, the yellow colored shell polymers will reach into the yellow domain. Here, there is no radius dependency of the nanoparticles concerning the location inside a domain. Large particles are simply expelled from the system, because a significant loss of conformational entropy is inevitable.

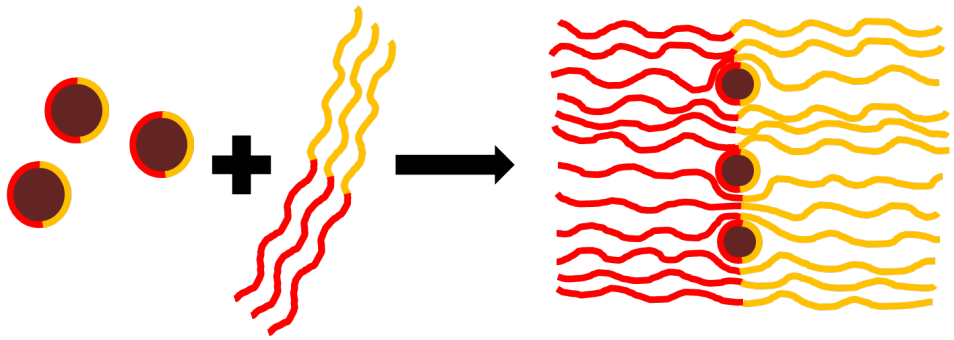

Figure 2.23. Schematic model of interface-specific domain loading with mixed-shell nanoparticles. Assuming a local phase separation of polymer ligands on the particle surface, the domain interface is the only sensible location for mixed-shell nanoparticles to assemble in.

Preparation approaches

Most ways to prepare inorganic-block copolymer-composite materials are performed from solutions with low concentrations in good solvents for both polymer blocks[90] or for only one block[91,92] following a simple blending-approach as described above (see section2.5.2). Figure 2.24 gives a schematic example.

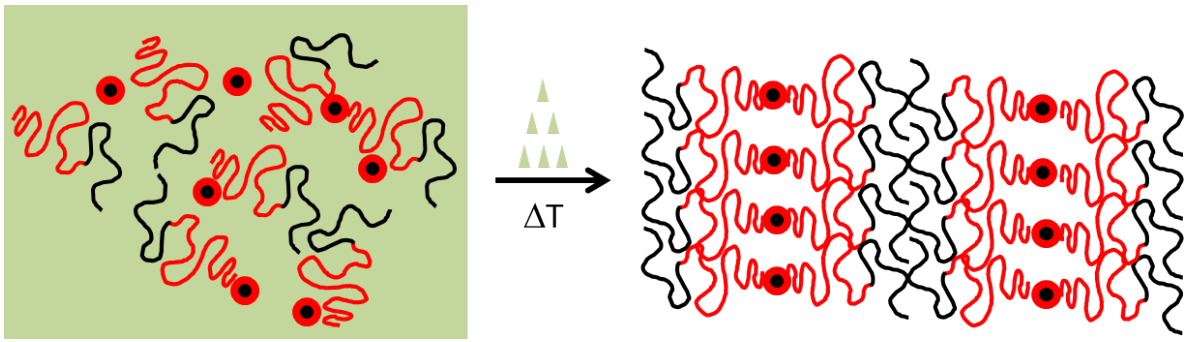

Figure 2.24. Schematic display of a simple blending approach to synthesize polymer-inorganic nanocomposites. The block copolymer chains form a random coil in an unselective solvent (green) while the nancomposite particles bearing a red shell are located near the red blocks. After solvent evaporation, the block copolymers have assembled in a lamellar structure, and have taken the particles in the center of the red domain due to enthalpic reasons.

These methods often produce structures that represent the thermodynamic equilibrium. The samples are usually annealed for several hours giving the system sufficient time and mobility to achieve energetic minimum.

However, using the previously described integral asymmetric membranes (see section 2.3) as templates for nanoparticles is different because it produces transient structures which do not resemble thermal equilibrium. Microphase separation occurs during the extremely fast evaporation of the volatile solvent THF, which locally increases the polymer concentration and induces self-assembly into block-rich domains. During this process, the particles are located near the corresponding polymer blocks and arrange in three dimensions while the domain structure develops.

3 Thesis Overview

This chapter is divided into three sections. The first is based on a paper recently published in Macromolecules (American Chemical Society, ACS)[93] dealing with microphase separation of PS-*b*-P2VP block copolymers in selective solvent mixtures during solvent evaporation. The full paper is given in chapter 4. As already explained in more detail in section 2.3, a system like this has been used for the formation of integral asymmetric membranes.[22,26,94] The process leading to pore formation is discussed while the second section focuses on an *in situ* method to study general characteristics during film formation of the described system. The findings were recently published in Macromolecules and are displayed in chapter 5. Here, modifications of the system in terms of molecular weight, block length ratio, and the addition of stabilizing agents are discussed. Moreover a crucial part of the membrane preparation process, the immersion in water, is investigated *in situ* for the first time.
Section three, as a completion, shows how the previously investigated membrane formation process can be utilized to place nanoparticles coated with polymer selectively inside the phase separated domains and even gain a distinct stabilizing effect for the porous surface structure. An impact on morphological transitions on the membrane surface was also determined. The whole manuscript is shown in chapter 6 and is also summarized below.

3.1 Topological Paths and Transient Morphologies during Formation of Mesoporous Block Copolymer Membranes

Highly viscous block copolymer solutions of PS-*b*-P2VP in solvent mixtures of DMF and THF form mesoporous and ordered surface structures after doctor-blading during solvent evaporation. The morphology is trapped upon immersion in water and shows extraordinary filtration performance as well as mechanical stability due to a thick, macroporous sublayer.[23–25]
The major challenge of the preparation process has so far been the empiric determination of the specific system parameters leading to pore formation. These include several independent variables, such as solvent composition, polymer concentration, immersion time, water bath temperature as well as ambient temperature and humidity.[95] Therefore a fundamental understanding of the phase separation process is of utmost importance and thus will be topic of this

section.
In the following, the structural evolution process leading to pore formation is discussed by means of calculated polymer volume fractions and trapped surface morphologies after systematic variation of the systems' composition. At last, the structure formation is observed in real time during solvent evaporation using synchrotron SAXS.

3.1.1 Calculation of polymer volume fractions

Considering the mentioned system, it is a useful first approach to understand the evaporation kinetics of the binary mixture of THF and DMF and the effect of a changing solvent composition on the block copolymer.
Due to their unequal solubilities in the two solvents the polymers will swell to different, variable extends which depend on the ratio of the two solvents. The overall composition determines the systems morphology and is given by the volume fractions of the solvent swollen polymer blocks.
Assuming that initially THF is the only evaporating solvent, the solution composition of the top layer of a cast membrane during evaporation was simulated. For this purpose, the swelling coefficients of each polymer block for the two solvents as well as measured evaporation rates of the pure solvents had to be taken into account. The corresponding compositional trajectories of different immersion times were mapped in a ternary phase diagram, as shown below. Here, it was assumed that the solvents evaporation rates are uninfluenced by the solution composition.
Figure 3.1a shows the calculated ternary phase diagram providing insight into the volume fraction of the P2VP block *via* the color scale. Besides the calculated trajectories (black dots) the diagram shows a distinct intermediate rise of the P2VP volume fraction of up to 0.6 (green region located in the middle-left) during solvent evaporation where the polymer concentration and DMF content are high. As illustrated in the following discussions (section 3.1.2) this region contains many phase transitions relevant for gaining full insight into the whole evaporation process.

3.1.2 Systematic variation of the solution compositions

In order to cover the whole range of possible solution compositions several series of water-trapped membranes in different solvent mixtures and with varying evaporation times were prepared.

Four characteristic morphologies were found during investigation with AFM, starting with a spinodal-type network structure (SpN) for large THF contents very similar to the sponge-like support layer below the surface (see section 2.3). Its dimensions shrink with a decreasing amount of THF in the solution. This trend is observable down to an approximate THF content of 50wt% in the solvent mixture. Lower initial THF contents rendered a disordered network of percolated spheres also with composition dependent diameters which at first shrink but then swell with a decreasing amount of THF. Consequently percolated sphere networks (SN) are found in the DMF rich part of the phase diagram (lower left part of figure 3.1a).

The observed swelling/collapsing behavior, as already partly been explained in section 2.3.1, is related to the different solubilities of the polymer blocks in the two solvents. When the solution loses THF the polystyrene block rapidly collapses because solvent quality becomes selective for P2VP. This explains the primary decrease of dimension for the spinodal network whereas after complete THF evaporation the P2VP blocks swell accounting for the increase in dimension for high DMF contents.

Following the trajectory that starts in the SpN phase inevitably leads to the formation of a highly ordered mesoporous PS matrix with spherical to cylindrical pores (PN) in the moment when the complete available volume of THF is taken up by the PS block. Automatically, the P2VP block is left to line the pore edges. The pore network is the first morphology in the SSL regime (see figure 3.1c) and it is directly followed by an ordered cylindrical phase (OC) when moving along the compositional trajectory. When the PS matrix breaks apart but is still mobile enough for adjacent cylinders to interact and arrange parallel, the OC phase appears.

The percolated sphere network (SN) agglomerates to disordered cylinders (DC) similar to a pearl necklace when the polymer concentration is increased upon evaporation. However, if the initial THF content is sufficiently high, for a very short period of time the PN phase is passed when the percolated spheres concentrate and arrange hexagonally. Pores are formed upon immersion when water penetrates the DMF swollen P2VP domains. The four characteristic morphologies are displayed in figure 3.1b.

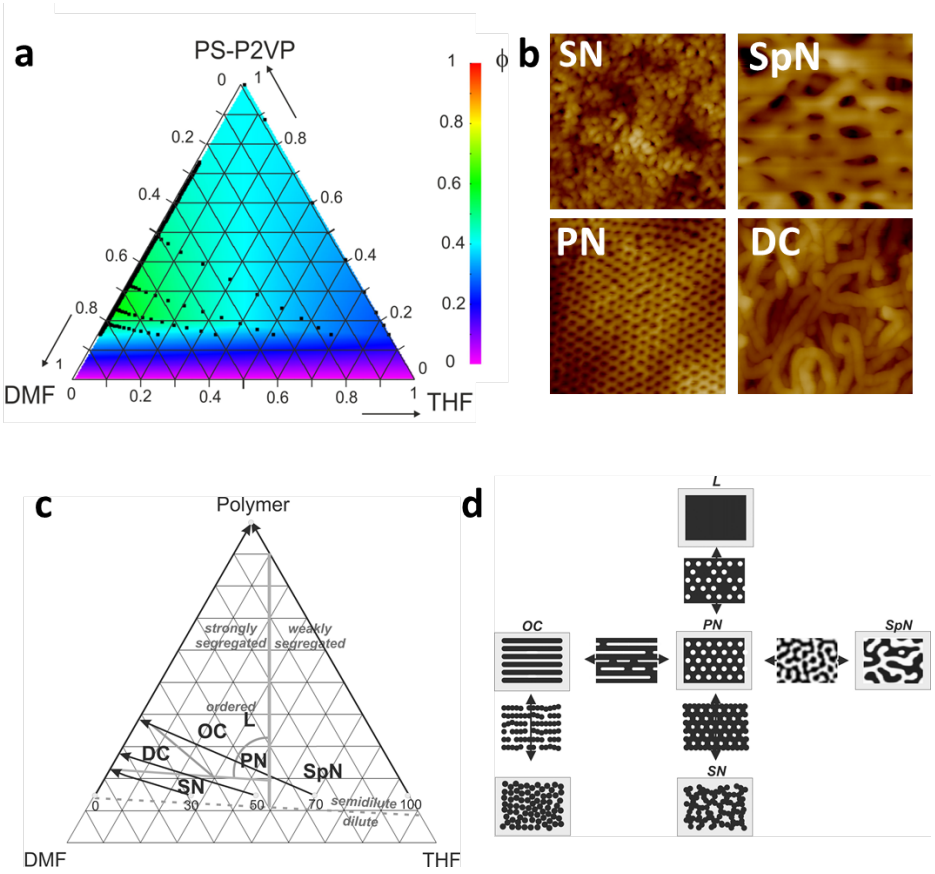

Figure 3.1. (a) Calculated ternary phase diagram displaying the relative P2VP volume fraction *via* the color scale with outlined evaporation trajectories. (b) AFM images of the four characteristic morphologies found on water-trapped membrane surfaces which are placed in a schematic ternary phase diagram (c) together with other morphologies also observed. (d) Schematic explanation of the structure formation mechanism.

The stability regions of all appearing morphologies are summarized in figure 3.1c. The considered system of PS-*b*-P2VP block copolymer in DMF and THF is discussed only near by or above the boundary of semi-dilution (gray dotted line), where polymer-polymer interactions become important making film formation most likely. The diagram also includes the boundary between weakly segregated (WSL) and strongly segregated compositions (straight gray lines) and the estimated trajectories being passed during evaporation (black arrows). Beside the morphologies described above (SpN, SN, PN, DC and OC) also perpendicular lamellae (L) are found. These appear after longer evaporation times when the system has reached the final dry state.

All these morphologies are kinetically trapped structures frozen by water immersion after cer-

tain measured evaporation times. Relating the morphologies to calculated volume fractions required the assumption of a negligible influence of the immersion bath on the developed morphologies.
A comparison between fig 3.1a and c quickly shows that the previously mentioned region of increased P2VP volume fractions (green area) corresponds well to the stability regions of the phases beside the PN phase outlined in figure 3.1c located in the middle-left of the diagram. It is important to note that the desired pore structure exists only shortly before the P2VP volume fraction begins to rise.
Figure 3.1d gives a schematic explanation how the desired porous morphology is formed. The schematic images are positioned according to their observance in the ternary phase diagram.

3.1.3 *In situ* SAXS investigation of the casting solutions of trapped membranes

The corresponding casting solutions of the trapped membranes were also studied *in situ* during film formation using synchrotron SAXS. An automatic film casting apparatus was therefore developed and will be described in more detail later. (section 3.2) The experiments rendered information about a characteristic length scale d^* in the evaporating solution which suggested growing structures for all solvent compositions except pure THF. The data were analyzed as discussed below to gain the structural development of d^* with time. A simultaneous development towards a plateau value d_∞ for all DMF containing solutions becomes apparent. Figure 4.11 shows the obtained length scales. The relative growth is related to the initial solution composition whereas high DMF contents rendered the highest relative increases. The micellar cores swell when THF evaporates as was evident from AFM images oft trapped membranes (section 3.1.2). Samples with a high initial THF content show the lowest relative increases because the polymer concentration is already too high to enable complete chain unfolding, when the DMF content becomes sufficiently high. The solutions in pure THF show much smaller length scales because the trajectory (see figure 3.1c) is located in the weakly segregated region of the phase diagram. d^* slightly decreases upon evaporation but since no preferential solvation occurs, no phase separation is induced and the length scale remains small. In the following section the applied *in situ* SAXS method will be explained in detail together with the developed apparatus. A similar block copolymer system also frequently used for membrane preparation (PS-P4VP) is investigated here in terms of molecular weight, block length ratio and

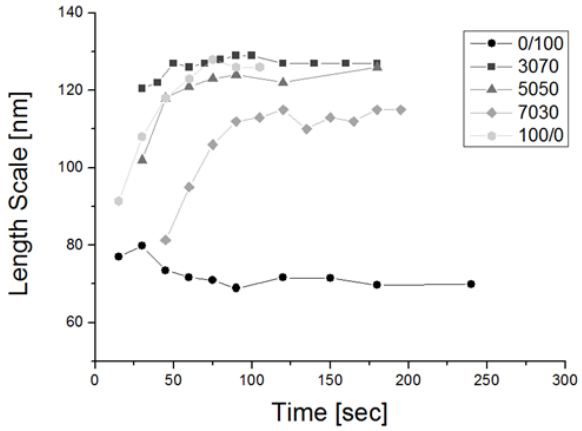

Figure 3.2. Structural evolution of the characteristic length scale d^* of each casting solution with varying solvent compositions. DMF/THF : 0/100 (black circle), 30/70 (black box), 50/50 (gray triangle), 70/30 (gray diamond), and 100/0 (gray circle).

stabilizing metal salts. After slight modification, the apparatus was also used to investigate the immersion process in water.

3.2 Evaporation-induced Block Copolymer Self-assembly into Membranes Studied by *in situ* Synchrotron-SAXS

In order to back up the assumption that water immersion does not influence the obtained morphology, an analogous systematic investigation of the evaporation process was conducted *in situ* using synchrotron SAXS. An automatic film casting apparatus was therefore developed which can be placed in a synchrotron beam and allows monitoring the evaporation process *in situ*. Figure 3.3a shows a schematic drawing of the device.

The apparatus uses tape *(Tesafilm ®, 1)* as an X-ray-transparent support material which is pulled around three guide rollers (2) and driven by a motor. The polymer solution is transported to the doctor blade (3) on top of the apparatus using a syringe pump, which is positioned directly above the gap. It is cast into a smooth film simply by the motion of the tape and moved to the spot to be probed by the X-ray beam (4). All parts are remotely controllable, a circumstance which is particularly important when dealing with fast evaporating systems. Solution casting can be started from outside the synchrotron hutch and the measurement is started right after casting with a constant dead time limited by the distance between doctor-

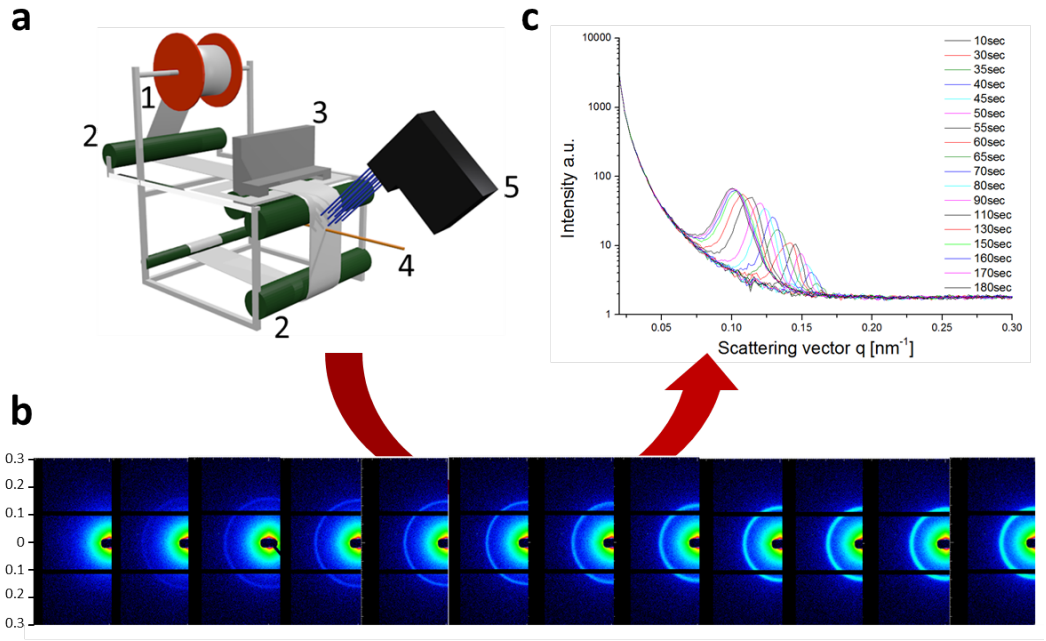

Figure 3.3. (a) Schematic drawing of the designed apparatus. The setup includes an inkjet printer (5) for the simulation of a water bath. (b) Series of collected scattering patterns obtained after evaporation times of 25, 30, 35...s. The evaporation was monitored for three minutes while each measurement frame was accumulated for five seconds. (c) Sectorally averaged and background subtracted scattering intensities. The shifting Debye-Scherrer ring is clearly evident with rising evaporation time.

blade and X-ray beam and by the tape velocity.

Depending on the type of sample, kinetic measurements can be conducted in different ways. The apparatus is adjustable in multiple positions, allowing to change various parameters, such as casting speed or film thickness. Also shear effects on evaporating systems can be examined by simply using a different doctor-blade. A GISAXS setup can be realized by choosing the measuring spot to be on top of the device. In addition, different support materials can be used.

The polymer system described here requires the usage of a precipitation bath (water) after a short evaporation time. For this reason, an additional set up was developed where water was sprayed onto the evaporating film after a certain, adjustable time. The wetted spot was subsequently moved into the X-ray beam to probe the changes after immersion. This was realized by using an inkjet printer and positioning it as close to the measuring spot as possible. The

inkjet printer is also shown in figure 3.3.
For SAXS/SANS-transmission measurements the sample solutions require an adequate, ("honey-like") viscosity in combination with an appropriate flow rate of the syringe pump, guaranteeing a mechanically stable film even in vertical position.

The investigated block copolymer system PS-*b*-P4VP in a solvent mixture of DMF and THF shows rapid changes of the surface morphologies during evaporation of THF as has been shown in various series of water-trapped membranes during the past years.[26,27,29,96]
In order to get useful information about any structural evolution in the evaporating solution, a temporal resolution of at least 10 s or less is necessary. The instrumental setup therefore used consisted of a high energy synchrotron X-ray source in combination with a highly sensitive 2D detector with a very low read out time.
After casting, the polymer film is transported to the measuring spot as fast as possible and stopped. The time needed to reach the spot defines the measurement's "dead-time" and is added to the evaporation time for each measurement frame.
The complete measurement consists of a series of short frames, the time for each frame identifying the temporal resolution of the information gained from the collected data.

3.2.1 Performed Experiments and Data Evaluation Approach

In general, the collected scattering patterns for each series were very similar suggesting no significant differences in the structural evolution during evaporation. In the first few seconds no structure had yet developed which was indicated by featureless scattering patterns expected for the SpN phase included in figure 3.1b. After some time, 20-40 s depending on the solvent mixture, a single Debye-Scherrer ring appears signaling the beginning of microphase separation. It shifts towards the beamstop implying a fast increase of structural dimension well in line with the observations obtained from AFM images of water trapped membranes (see section 3.1.2) and the calculation of polymer volume fractions (section 3.1.1).

An exemplary series of scattering patterns is shown in figure 3.3b. The ring first appears after 30 seconds and shifts for approximately two minutes. Meanwhile, it becomes more intensive and the diffuse background rises. The peak position q* is easily transferred into the characteristic length scale d* *via*

$$d^* = \frac{2\pi}{q^*} \tag{3.1}$$

Figure 3.3c shows the scattering intensities obtained after background subtraction and azimuthal averaging. The position of the Debye-Scherrer ring clearly shifts from approximately $q^* = 0.16$ to $q^* = 0.1$. Plotting the calculated length scales against the evaporation time renders a graph tracing the temporal evolution of the solution's characteristic length scale. All measurement series were treated and evaluated analogously.

Since the used polymer system might influence the membrane formation process, two parameters, molecular weight and block length ratio, were varied to identify possible consequences. For large molecular weight block copolymers, the Debye-Scherrer ring was found to appear earlier and the shift to be completed sooner than for smaller polymers suggesting faster phase separation kinetics.

A block copolymer with a different relative volume ratio principally produces the same results. The isotropic Debye-Scherrer ring appears a few seconds after casting and shifts towards the primary beam.

Since several research groups have added metal salts to the casting solution for complexation (see section 2.3.1), the influence of these additives was investigated also. Similar to the other samples, the measurements using polymer solutions including a small amount of copper(II) chloride showed no significant difference. However, the obtained length scales were slightly smaller which is explained by the copper(II) ions binding to the P4VP groups *via* their basic nitrogen atom. The temporal evolution of the length scales evolved in parallel to a sample without salt additive.

Figure 3.4a shows all structural developments discussed so far for comparison (dotted lines). It becomes evident that in each case the calculated length scales develop similarly and reach a plateau value d_∞ after a period of time depending on molecular weight and block length ratio. All experimental data can be described by an exponential saturation fit following the general equation

$$d^* = d_\infty(1 - exp(-t/\tau)) \tag{3.2}$$

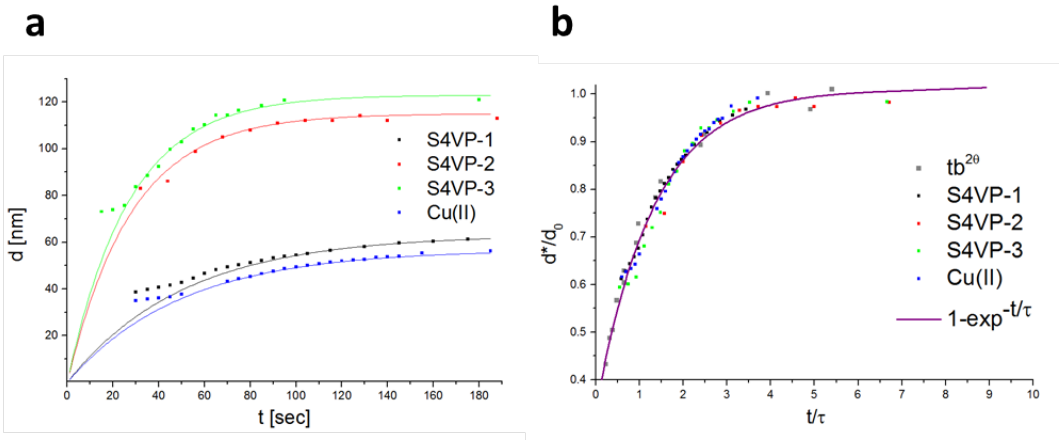

Figure 3.4. (a) Graphic display of the obtained length scales (dots) of the reference polymer S4VP-1 (black), a polymer with a lower hydrophilic volume fraction (S4VP-2, red), a higher molecular weight polymer (S4VP-3, green), and the reference polymer including 0.15 wt.% of copper(II) chloride (Cu(II), blue). The corresponding exponential saturation fits are represented by the solid lines. (b) Mathematical transformation using the determined parameters for d_∞ and τ along with a calculated polymer domain growth line (gray) by Podariu et al.

The fitted lines reveal certain characteristic parameters of the polymer system, such as the plateau value d_∞ and the characteristic growth time τ. These values are employed to prove the similarity of all observed evaporation series. Plotting the calculated length scale d^* divided by the plateau value for each series d_∞ against time divided by τ renders four graphs following the same exponential rise proving the distinct similarity of the evaporation kinetics and phase separations. Figure 3.4b shows the obtained graphs.

The results agree with theoretical studies by Podariu et al[97], who calculated block copolymer domain growth towards an upper limit given by the block copolymer. Their simulated domain dimensions can be transformed to fit the data by simple mathematical modifications and are also displayed in figure 3.4b (gray squares).

Since all discussed evaporation series were based on solutions in the same solvent mixture, the structural evolution is obviously directly connected to the altering solvent composition and principally independent of the observed polymer system. All that is observed during film formation is a continuous growth of P4VP domains due to the developing preferential solvation, starting from an initially weakly segregated state to a strongly segregated state with different surface morphologies summarized in figure 3.1.

Trapping the structures on the surface with water is a crucial step of membrane formation but has not been investigated in detail so far. Therefore, an inkjet printer spraying water onto an evaporating PS-P4VP solution after approximately 45 and 30 seconds respectively was included in the set up and the process was monitored with *in situ* SAXS.

A sudden and rapid shift of the Debye-Scherrer ring in the scattering patterns (see Figure 5.6) indicated an abrupt increase of the characteristic length scale in the polymer film upon immersion. Within one measurement frame, the length scale d^* jumps excessively followed by only slight changes towards the plateau value d_∞ obtained from slowly drying samples. Thus, the performed water immersion with the inkjet printer did not, as expected, trap the film morphology effectively. If this had been the case, the length scale would have remained constant after immersion. All samples measured several hours later showed to have lost their surface morphology, indicating further structural changes which are not known from the usual membrane formation process. These findings point out the importance of the water immersion step in general and of a sufficient excess of water in particular.

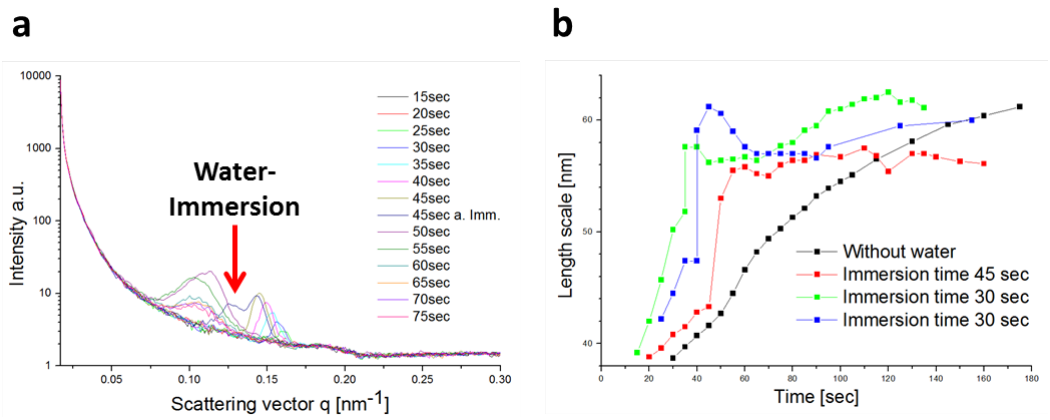

Figure 3.5. (a) Scattering intensities and (b) calculated length scales of an evaporation series of a solution of the reference polymer S4VP-1 comparable to the series discussed in figure 3.3. Water was sprayed on the film after approximately. 45 s (red squares) and 30 s respectively (green and blue squares).

3.3 Functionalization and Stabilization of Self-Assembled Blockcopolymer Membranes by Nanoparticles

In the third part of this chapter, a way to ordered self-assembled nanoparticles in a block copolymer matrix is introduced where the discussed highly porous membrane structure is used to arrange iron oxide nanoparticles controllable in three dimensions.
Section 3.1 has already described how block copolymer self-assembly is utilized to prepare highly symmetric and porous film surfaces. Also, the complicating circumstances this structure is formed under are discussed. Finding a way to overcome these experimental difficulties is particularly important for large-scale membrane preparation. Extending the time frame for stable pores is essential to achieve optimal separation selectivity and efficiency. In the following, it is described how the synthesized nanocomposite particles affect the phase separation in the above discussed PS-P2VP polymer films (see section 3.1).
The next sections will show that the formation of these structures can be promoted using inorganic-organic composite particles of nanometer size which direct the self-assembly of the block copolymers. Improved ordering is thereby achieved and, in addition, an easy possibility to arrange nanoparticles in close proximity is provided giving rise to several nanotechnological applications.
The principle of nanocomposite preparation and the main impacts of their addition to membrane casting solutions are summarized in the following.

3.3.1 Nanocomposite materials

As explained under 2.5.3, in order to achieve a selective placement of nanoparticles in a specific block copolymer domain, one approach is to coat the nanoparticle surface with a layer of the correspondent homopolymer. Since the channels of the membranes described in section 3.1 are lined with poly-2-vinylpyridine, it is sensible to coat the nanoparticles with short chains of the same polymer to achieve a placement in the channels.
To prepare the homopolymer ligands, poly-2-vinylpyridine was synthesized *via* anionic polymerization in THF following established procedures.[98] The reaction was terminated with ethylene oxide, thus introducing a functional hydroxyl-group that provides the opportunity to add functionality to the polymer.

After the synthesis, the nanoparticles are stabilized with oleic acid which has to be replaced by polymer ligands bearing basic functionalities in order to quantitatively bind to the nanoparticle surface. Amino and carboxyl-groups have proven to be useful for this purpose.
For attaching an amino group, the hydroxy-terminated polymer is activated with excess CDI (1,1'-Carbonyldiimidazole) and, in a second reaction, converted into an amine *via* a simple addition-elimination mechanism. A reaction scheme is shown in figure 3.6.
The ligand exchange is performed by simply mixing the nanoparticles and the ligand polymers in a good solvent followed by precipitation and redispersion.[99]

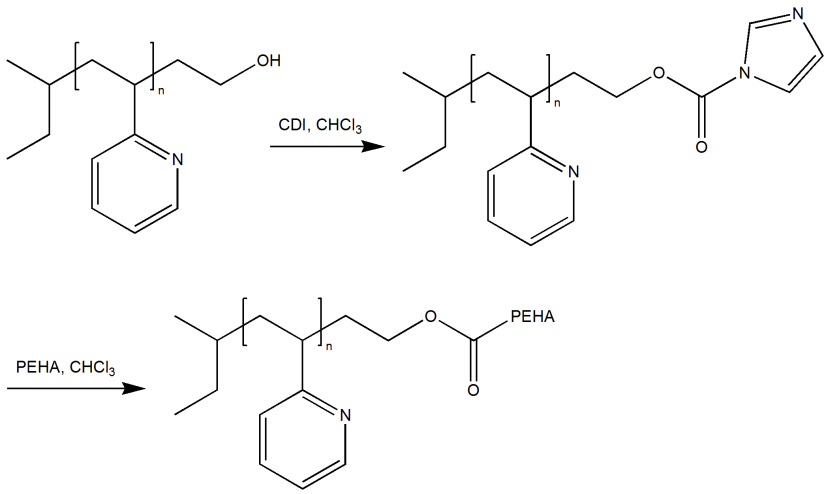

Figure 3.6. Reaction scheme of the polymer activation and functionalization. Both reactions are conducted in chloroform at room temperature over night.[100]

Multivalent organic amines such as diethylene triamine (DETA) or pentaethylene hexamine (PEHA) show maximum binding efficiency and provide optimal entropic conditions for the ligand exchange because they occupy multiple binding positions on the nanoparticle surface. For this study, magnetic iron oxide nanoparticles were used because of a possible application of their magnetic properties and good contrast in electron microscopy. Figure 3.7 shows TEM images of the synthesized particles coated with oleic acid (c), with P2VP (d) and with PS (e). Single and separated particles are visible on each image suggesting a dense polymer layer around each particle and a successful ligand exchange. Figure 3.7a displays size distributions of particles before and after ligand exchange with P2VP homopolymers of different molecular weights measured by dynamic light scattering. A shift towards larger radiuses is

only recognizable for the particles before and after ligand exchange. However, an effect of the molecular weight of P2VP on the hydrodynamic radius was not observed which is explicable taking into account the binding nature of P2VP. Here, every repeating unit bears a basic functionality which contributes to the binding nature described as "train-like", meaning that the P2VP chains occupy large surface areas but do not reach very far into the surrounding solvent. For visualization, figure 3.7 includes a schematic drawing.

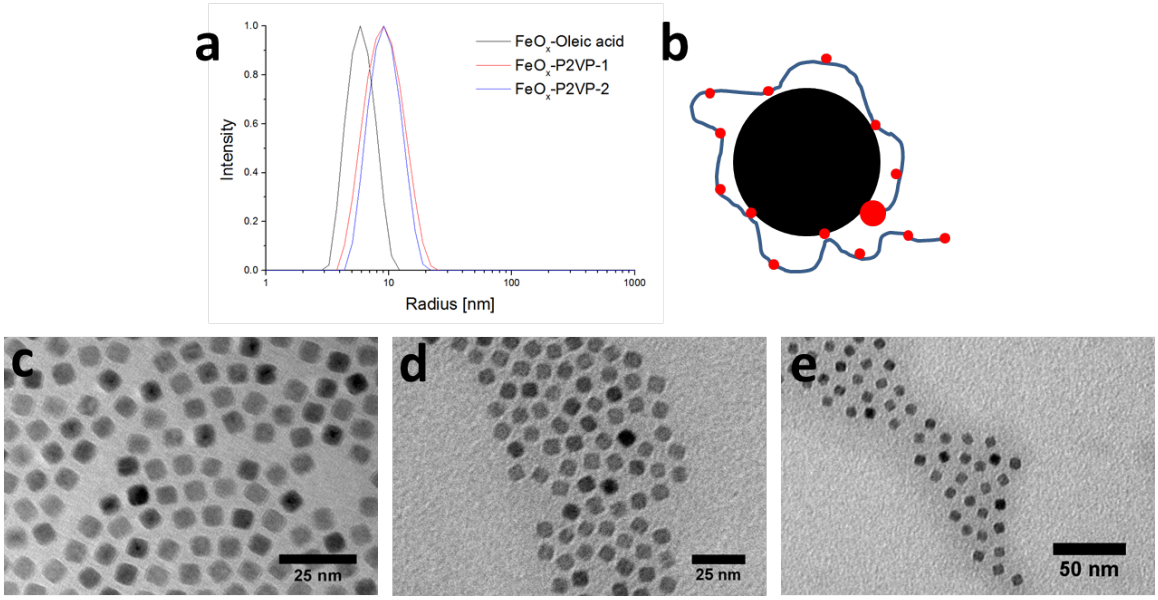

Figure 3.7. Particle size distributions obtained by DLS of P2VP coated Fe_2O_3 nanoparticles (a) and a scheme illustrating the binding nature of the P2VP ligand (b) The small red dots represent the pyridine side groups of every repeating unit while the larger red dots corresponds to the amino anchor group. TEM images of the prepared nanocomposite batches. The shells consist of (c) oleic acid, (d) P2VP and (e) PS.

3.3.2 Embedding of nanocomposite particles in block copolymer domains

For the embedding experiments the polymer-coated nanocomposite particles in low concentrations were blended with the PS-P2VP polymer and the membrane preparation was performed analogously to the above described procedure (see section 3.1). Nanocomposite particles with shells consisting of different mixtures of these polymers were used for membrane

fabrication. The obtained film surfaces were characterized with AFM, followed by embedding of small membrane pieces in a epoxy resin to enable the preparation of ultrathin sections of the material giving insight into the films interior using TEM.

The impact of the nanocomposite particles in general and of the polymer shell mixture in particular on the surface morphology is investigated and discussed in the following section.

In general, the addition of nanocomposite particles causes the porous matrix to be formed earlier than without the addition of particles which is independent on the composition of the shell. As evident from figure 3.8a, pore formation for nanocomposite membranes starts below 5 seconds instead of at around 10 seconds. Contents of only 1 wt.% produce stable porous surfaces over up to 20 s which is considerably longer compared to pure PS-P2VP membranes (compare line 1 in figure 3.8a to lines 3, 5, and 7) A complete set of AFM images is shown in chapter 6 for confirmation.

For slightly lower nanocomposite content (0.5 wt.%), the morphological transition from pores to cylinders mentioned in section 3.1.2 was observed rather early especially concerning membranes with a high P2VP content in the nanoparticle shell. Lines 2 and 4 in figure 3.8a make this evident. The transition expected after 20 s or later (see line 1) occurs already after 8 s and 11 s respectively. The nanoparticle batch coated mostly with PS shows no difference concerning the evaporation time the phase transition is observed.

These findings are explicable taking the P2VP volume fractions of the complete system into account. It was already discussed in section 3.1 that a pore-cylinder transition occurs when the overall P2VP volume fraction exceeds a certain value (approx. 50%). Since the nanoparticles are coated with mixtures of PS and P2VP homopolymers, these add up to the overall volume fractions of the blocks. Particles with the largest P2VP shell content (red series) therefore have the biggest influence. Theoretically, the higher the initial P2VP volume fraction, the sooner a pore-cylinder transition can be expected which is well in line with our findings. The corresponding AFM surface images are also shown in chapter 6.

These results already proof that the particles interact specifically with one polymer domain. In order to get visual confirmation, ultrathin membrane sections were prepared for TEM characterization. Two images are shown in figure 3.8b and c. Here, the extreme cases of a pure polymer coating were chosen in order to illustrate the different placements more clearly. The PS coated particles are clearly located in the middle of the cylindrical domains, while the P2VP coated particles assemble in the darker P2VP domains in-between.

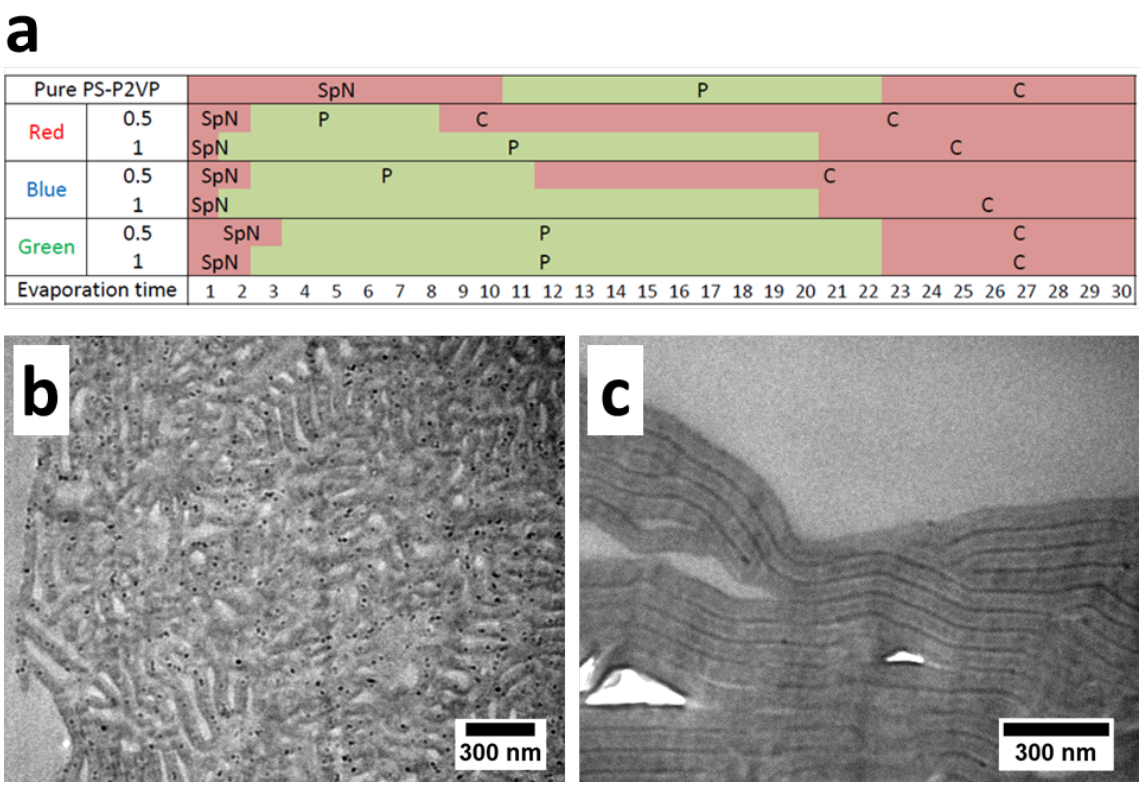

Figure 3.8. (a) Schematic summary of morphologies found on nanocomposite membrane surfaces after different evaporation times. The films contained nanoparticles coated with mixtures of PS and P2VP in three different ratios. The P2VP contents were: 70% (red); 50% (blue); 30% (green). TEM images of thin sections of membranes containing nanoparticles coated with (b) pure PS and with (c) pure P2VP.

For the experiments using the mixed shell nanocomposites, expectations concerning the placement in a domain were based on the results just presented. Generally, all nanocomposite particles are expected to be located near the domain interface because the shell consists of both block polymers. Particles with a high PS shell content are expected to reach into the large PS domains while all other particles would be located very close to the narrow P2VP domains making a visual determination impossible. TEM images shown in chapter 6 confirm the expectations.

3.4 Individual Contributions to joint Publications

The results summarized above were obtained in close collaboration between different people and are displayed as published in the following three chapters. The next section indicates the contribution of each coauthor. The corresponding author is marked with an asterisk.

Chapter 4

This work is published in *Macromolecules* **2014**, *47*, 5566-5577 with the title:
"Topological Paths and Transient Morphologies during Formation of Mesoporous Block Copolymer Membranes"
by Corinna Stegelmeier, Volkan Filiz, Volker Abetz, Jan Perlich, Andreas Fery, Pia Ruckdeschel, Sabine Rosenfeldt, Stephan Förster*

I synthesized the polymers S2VP-2 and S2VP-3 and performed most of the experiments including the SEM characterization as well as *in situ* SAXS measurements. I wrote the manuscript and also supervised *Pia Ruckdeschel*, who prepared most membranes and performed AFM characterization.
Jan Perlich was responsible for the instrumental set up during the *in situ*-SAXS measurements.
Andreas Fery, *Sabine Rosenfeld*, *Volkan Filiz* took part in discussions.
Volker Abetz supervised and coordinated the *SELFMEM* project and took part in discussions.
*Stephan Förster** corrected the manuscript, performed the theoretical calculations and took part in discussions.

Chapter 5

This work was published in *Macromolecules* **2015**, *48*, 1524-1530 with the title:
"Evaporation-induced Block Copolymer Self-assembly into Membranes Studied by *in situ* Synchrotron-SAXS"
by Corinna Stegelmeier, Alexander Exner, Stephan Hauschild, Volkan Filiz, Jan Perlich, Stephan V. Roth, Volker Abetz, Stephan Förster*

I synthesized the polymers S4VP-1 and S4VP-2, performed the major part of the *in situ* SAXS experiments, and wrote the manuscript.
Alexander Exner contributed to designing the film-casting apparatus, helped with the SAXS measurements, and took part in discussions.
Stephan Hauschild constructed the remote control of the film-casting apparatus and provided the inkjet printer.
Volkan Filiz provided the polymer S4VP-3 and the SEM images of corresponding membranes.
Jan Perlich and *Stephan V. Roth* were responsible for the instrumental set up during the *in situ*-SAXS measurements.
Volker Abetz supervised and coordinated the *SELFMEM* project and took part in discussions.
*Stephan Förster** corrected the manuscript and took part in discussions.

Chapter 6

This work is intended for submission with the title:
"Functionalization and Stabilization of Self-Assembled Blockcopolymer Membranes by Nanoparticles"
by Corinna Stegelmeier, Sara Mehdizadeh Taheri, Sascha Ehlert, Katharina Ottermann, Andreas Fery and Stephan Förster*

I wrote the manuscript, synthesized the polymers, performed all TEM and SEM measurements and supervised *Katharina Ottermann* who prepared the membranes, and the ultrathin sections and performed the AFM characterization.
Sascha Ehlert performed the TGA measurement.
Sara Mehdizadeh Taheri provided the iron oxide nanoparticles.
Andreas Fery took part in discussions.
*Stephan Förster** corrected the manuscript and took part in discussions.

4 Topological Paths and Transient Morphologies during Formation of Mesoporous Block Copolymer Membranes

[1]*Corinna Stegelmeier,* [2]*Volkan Filiz,* [2,3]*Volker Abetz,* [4]*Jan Perlich,* [5]*Andreas Fery,* [1]*Pia Ruckdeschel,* [1]*Sabine Rosenfeldt,* [1]*Stephan Förster*

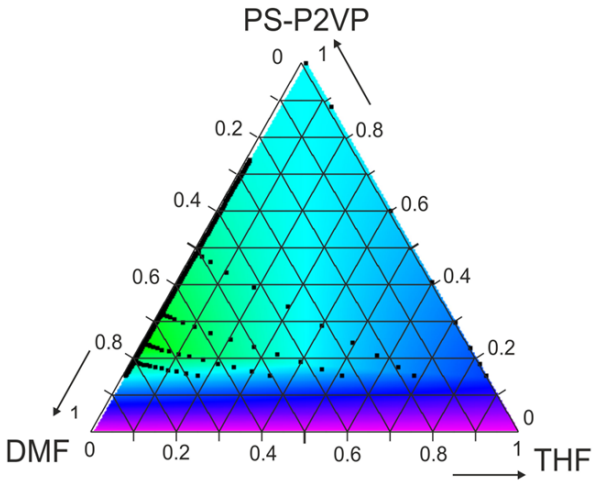

[1] Physical Chemistry I, University of Bayreuth, Universitätsstrasse 30, 95447 Bayreuth, Germany

[2] Institute of Polymer Research, Helmholtz-Zentrum Geesthacht, Max-Planck-Strasse 1, 21502 Geesthacht, Germany

[3] Institute of Physical Chemistry, University of Hamburg, Grindelallee 117, 20146 Hamburg, Germany

[4] Deutsches Elektronen-Synchrotron DESY, Notkestrasse 85, 22607 Hamburg, Germany

[5] Physical Chemistry II, University of Bayreuth, Universitätsstrasse 30, 95447 Bayreuth, Germany

4.1 Abstract:

We systematically investigated the structure formation pathways and transient morphologies involved in the formation of mesoporous membranes by the self-assembly of block copolymers during nonsolvent induced phase separation. Using AFM, SEM, and *in situ* synchrotron SAXS, we mapped the topological paths and characteristic transient structures into a ternary phase diagram. We focused on the stability region of an ordered pore phase which is relevant for the generation of integral asymmetric isoporous membranes. We could identify several characteristic morphologies, i.e., spinodal networks, sphere percolation networks, ordered pore structures, and disordered and ordered cylinder arrangements together with transient structures connecting their stability regions. With given evaporation rates for the pure solvents, we calculated the corresponding composition trajectories in the phase diagram to identify suitable experimental conditions in terms of initial polymer volume fraction, solvent composition, and immersion time to trap the desired pore structure.

4.2 Introduction:

The self-assembly of amphiphilic diblock copolymers has been exploited in many areas of material science.[8] A recent fascinating example is the spontaneous formation of integral asymmetric membranes which are of high interest in devices for water purification and protein separation.[22] Their formation utilizes the combination of self-assembly and nonsolvent-induced phase separation.

The method involves dissolving an amphiphilic block copolymer in a mixed-solvent system to produce a casting solution, which is doctor-bladed into a film. The solvent is then evaporated for a period of tens of seconds before immersing the film in a coagulation bath containing a nonsolvent, mostly pure water, to induce phase inversion. A significant concentration of a highly volatile solvent in the solvent mixture leads to the formation of a dense nanoporous skin during evaporation. Remarkably, this simple procedure yields in one step integral asymmetric isoporous membranes with a high density of uniform open pores (typically > 1014 pores/m^2) in the top separation layer above a macroporous, asymmetric substructure providing mechanical support. This is a very efficient preparation procedure for an ideal structure for applications in nanofiltration devices.

The first reported and most often used block polymer/solvent system is poly(styrene-*b*-poly-4-

vinylpyridine) (PS-P4VP) in a DMF/THF solvent mixture, using evaporation times of 10-20 s.[22] The original idea was further explored[26,27,94] with a better understanding of the mechanism of pore formation. Meanwhile, also other polymer/solvent systems were introduced such as PS-P4VP in a dioxane/THF/DMF mixture[101,102], poly(isoprene-*b*-styrene-*b*-4-vinylpyridine) (PI-PS-P4VP)[102–106], poly(styrene-*b*-2-vinylpyridine-*b*-ethylene oxide) (PS-P2VP-PEO)[29], PS-PEO[107], PS-P2VP[25], poly(*t*-butylsytrene)-*b*-4-vinylpyridine)[96], and poly(trimethylsilylstyrene-*b*-4-vinylpyridine)[96], all in binary or ternary solvent mixtures containing DMF and/or THF. Not only flat but also isoporous hollow fiber membranes have been prepared using this procedure.[108,109] In all these cases the films were prepared by partial evaporation of THF, which is the most volatile solvent, followed by immersion of the obtained film in water, a nonsolvent for the block copolymer. Upon evaporation the solvent mixture becomes selective for the P4VP- and P2VP-blocks because DMF is a much better solvent for these blocks than for PS. The procedure leads to a top layer of 100-300 nm thickness exhibiting well-ordered, open spherical to cylindrical pores perpendicular to the film surface with pore diameters between 20 and 100 nm.

During the short evaporation time the block copolymer self-assembles, and the formed morphology on the film surface is trapped by immersing the membrane in a nonsolvent bath (water). When varying process parameters it is found that only in a narrow range in parameter space stable mesoporous membranes are found. The complex parameter landscape associated with producing these membranes makes the identification of the optimal parameter set a considerable effort, and makes progress in this field a major challenge. Major parameters include block copolymer chemical composition, molar mass, casting solvent composition, solution concentration, and evaporation time. The big challenge is not only to direct the block copolymer assembly into the desired structures but also to stabilize this state against further structural changes to produce the desired nanostructured membrane.

A more detailed understanding of the membrane formation process would considerably aid to find optimal processing parameters. The goal of the work presented here is to investigate the structural transformations that are critical during the first minute of the membrane formation process where the crucial steps of the pore formation occur, including casting of the block copolymer solution, solvent evaporation after film casting, and immersion into water.

In order to get insight into the membrane formation process, we performed AFM, SEM, and in situ synchrotron SAXS experiments and varied evaporation time, polymer type, and solvent

composition. For AFM and SEM the sample structure after different evaporation times were trapped by immersion in water and then dried. *In situ* SAXS experiments were performed after doctor-blading the polymer solutions and measuring SAXS patterns during evaporation and immersion in water. We used polymer solutions of PS-P2VP in different ratios of tetrahydrofuran (THF) and *N,N*-dimethylformamide (DMF). We found the PS-P2VP system particularly suitable for this study because the stability region of the nanoporous structure is small, such that the neighboring morphologies in the phase diagram could be captured as well.

4.3 Experimental Part:

Block Copolymers

The PS-P2VP block copolymers were synthesized by sequential living anionic polymerization in tetrahydrofuran at $-70\,^{\circ}\mathrm{C}$ following procedures previously described in the literature[110]. The block copolymers used in this study are summarized in Table **??**. All polydispersities were < 1.10.

Table 4.1. Molecular Weights of the PS-P2VP Block Copolymers and Volume Fractions of the P2VP Blocks Used in the Present Study.

Polymer	M [g/mol]	f_v(2VP)
S2VP-1	295 000	0.25
S2VP-2	100 000	0.25
S2VP-3	160 000	0.29

Membrane Preparation

In order to determine an influence of the solvent composition on the phase separation behavior of poly(styrene-*b*-2-vinylpyridine) block copolymers several membranes were prepared from solutions containing between 10 and 15 wt% of polymer in solvent mixtures varying from pure THF to pure DMF via three mixing ratios. The evaporation times were varied between 0 and 60 s and the structures were fixed by immersing the polymer film in a water bath.

In Situ SAXS Film Formation Experiments

To follow the structural evolution in the polymer films during the membrane preparation pro-

cess, we performed *in situ* small-angle X-ray scattering experiments at the synchrotron beamline BW4 at HASYLAB/DESY. For this purpose an automatic film casting apparatus was developed. It casts a thin polymer film from a viscous polymer solution onto a moving support film. We used commercially available tesafilm, which is optically transparent and transparent to X-rays with negligible background scattering over the whole q-range of interest. The polymer solutions are continuously cast via syringe pumps and a doctor blade, which are positioned above the continuously moving tape. It is wound up by a motor with variable speed.
This setup allows one to prepare a homogeneous film with well-defined thickness in the range of $50 - 200\mu m$. The film is transported over rolls into the X-ray beam, which probes the film structure after a certain distance from the doctor blade, which depends on the films moving velocity. This position corresponds to a certain time after film preparation. Further details can be found in ref[111].

Synchrotron Small-Angle X-ray Scattering

The SAXS experiments were performed at HASYLAB/DESY Hamburg at the beamline BW4 ($\lambda = 0.138nm$) with a sample-detector distance of 11 m. For the detection of the scattering patterns a MarCCD camera was used.[112]

Atomic Force Microscopy (AFM)

The surface topographies of the polymer films were characterized using the Dimension 3100 NanoScope IV atomic force microscope. The images were detected using a standard silicon tip with a radius of 10 nm, and the instrument was operated in the intermittent contact mode with scan rates of 0.7-0.9 Hz. The obtained data were processed with the Nanoscope Analysis software.

Scanning Electron Microscopy (SEM)

For the characterization with SEM the block copolymer samples were sputter-coated with a platinum layer of 1.3 nm using the Cressington sputter coater 208HR. The film surfaces were characterized using a Zeiss LEO 1530 scanning electron microscope with a field emission electron gun. The instrument was operated at 2.0 kV, and the images were detected using an Inlens SE detector.

4.4 Results and Discussion:

Calculation of Composition Trajectories

In the following we develop and use a theoretical model to calculate the polymer/solvent composition of cast films as a function of time upon solvent evaporation. This allows one to construct time-composition trajectories in a ternary phase diagram, suitable to be compared with our experimental studies.

The idea of the solvent cast procedure is that during evaporation of the solvent β the solvent mixture becomes selective for the A-blocks, which induces microphase separation and a disorder-order transition into a cylindrical phase with solvent swollen, hexagonally ordered A-cylinders in a B-matrix. In the cast film, this process will start at the film surface, whereas the underlying film will still be in the solvent-swollen disordered state. Sudden subsequent immersion in a nonsolvent for both blocks will trap the B-matrix containing the cylindrical A-domains and induce a spinodal decomposition of the underlying solvent-swollen disordered phase to form a coarse porous network support structure. If immersed after the right evaporation time t* and subsequently dried, one obtains a mechanically stable integral asymmetric membrane exhibiting a top layer with cylindrical pores on an underlying coarse-pore membrane support layer. The difficulty in this process is to find a suitable AB-block copolymer, a suitable combination of solvents with different evaporation rates and interaction parameters χ, and the right evaporation time t^*, after which the cast film is immersed in the nonsolvent. In practice, these parameters have to be found empirically.

Upon evaporation, the composition of the ternary mixture of block copolymer, solvent α, and solvent β changes continuously. It would be desirable to map the compositional changes in the form of a trajectory into a ternary phase diagram and relate different positions on the trajectory to the cast film morphology and the evaporation time. It would then allow one to predict the starting composition and evaporation time t* needed to obtain an ordered pore morphology, which is the optimal and desired membrane structure. This task is complicated by three circumstances: (1) the cast film during evaporation has an inhomogeneous composition, with a low solvent content at the top where the solvent evaporates, a high solvent content at the bottom, and a vertical composition gradient in between, (2) calculations of compositions after certain evaporation times would have to be based on solvent evaporation rates, which themselves depend on the composition the cast film in a complicated way, and (3) it may be an

experimental difficulty to effectively trap the film morphology that has developed after a certain evaporation time because during immersion in water the morphology may further change.

To keep this study feasible, we (1) focus on the structural evolution of the top layer, which is most relevant for the membrane applications, (2) calculate and map evaporation times onto the trajectories based on solvent evaporation rates derived from the top layer composition, and (3) assume that the film morphologies trapped by the water-immersion method are close to the actual film morphologies. Water may in the very beginning of the immersion process increase the selectivity of the solvent mixture, thus moving slightly further upward the trajectory in the phase diagram, but within very short times effectively traps the structure of the polystyrene matrix, avoiding any further structural changes. With these assumptions in mind, we outline in the following the model calculation of the composition trajectories.

We consider an AB-diblock copolymer with a volume fraction f_A of the A-block with respect to the total dry volume of the block copolymer V_P. The block copolymer is dissolved in a solvent mixture of solvents α and β with initial volumes $V^0{}_\alpha$ and $V^0{}_\beta$. The block copolymer composition is chosen such that $f_A<f_B$ in order to favor the formation of cylindrical domains of A in a continuous matrix of B in the bulk. The solvent mixture is chosen such that at the beginning of the casting process it is a neutral solvent for both blocks. Solvent β should have a higher evaporation rate and should be more selective for the B-block compared to solvent α.

For the following calculations, we set the initial volumes of the three components polymer, $V^0{}_P$, solvent α, $V^0{}_\alpha$, and solvent β, $V^0{}_\beta$, in the cast solution. With a given volume fraction of the A-block in the block copolymer, f_A, the initial volumes of the two polymer blocks are then $V^0{}_A=f_A V^0{}_P$ and $V^0{}_B=(1-f_A)V^0{}_P$.

Solvent Evaporation Kinetics.

After casting the solution onto a solid support the two solvents will evaporate, each with its specific evaporation rate. Langmuir[113] calculated the rate of evaporation of a liquid per unit area as

$$\frac{\dot{m}}{A} = (p^0 - p_{air})\lambda \tag{4.1}$$

where m is mass of evaporated liquid, A is the surface area of the liquid, p^0 is the vapor pressure of the pure liquid, p_{air} is the vapor pressure of the liquid above the cast membrane during the experiment, and λ is an inverse mobility characterizing the transport rate of liquid molecules from the membrane interior to the surface. Langmuir originally used an expression

derived from kinetic gas theory with $\lambda = \frac{M}{2\pi RT}^{1/2}$, where *M* is the molar mass of the liquid, and *RT* the thermal energy. Since the transport process in our case is limited by the diffusional transport of solvent within the membrane, which cannot be described by kinetic gas theory, we keep the more general form and use λ to characterize the transport rate of the solvent in the cast membrane.

According to Raoult's law for an ideal liquid mixture, the vapor pressure of each liquid component *J* will be proportional to its volume fraction ϕ_J in the mixture, i.e., $p_J = \phi_J p_J^0$. This volume fraction is given by $\phi_J = V_J/V$, where V is the total volume of the polymer/solvent mixture. The mass m_J relates to the corresponding volume of the liquid via $V_J = m_J/\rho_J$, where ρ_J is the density of the liquid. For simplicity, we consider the limit $p_{air} = 0$ (ideal venting conditions) which could be changed to arbitrary values in the numerical calculations, if desired. We then obtain the following set of coupled differential equations for the volume changes of the solvents

$$\frac{dV_\alpha(t)}{dt} = \Gamma_\alpha \frac{V_\alpha(t)}{V(t)} \tag{4.2}$$

$$\frac{dV_\beta(t)}{dt} = \Gamma_\beta \frac{V_\beta(t)}{V(t)} \tag{4.3}$$

where $V(t) = V_\alpha(t) + V_\beta(t) + V_P^0$ and $\Gamma_J = \frac{p_J^0 A \lambda_J}{\rho_J}$ is the evaporation rate of the pure solvent *J*. The equations can be numerically integrated assuming initial volumes V_J^0 and evaporation rates Γ_J. The evaporation rates may, in principle, be themselves a function of composition due to nonidealities caused by enthalpic and hydrodynamic interactions which affect the value of λ_J. These interactions are not further taken into account because it would not be expected to give significant improvement of the description in light of the assumptions that have already been made.

To be specific, we consider the block copolymer poly(styrene-*b*-2-vinylpyridine) (PS-P2VP) dissolved in a THF/DMF mixture. According to the nomenclature introduced above, we have the correspondence A=P2VP, B=PS, $\alpha = DMF$, and $\beta = THF$. Measured evaporation rates are $\Gamma_{DMF} = 0.01 \mu l/s$ for pure DMF and $\Gamma_{THF} = 6.74 \mu l/s$ for pure THF. The ratio of measured evaporation rates $\Gamma_{DMF} : \Gamma_{THF} = 1 : 67$ is in the same order of magnitude as the ratio of the corresponding vapor pressures $p^0_{DMF} : p^0_{THF} = 1 : 40$ (see Supporting Information) as expected from eq. (2) and the expression for Γ_J. Figure. 4.1 shows the calculated volume fractions of solvent α solvent β and polymer upon evaporation. Characteristic for

the evaporation of such solvent mixtures is an intermediate increase of the evaporation rate of lower boiling liquid (DMF) due to the strongly increasing volume fraction. Sets of volume fractions $[\phi_P(t), \phi_\alpha(t), \phi_\beta(t)]$ during evaporation for different initial compositions can then be mapped into a ternary phase diagram.

We would like to point out that the volume fractions $\phi_J(t)$ have been calculated based on the assumptions that (1) we only consider compositions within the top layer of the cast film and (2) consider composition-independent diffusivities. The presence of the subjacent layers, which have different and vertically changing compositions compared to the top layer, and their possible effect on the diffusivities may in practice retard the temporal evolution on the trajectory, such that the volume fractions $\phi_J(t)$ represent an upper limit. In this sense the calculated trajectories are representing the fast limiting case of ideal solvent vapor venting and non retarded solvent diffusion from subjacent film regions, serving as a guideline for the actual membrane preparation process.

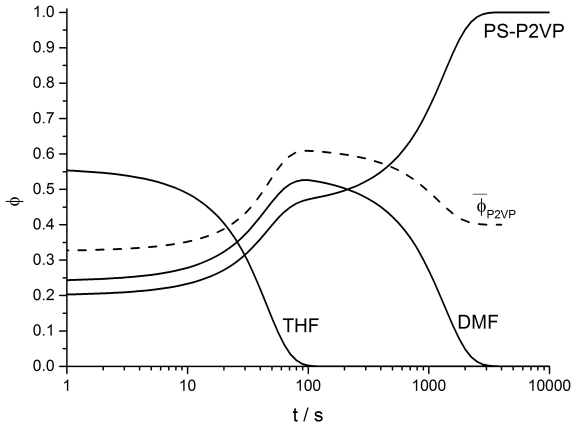

Figure 4.1. Volume fractions of THF, DMF, and PS-P2VP (solid lines) as well as solvent-swollen P2VP phase (dashed line) as a function of time, calculated with eq. (2) for swelling coefficients of the polymer blocks in the respective pure solvents $S_{P2VP}^{DMF} = 6$, $S_{P2VP}^{THF} = 3$, $S_{PS}^{DMF} = 1$, and $S_{PS}^{THF} = 8$, evaporation rates of $\Gamma_{DMF} = 0.01\mu l/s$ for DMF and $\Gamma_{THF} = 6.74\mu l/s$ for THF, and a P2VP-block copolymer volume fraction of 0.4.

Polymer Block Swelling.

Before evaporation we have a volume $V_A^0 = f_A V_P^0$ of dry polymer block A, a volume $V_B^0 = (1 - f_A)V_P^0$ of dry polymer block B, a volume V_α^0 of solvent α, and a volume V_β^0 of solvent β, which add up to a total volume $V = V_A^0 + V_B^0 + V_\alpha^0 + V_\beta^0$ in the casting solution. Upon swelling with solvent, the volume of a dry polymer block V_J^0 increases to

$$\widetilde{V}_J = V_J^0(1 + S) \tag{4.4}$$

where S is the swelling coefficient describing the relative amount of solvent that is taken up by the polymer upon swelling. Depending on the solvent quality of the solvent mixture, the A-block and B-blocks will swell to different extents. This can be characterized by different swelling coefficients S_A and S_B.

In the solvent mixture at a given time t of evaporation, each block will swell in relation to the current solvent composition if there is no preferential solvation. The swelling coefficient for a polymer block would then be intermediate between the swelling coefficients of the pure solvents, which can in a linear approximation be written as

$$S_A(t) = f_\alpha(t)S_A^\alpha + (1 - f_\alpha(t))S_A^\beta \tag{4.5}$$

$$S_B(t) = f_\alpha(t)S_B^\alpha + (1 - f_\alpha(t))S_B^\beta \tag{4.6}$$

$$f_\alpha(t) = \frac{V_\alpha(t)}{V_\alpha(t) + V_\beta(t)} \tag{4.7}$$

S_A^α, S_A^β, S_B^α and S_B^β are the swelling coefficients of the polymer blocks in the respective pure solvents.

In case of a dilute solution, where the available volume of solvent is larger than the volume taken up by swelling the polymer blocks, we have for the volume fraction of the solvent swollen polymer block A in the solution

$$\widetilde{f}_A(t) = \frac{\widetilde{V}_\alpha(t)}{V_{ges}(t)} = \frac{V_A^0(1 + S_A(t))}{V_\alpha(t) + V_\beta(t) + V_P^0} \tag{4.8}$$

If the volume of available solvent is completely taken-up by the solvent-swollen polymer blocks (semidilute solution), i.e., $V_{ges} = \widetilde{V}_\alpha(t) + \widetilde{V}_\beta(t)$, we have

$$V(t) = \widetilde{V}_\alpha(t) + \widetilde{V}_\beta(t) = V_A^0(1 + xS_A(t)) + V_B^0(1 + xS_B(t)) \tag{4.9}$$

where the factor *x* serves to adjust the swelling ratio calculated from eq. (5) to completely fill the remaining available volume with swollen polymer. From eq. (6) we calculate *x* to be

$$x = \frac{V_\alpha(t) + V_\beta(t)}{V_A^0 S_A(t) + V_B^0 S_B(t)} \tag{4.10}$$

Then the volume fraction of the solvent swollen polymer block A in the solution is finally given by

$$\widetilde{f}_A(t) = \frac{\widetilde{V}_\alpha(t)}{\widetilde{V}_\alpha(t) + \widetilde{V}_\beta(t)} = \frac{V_A^0(1 + xS_A(t))}{V_A^0(t)(1 + xS_A(t)) + V_B^0(t)(1 + xS_B(t))} \tag{4.11}$$

The morphological changes upon movement on the phase-trajectories in the ternary phase diagram will be largely determined by the volume fraction of domains of solvent-swollen polymer block A, $\widetilde{f}_A(t)$ and solvent-swollen polymer block B, $\widetilde{f}_B(t) = 1 - \widetilde{f}_A(t)$.
The swelling ratio may be calculated from the intrinsic viscosity $[\eta] = kM^\alpha$ as

$$S = \frac{2[\eta]\rho}{5} - 1 \tag{4.12}$$

with the Mark-Houwink constants *k* and α, which for various polymer/solvent systems are compiled in ref[114]. For the limit of a collapsed chain we obtain $S = 0$. As representative values for numerical calculations for the polystyrene/polyvinylpyridine system in DMF/THF or similar solvent mixtures we used S(PS/THF)=8, S(PS/DMF)=1, S(PVP/THF)=3,
and S(PVP/DMF)=6.

Ternary Phase Diagrams.
The ternary phase diagram in Figure 4.2 shows calculated composition trajectories at different evaporation times for different initial solvent compositions $f_{DMF} = 0, 0.2, ...1.0$ starting at a polymer volume fraction of $\phi_P = 0.15$. Since initially mostly THF is evaporating, the trajectories typically first follow a nearly straight line of constant DMF:polymer ratio until for near zero THF-content they merge into a line corresponding to the binary polymer/DMF mixture diagram toward the pure polymer. In Figure 4.2a, the trajectories are mapped into a ternary phase di-

agram indicating the solvent-swollen volume fraction $\widetilde{f}_{P2VP}(t)$. Interesting for the membrane formation process is the region of high solvent-swollen volume fraction $\widetilde{f}_{P2VP}(t)$ in the middle left of phase diagram, where transitions from spherical to cylindrical or lamellar structures are expected to occur. These intermediate high values of $\widetilde{f}_{P2VP}(t)$ can also be observed in Figure 4.1. In Figure 4.2b the trajectories are mapped into a phase diagram indicating the total volume fraction of polymer. The red region indicates the semidilute concentration regime, where polymer/polymer interactions become increasingly important.

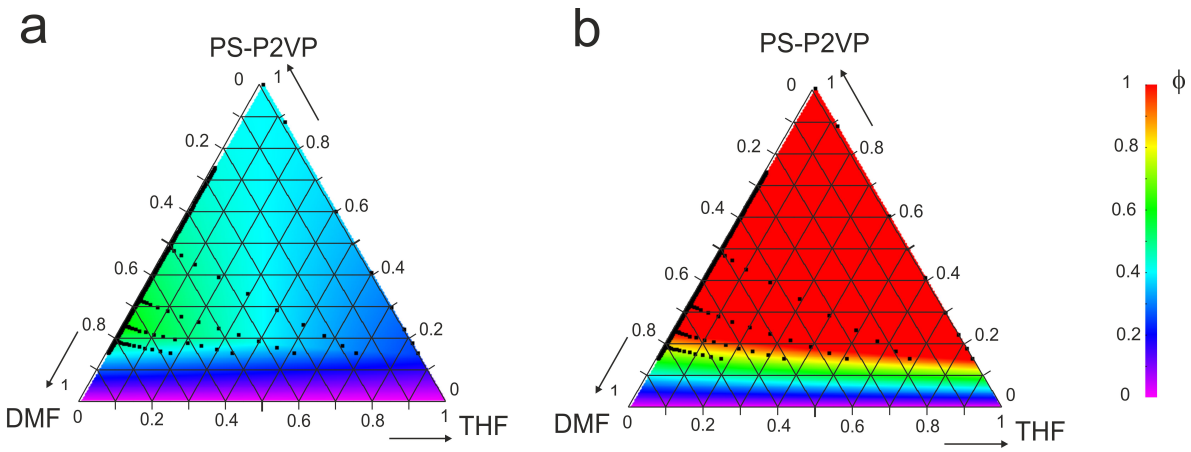

Figure 4.2. Calculated composition trajectories (dotted lines) mapped into ternary phase diagrams displaying (A) the solvent-swollen P2VP volume fraction $\widetilde{f}_{P2VP}(t)$, and (B) and total volume fraction of block copolymer (B) for PS-P2VP in THF/DMF. In the left region of the phase diagram the $\widetilde{f}_{P2VP}(t)$-values are high, in a range where sphere-cylinder transition can occur. The calculations were done using eq. 4.3 and the same set of parameters used in Figure 4.1. As starting compositions for the trajectories, corresponding to their first data point ($t = 0$), we choose a polymer volume fraction of $\phi_P = 0.15$ and solvent compositions $f_{DMF} = 0, 0.2, 0.4, 0.6, and 0.8$ which are typical conditions for the membrane preparation process.

Topological Investigations of Trapped Membranes

In the following sections we (A) describe the characteristic membrane morphologies that we observed by AFM and SEM and map them into a ternary phase diagram, (B) describe characteristic transition structures between these morphologies, (C) describe the topological path to ordered membrane pores consistent with the observed morphologies in the phase diagram, and (D) describe and discuss *in situ* synchrotron SAXS experiments that further support the proposed mechanism of pore formation. Throughout the parts B-D we discuss our findings in

relation to all presently available literature, which serves to obtain a consistent and complete picture of membrane structure formation.

A) Stability Regions of Characteristic Morphologies.

To follow the structural evolution experimentally, we immersed the cast films in water after a certain evaporation time, which reproduces the actual membrane formation process. The structures of the top layers of the cast films were then characterized by AFM and SEM. Typical top layer topologies that were observed by this procedure are sphere percolation networks (SN), spinodal networks (SpN), ordered pore networks (PN), and cylinders (DC). AFM images of these structures are shown in Figure 4.3.

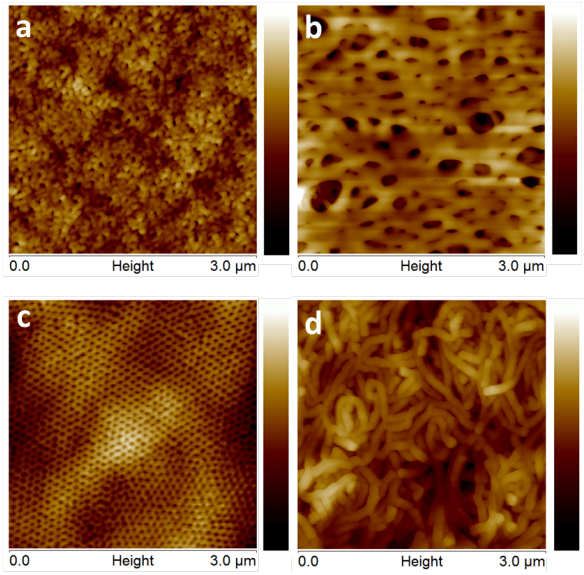

Figure 4.3. AFM images of four characteristic morphologies found for the block copolymer S2VP-1: sphere percolation network (SN), spinodal network (SpN), ordered pore network (PN), and disordered cylinders (DC).

In Figure 4.4 these structures and variations of them, observed in membranes immersed and trapped in water after certain evaporation times, are mapped into a ternary phase diagram at compositions in line with the calculated trajectories from Figure 4.2. The characteristic stability regions in this "phase diagram" do not correspond to equilibrium structures but represent regions of characteristic structures that have been formed at the corresponding ternary polymer/solvent compositions. The experiments were performed with initial polymer volume fraction of $\phi_P = 0.15$ and solvent compositions $f_{DMF} = 0, 0.3, 0.5, 0.7, and 1.0$.

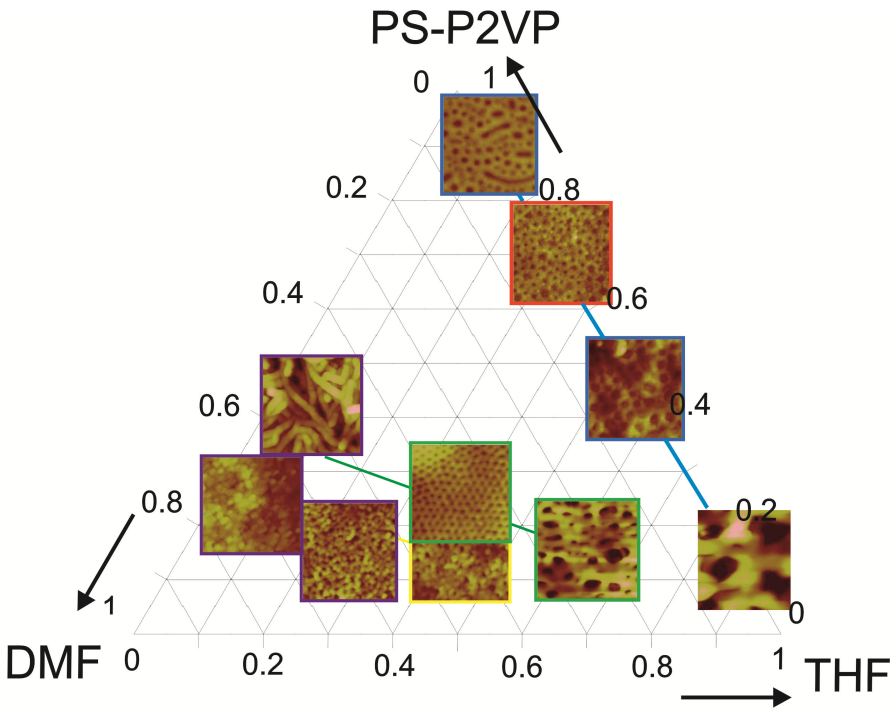

Figure 4.4. AFM height images of the top layers of S2VP-1-membranes prepared by immersing cast solutions in water with varying initial solvent composition. Images with equally colored frames belong to the same trajectories: purple, 15 wt.% of polymer in DMF/THF 7/3; yellow, 15 wt.% of polymer in DMF/THF 5/5; green, 15 wt.% of polymer in DMF/THF 3/7; blue, 15 wt.% of polymer in THF; red, 20 wt.% of polymer in THF; orange, 10 wt.% polymer in THF. The images are mapped into the ternary phase diagram according to the calculated composition trajectories in Figure 4.2. A more detailed version of the phase diagram and enlarged AFM images are reproduced in the Supporting Information.

With the distinction of different characteristic topologies as shown in Figure 4.3, we can identify characteristic stability regions in the phase diagram as shown in Figure 4.4. In the right half of the phase diagram, corresponding to the region of high THF content (> 50%), we typically observe disordered, spinodal-type continuous networks with polydisperse pores (SpN). The mean pore size decreases with decreasing THF content. In the lower left of the phase diagram corresponding to low polymer concentrations (< 20 %) and low THF content (< 50 %), we observe disordered sphere percolation networks (SN). With decreasing THF content the sphere diameters first decrease and then increase again. In the middle to upper left region of the phase diagram at high DMF volume fractions (> 80 %) and higher polymer volume fractions (> 30%), we observe disordered cylinders (DC). The most interesting region is located

in the middle of the phase diagram around a THF content of 50 % and a polymer content of 25 % where the desired ordered continuous network with monodisperse pore sizes is formed (PN). Between the ordered continuous network and the disordered cylinders (DC), a region of ordered cylinders (OC) is observed.

In Figure 4.5 we have mapped the stability regions of the characteristic topologies by tentatively drawing lines that separate adjacent regions. Further, a horizontal line is drawn in the lower region of the phase diagram which separates the region of dilute solution, where polymer/solvent interactions dominate, from the semidilute solution, where polymer/polymer interactions become increasingly important. Further, a vertical line at a THF content of 55-60% separates the region of weak segregation (WSL) at high THF content, where the block copolymers are dissolved in a common solvent, from the region of strong segregation (SSL) at high DMF content, where the block copolymers are dissolved in selective solvent for the P2VP-block. This facilitates the following discussion of thermodynamic and kinetic aspects of the structure formation mechanisms.

Spinodal Networks (SpN). A disordered, bicontinuous spinodal-type network structure is observed in the semidilute region under weak segregation conditions. In this region we have, particularly at high THF volume fractions, neutral solvent conditions; i.e., both polymer blocks are equally well solvated. Recently performed small-angle neutron scattering (SANS) experiments using contrast variation[115] show the absence of microphase segregation. With decreasing THF volume fraction the characteristic length scale λ_S of the spinodal network structures decreases. Figure 4.4 shows that along a horizontal line at lower polymer concentrations at high THF content (70%) the characteristic length scale is λ_S=200 nm, which decreases to λ_S=50 nm for very low THF contents. A decreasing THF-content decreases the solvent quality for the polymer blocks, in particular for PS-blocks. The bicontinuous spinodal structure (SpN) is characteristic for the support layer structure of the final membrane. Semidilute solution conditions provide continuous, mechanically stable polymer network structures upon immersion in water.

In the dilute regime isolated, highly swollen particles are observed. In Figure 4.4 this can be observed in the $f_{THF} = 1.0$ evaporation series, where below $\phi_P < 0.2$ (dilute regime), we observe large 200 nm particles, whereas above $\phi_P > 0.2$ (semidilute regime), we observe bicontinuous network structures. In pure THF at high polymer concentrations the structure evolves into a continuous swollen polymer network with isolated polydisperse spherical pores.

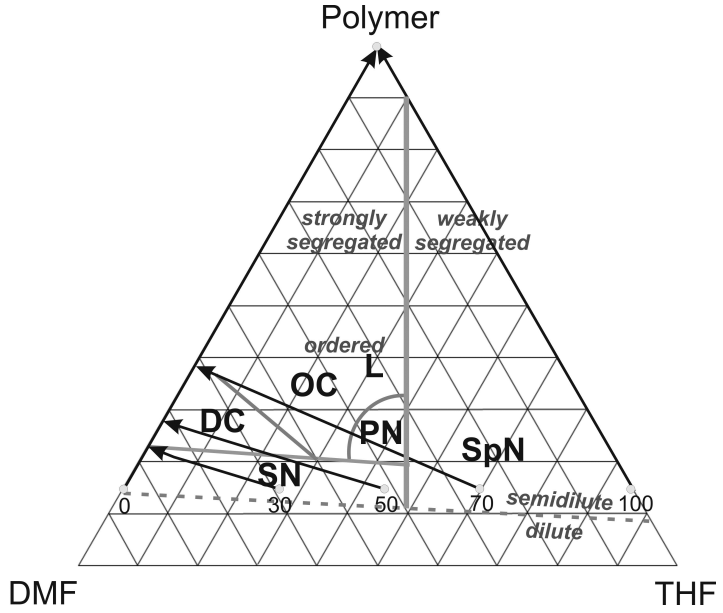

Figure 4.5. Schematic ternary morphology diagram showing the stability regions of the characteristic morphologies observed in the experiments: SN = percolation network, SpN = spinodal network, PN = pore network, DC = disordered cylinders, OC = ordered cylinders. L indicates lamellar structures. Also indicated are lines separating the dilute/semidilute regions and the weakly segregated/strongly segregated regions, together with the trajectories corresponding to Figure 4.4. The numbers indicate the relative amount of THF in the solvent mixture before evaporation occurs.

No ordering is observed due to the weak segregation up to highest polymer volume fractions.

Sphere Percolation Network (SN). A percolated sphere network structure is observed in the semidilute region at higher DMF volume fractions, i.e. stronger segregation. In this region the block copolymer microphase separates to form spherical micelles which, when immersed in water, are trapped and aggregate into a percolation network. The length scales are smaller compared to the spinodal network structure, since they reflect the length scale of the segregated polymer blocks d* in the micelles. With decreasing THF content the sphere diameters first decrease because the PS-blocks become less solvated and then increase due to the increased solvation of the P2PV-blocks.

Disordered Cylinders (DC). With increasing polymer volume fractions above the stability region of the spherical micelles, and at high DMF volume fractions, there is the stability region of the cylindrical micelles. In this region the P2VP-blocks are well solvated and highly swollen, leading to a high P2VP volume fraction $\widetilde{\phi}_{P2VP}$ which is known to trigger a sphere-cylinder

transition. Careful inspection of the AFM images shows that in the transition regime between spheres and cylinders pearl-necklace-type elongated structures of linearly aggregated spherical micelles are formed (see Figure 4.4), which represent the corresponding transition structures.

Ordered Cylinders (OC). There is a region of ordered cylinders next to the disordered cylinder region at higher THF content, where the PS chains are better solvated. When the P2VP- and PS-blocks are well solvated, the mutual interactions are sufficiently high to induce a disorder-order transition. The stability region of ordered structures is indicated in the ternary phase diagram in Figure 4.5.

Pore Network (PN). For the formation of isoporous membranes, the most important region is in the center of the ternary phase diagram, where ordered network structures with uniform-sized pores are formed. This zone is located between the SN-, SpN-, and OC-stability regions. It is topologically very similar to the spinodal network structure in the adjacent SpN-region. The pore network structure may be viewed as a topology where the length scales of spinodal decomposition λ_S (macrophase separation) meets the intrinsic length scale of the block copolymers d^* (microphase separation). It has been theoretically shown[116] that ordered periodic structures can be formed and become stable upon spinodal decomposition, if the characteristic length of the spinodal decomposition λ_S becomes equal to an intrinsic length scale of the system, which in our case would correspond to the length scale d* of the block copolymer. This would provide stabilization of the pore structure. In the membrane formation process, the structure of the desired top layer corresponds to this regular ordered pore structure. A one-step route employing a similarly concerted process of spinodal macrophase separation and block copolymer microphase separation has recently been worked out to prepare well-defined meso-/microporous block copolymer structures.[117]

B) Transitions Structures.

Indications that the topologies shown in the ternary phase diagram are characteristic and their designated regions are adequately delineated are trapped transition structures. The example of the pearl-necklace structure of linearly aggregated spheres, which is observed between the sphere percolation network (SN) and the disordered cylinders (DC), has already been described above (Figure 4.4). Linearly aggregated spheres and sphere percolation networks have very recently been observed as well by using cryo-SEM of freeze-fractured lyotropic solution structures.[102] The phase sequence SN-DC on the DMF-rich side of the phase di-

agram has been observed by cryo-electron microscopy.[118] In agreement with our findings, they reported at lower polymer concentrations a sphere percolation network (SN), at higher polymer concentrations spheres that aggregated into a cylinder network, and finally elongated separated cylindrical micelles (DC) above 20% polymer content.

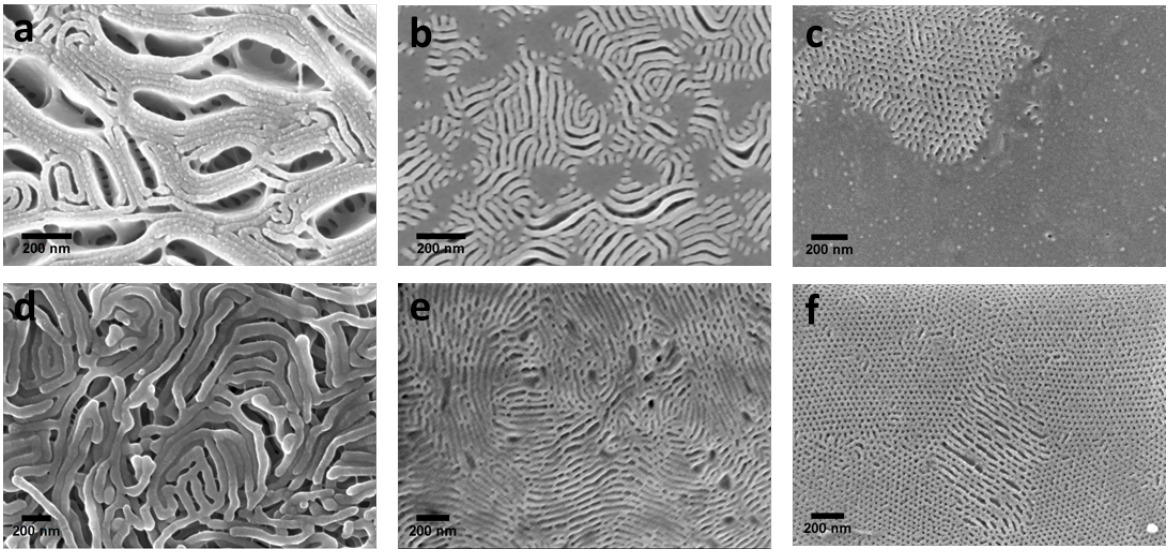

Figure 4.6. Top layer SEM images of typical transition states found on S2VP-2 films (a,b,c,e,f) and S2VP-3 films (d): (a) ordered cylinder stacks close to the OC/L transition region, (b) elongated cylindrical pores and closed layers in the OC/L transition region, (c) ordered pores and closed layers in the PN/L transition region, (d) isolated cylinders in the DC/OC transition region, (e) ordered cylinders with pores in the OC regime close to the PN region, and (f) ordered spherical pore network with occasional elongated pores connected by struts in the PN/OC transition region.

Using scanning electron microscopy (SEM), we could identify many more transition structures, which are summarized in Figure 4.6. The transition of the ordered pore network (PN) into a cylinder network structure (OC) is shown in Figure 4.6f. Here, the ordered pore network matrix starts to disconnect into thin parallel cylinders that are connected by thin struts. This structure is dominant in Fig. 4.6e. The formation of the ordered cylinder morphology is induced by a decreasing THF content. This decreases the solvation of the PS-blocks, such that the PS matrix volume fraction falls below the limit to form a stable continuous matrix around the pores. With further decreasing THF content the cylinders become more separated and less ordered (Figure 4.6d), indicating the structural transition into the disordered cylinder region (DC).
For higher polymer content we observe transition structures into a lamellar phase (L). Figure

4.6c shows a top layer with an ordered pore network (PN) together with a closed continuous nonporous surface layer. Figure 4.6b presents a transition structure between the ordered cylinder region (OC) and a continuous top layer (L). The same type of structure has very recently been observed by AFM close to the lamellar phase for another block copolymer system.[119] Finally, Figure 4.6a shows adjacent cylinders connected by thin cylindrical struts, which corresponds to transition structure trapped between the ordered cylinder region (OC) and the lamellar region (L).

The transition from large length scale λ_S spinodal network (SpN) at high THF content to the ordered pore network (PN) can be observed from a cross-sectional cut of a membrane as shown in Figure 6.3. The sequence of structures from the bottom to the top of the membrane corresponds exactly to the trajectory drawn in the ternary phase diagram in Figure 4.4. The ordered pore top layer network is clearly seen in Figure 6.3a. The cross-sectional cut shows the underlying spinodal network structure with cross-linked cylindrical strut structures. As solvent can only evaporate from the top surface of the polymer cast film, there will be a polymer and solvent concentration gradient vertically across the membrane, very similar to the trajectories investigated in our evaporation studies.

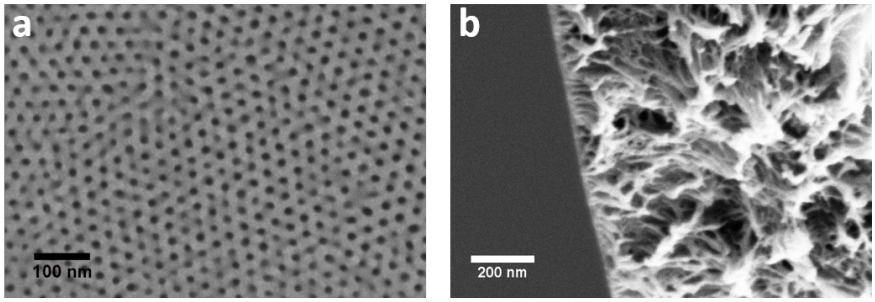

Figure 4.7. SEM image of the (a) surface and of a (b) cross section of an integral asymmetric membrane of the block copolymer S2VP-2. The top layer of the membrane consisting of a regular array of uniform size pores in a continuous matrix is shown in (a). The SEM cross-section image shows the bicontinuous network support matrix. The characteristic length scale of the network decreases continuously from the lower support to the top layer. The structure reflects the trajectory through the phase diagram shown in Figure 4.5.

On the basis of the observed characteristic morphologies (Figure. 4.3) and their transition structures (Figures 4.6 and 6.3) it is possible to illustrate their topological relations as shown

in Figure 4.8. The sequence of structures is drawn in correspondence to their position in the central part of the phase diagram in Figure 4.5. This schematic overview can serve to identify and readjust the compositional trajectory taken by a particular membrane preparation process.

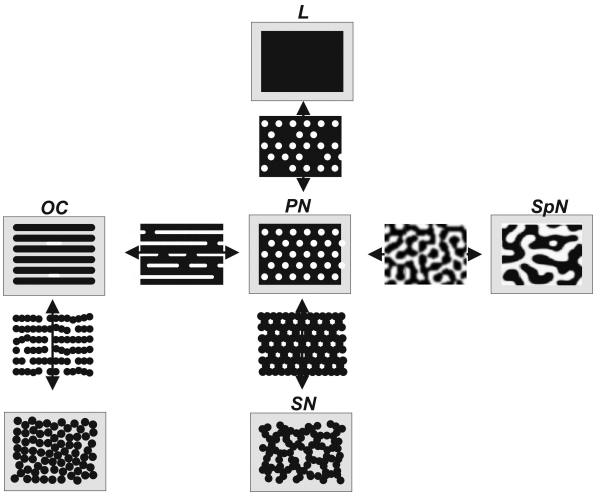

Figure 4.8. Schematic overview of the relevant topologies in the formation of porous membranes. Many of the structures are transients that are trapped during phase separation. This array of structures is compatible with the available literature.

These structures have been reported in many publications dealing with the block copolymer membrane formation process either using PS-P2VP or PS-P4VP in mixed solvent systems of DMF, THF, or dioxane. The porous fused sphere percolation network (SN) was observed in refs.[27] and[28] close to the ordered pore phase (PN) as reported in ref[101]. A structurally very similar dense network of spheres in solution was observed by cryo-SEM[102,120] as were densely packed spheres, corresponding to sphere percolation networks in the lower left of the ternary phase diagram.

Parallel oriented ordered, nonconnected cylinders (OC) and isolated, highly swollen cylindrical micelles (DC) have been reported in ref[120]. Parallel aligned swollen cylinders with strut connections (transition from OC to PN) were observed in ref[101]. A similar transition structure involving regular pores with elongated pores and struts was reported in ref[28].

The perfect ordered pore network (PN) has been reported many times.[27,101,102,106,29,107,28,120–123] Ordered and more disordered pore networks exhibiting typical transition structures such as struts of aggregated spherical micelles (SN) have been observed by AFM in ref[122]. Transition structures from the pore network (PN) into the spinodal network (SpN) such as thin pores with

spinodal network dense support layers have been reported in ref[123]. SEM-cross-sections with a thin porous top-layer and a spinodal layer below with increasing pore size were observed in ref[28], and a smooth spinodal network structure in ref[29]. The appearance of cylinders in the pore network along the trajectory for longer evaporation times has also been observed in ref[29]. Disordered pores with uniform pore size have been reported in[107] and[28].

The disappearance of pores to form smooth, closed top layers as an indication of a structural transition from the pore network (PN) into the lamellar phase (L) has also been observed. The fusion of a few pores has been reported in refs[27] and[29] and also in ref[120], where ca. 1/3 of the pores had fused into a closed continuous lamellar structure. Similar observations have been made in ref[123] where ca. 1/2 of the pores were fused, in ref[29] with ca. 2/3 of fused pores and in ref[107] where nearly all pores were fused. An ordered pore network containing both closed lamellar regions (transition to L) as well as cylindrical pore/cylindrical strut structures (transition to OC) have been reported in ref[120], strut-connected lamellae in ref[122], and small closed-pore lamellar regions in ref[120] together with extended closed lamellar regions at higher polymer concentrations, i.e., for trajectories starting at higher polymer concentration and THF-content as in refs[121] and[122].

C) Topological Path to Ordered Pore Structures.

Of central interest for the membrane formation process is the exact topological path that connects the percolated micellar network (SN) or spinodal network (SpN) to the ordered pore network (PN). SANS- and cryo-TEM studies[118] agree that micelles in the THF/DMF mixtures consist of a core containing the PVP-blocks and a shell containing the solvent-swollen PS-blocks. According to ref[118], using cryo-TEM and SANS with contrast variation, even in pure DMF in dilute solution, PVP forms the core and PS the shell. Only if water is added to strongly reduce the solubility of PS, the PS-blocks will form the micellar core. This is also in line with our observation that upon swelling of the PVP-cores with DMF a transition into cylindrical micelles (DC) is observed.

An alternative topological path has been proposed in ref[26] based on the assumption that micelles are formed with micellar cores consisting of the PS-blocks and shells consisting of the PVP-blocks. This micellar topology then requires a microphase inversion, where the PS-cores become the continuous matrix, and the PVP-shells form the pores of the ordered pore network (PN). For this the authors proposed a topological path via a honeycomb array of

micelles, where the centers of the honeycomb hexagons become the location of the pores. Indeed, AFM images show networks of micellar pearl-necklace strings, topologically similar to the honeycomb model, but also similar to the micellar pearl-necklace strings shown in Figure 4.4, corresponding to the SN/PN/DC transition region. Thus, their observations are well in accord with the proposed topological relations shown in Figure 4.8. Very recent studies by the same group using cryo-SEM on a PS-P4VP system forming micellar pearl-necklace strings in solution provided direct evidence of the topological path from cylindrical micellar structures evolving into the surface pore structure (PN).[102]

On the basis of our experimental results, and in line with the results and interpretations outlined in ref[118], we schematically illustrate the topological path into ordered pore network (PN) in Figure 4.9. Upon THF evaporation on a composition trajectory entering the microphase segregated regime and being at sufficiently high polymer concentrations where polymer-polymer interactions are sufficiently strong to induce order, the solvent-swollen PS-blocks in the overlapping micellar shells form a dense, stable continuous matrix with embedded ordered spherical solvent-swollen PVP-cores. It is this structure that has to be trapped by immersion in water, leading to a mechanically stable PS-matrix with ordered solvent-swollen PVP-core domains, which eventually upon drying collapse onto the PS-matrix to form an open pore system. If immersed in water at later times, further advancing on the trajectory to lower THF content, transitions into cylindrical or lamellar topologies take place as shown in Figure 4.6. If the trajectory proceeds at too low polymer volume fractions, polydisperse pore systems resulting from the sphere percolation network (SN) or spinodal networks (SpN) result.

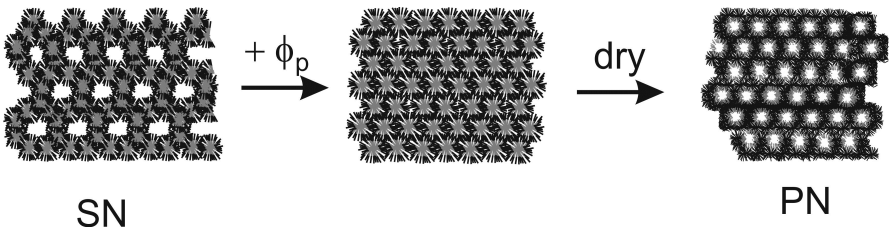

Figure 4.9. Topological path from a sphere percolation network (SN) to an ordered sphere array by increasing polymer volume fraction to an ordered pore network (PN) upon drying of the solvent-swollen core domains.

Since the ordered pore network is close to the cylindrical region, and because there is a vertical composition gradient in the membrane during evaporation, spherical and vertically elon-

gated pores are often found.[22,27] Long vertical cylindrical pores, which have been reported for polymer films produced by other methods,[24,124] are never found. The vertical dimension of the pores is limited by the small stability region of the pore network (PN) on the composition trajectory. A prolonged evaporation time would not result in longer vertical pore dimensions, but rather the formation of cylindrical strut structures on the top layer (see Figure 4.6e,f) upon transition into the ordered cylinder phase (OC). In all successful cases, a sponge-like spinodal structure (SN or SpN) is formed underneath the top layer. The synergy of this process for the formation of isoporous integral asymmetric membranes, which need a thick large-pore support structure and a thin nanoporous top layer for high mechanical stability and high flow rates, is fortunate and remarkable.

D) *In Situ* Investigation of Structural Evolution.

The conclusions drawn so far are based on postpreparative analytical tools such as AFM and SEM performed on membranes prepared under systematically varying conditions. We therefore developed a method to study the structural evolution during the membrane formation *in situ* by using synchrotron small-angle X-ray scattering (SAXS). For this study films, doctor-bladed from block copolymer solutions with different polymer concentrations and solvent compositions onto a continuous X-ray transparent polymer support tape, were rapidly translated into the X-ray beam to probe the structural changes upon evaporation of the solvent *in situ*. Using fast detectors this allowed one to follow the structural evolution during the membrane formation process with 10 s temporal resolution.

Figure 4.10 shows the typical evolution of scattering patterns observed upon evaporation of solvent. In the first measurement after 15 s of evaporation, a weak featureless small-angle scattering pattern characteristic for an unstructured polymer solution is observed. After 30 s a weak Debye-Scherrer ring appears, indicated by the arrow in Figure 4.10. It signals the beginning microphase separation of the block copolymers solution. After 45 s, the Debye-Scherrer ring has clearly developed. From the AFM and SEM studies it is clear that after 20-30 s the composition trajectory enters the segregated regime with the ordered pore structure (PN) at 70% initial THF content or the micellar percolation network (SN) at lower THF content. This observation is in line with recent SAXS experiments which showed that asymmetric membranes fabricated from casting solutions with polymer concentration at or slightly below the ordering transition possess the desired nanopore structure (PN).[101]

We observe the intensity of the Debye-Scherrer rings to increases and their position to shift continuously to lower q-values, indicating an increase of the characteristic length scale d*. Measurements at subsequent times show the appearance of a strong featureless small-angle background scattering indicating macrophase separation. It eventually completely obscures the Debye-Scherrer ring. The observed strong increase of the small-angle scattering is consistent with the observation that initially the casting solution is a clear and homogeneous liquid, whereas at the end of the evaporation process the resulting polymer film appears white due to the formation of the large-scale heterophase spinodal network.

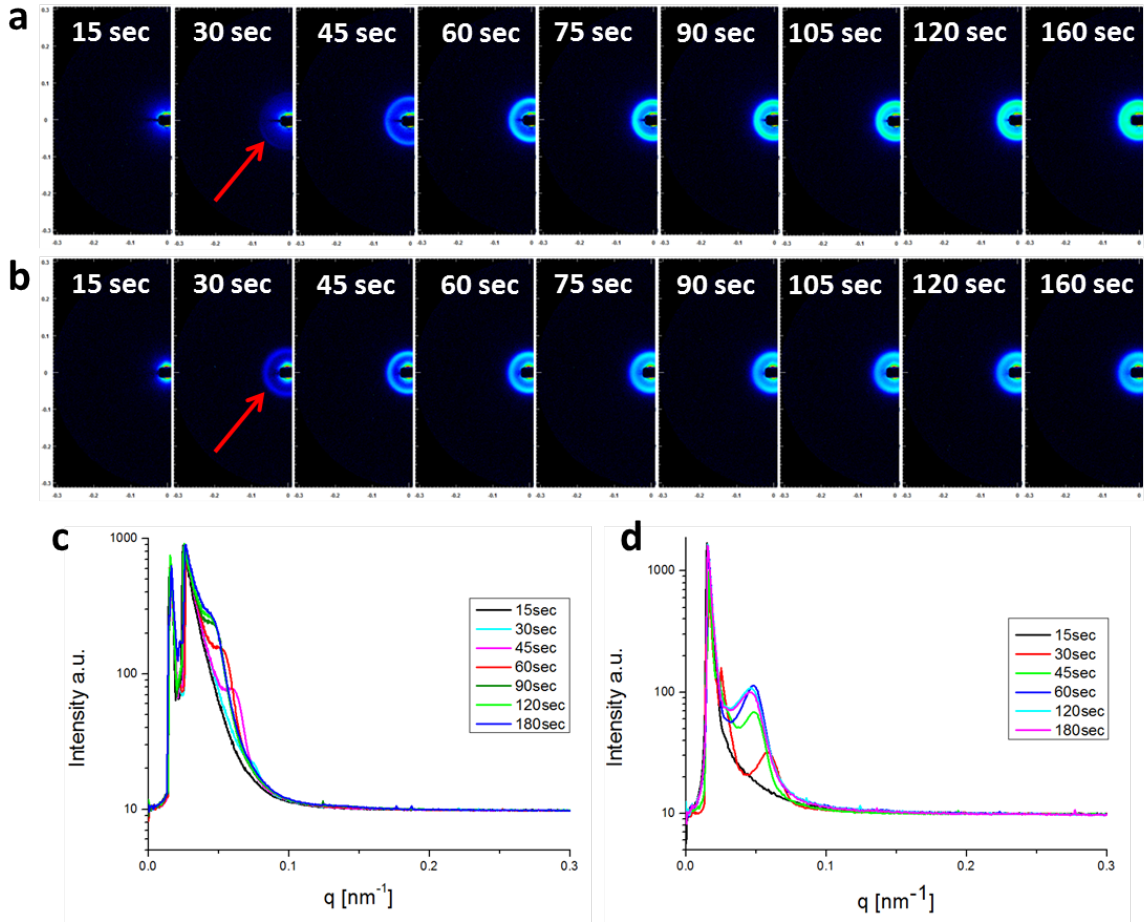

Figure 4.10. Synchrotron SAXS patterns of cast S2VP-1 polymer films in different solvent compositions measured during solvent evaporation and the corresponding scattering curves obtained by sectorial averaging. The solvent compositions are DMF/THF: (a,c) 70/30 and (b,d) 50/50. The scattering intensities correspond to the AFM-surface images on the purple and yellow trajectories in Figure 4.4.

The observed shift of the Debye-Scherrer ring to lower q-values corresponds to an increase of the characteristic length scale d*. This agrees with our AFM measurements along composition trajectories shown in Figure 4.4, where the size of the block copolymer micelles increases due to strong selective swelling of the micellar core-forming P2VP-block, which determines the characteristic length scale of the system. As observed in Figure 4.4, also highly swollen cylindrical micelles can be formed. These observations are in agreement with previously reported SAXS measurements,[121] where upon evaporation above 20 wt% polymer order became noticeable with the same trend of increasing d* with increasing evaporation, and also with very recent GISAXS and cryo-SEM investigation showing similar increase of the characteristic length scale upon evaporation and pore formation.[102] As shown in the Supporting Information for a PS-P4VP system, a late-stage ordered cylindrical phase with a horizontal alignment of the cylinders as in Figures. 4.4 and 4.6 can also be observed by our *in situ* SAXS experiments.

The measured scattering patterns in Figure 4.10 are isotropic and can be azimuthally averaged to obtain the scattering curves shown in Figure 4.10c and d. Here the emergence and the continuous shift of the diffraction peak to lower scattering vector q and the subsequent approach to a stationary value of the peak position can be well observed. The peak position q* can be related to the characteristic distance via $d* = 2\pi/q*$. In Figure 4.11 the length scales obtained from a series of evaporation experiments starting at different DMF/THF ratios are displayed.

Figure 4.11 shows the temporal evolution of the measured length scale d* of evaporating S2VP-1 films at different solvent compositions. The dead time of the experiment is 5 s set by the transport of the film from the doctor blading position to the beam position. Measurements are then taken in 10 s frames. The first datapoints in Figure 4.11 correspond to the first observation of a Debye-Scherrer ring in the measured scattering pattern, from whose position the length scale d* is calculated. We observe that except for pure THF, which follows a completely different trajectory in the ternary phase diagram as shown in Figures 4.4 and 4.5, all solvent mixtures show an increase of the characteristic length scale d* in the first 100 s of the evaporation experiments, then reaching a plateau value. The low THF content mixtures (< 50% THF) show the largest increase in length scale due to the large degree of micellar core swelling in these DMF-rich mixtures. The first peak appears when the polymer volume fraction reaches a certain threshold which is $\phi_P \approx 0.2$, similar to reports in ref[121]. Above

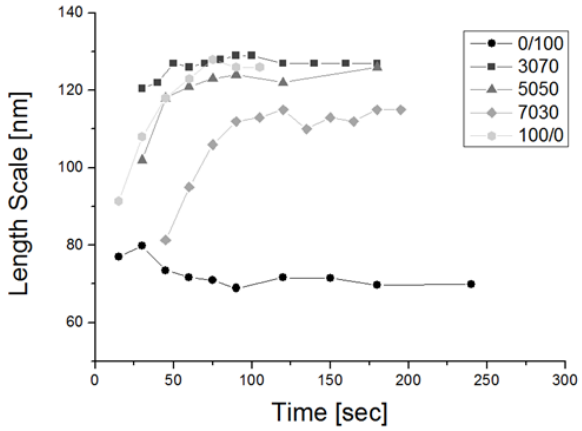

Figure 4.11. Evolution of the length scale d* of evaporating S2VP-1 films in different solvent compositions (DMF/THF): 0/100 (black circle), 30/70 (black box), 50/50 (gray triangles), 70/30 (gray diamond), 100/0 (gray circle). The dead time of the experiment is 5 s. For the membrane preparation process the initial phase during the first 60 s is most relevant.

this threshold polymer-polymer interactions can induce ordering. This occurs fastest for pure THF, and progressively slower for lower THF contents, because of the slower evaporation rate and corresponding slower change in composition on the phase trajectory.

The trajectories for pure DMF and the mixed solvent systems solution (f^0_{THF}=0.7, 0.5, 0.3, and 0) end in similar regions of the phase diagram with similar characteristic length scales and similar degrees of segregation. The trajectory for pure THF transects a completely different region of the phase diagram in the weakly segregated state and thus has low values ($d* = 80nm$) as the characteristic length scale. It slightly decreases upon evaporation as no selectivity of the solvent develops and the distance between the segregated domains slightly decreases.

As practical guidelines for the preparation of isoporous integral asymmetric membranes we may conclude that: (1) The starting polymer concentration, which determines the viscosity of the solution and thus controls solvent cast conditions to obtain a smooth viscous, stable film, should be in a range of $\phi^0_P = 15 - 25wt\%$. (2) For a given value of the starting polymer concentration, the solvent composition f^0_α, which sets the starting point for the evaporation trajectory in the triangular phase diagram, should be chosen such that the trajectory transects the PN-phase as the first ordered structure. (3) The evaporation time t^* needed to reach the PN-phase for subsequent immersion in water may be estimated with the help of eq. (4.2).

4.5 Conclusions:

Using AFM, SEM, and *in situ* synchrotron SAXS, we have for a typical block copolymer/mixed solvent system mapped out the transient morphological structures which are formed during fast solvent evaporation into a ternary phase diagram. We focused particular on the stability region of an ordered pore phase which is relevant for the generation of integral asymmetric isoporous membranes. We could identify characteristic morphologies, i.e., spinodal networks, sphere percolation networks, ordered pore structures, and disordered and ordered cylinders together with transient structures connecting their stability regions. With given evaporation rates for the pure solvents, we calculated the corresponding composition trajectories in the phase diagram to identify suitable experimental conditions in terms of initial polymer volume fraction ϕ_P^0 , solvent composition f_α^0, and immersion time t* to trap the desired pore structure.

Acknowledgments:
We thank the EU (Project #228652, *SELFMEM*), the German Science Foundation (SFB 840-TP B9, C.S.) and the Elite Network Bavaria (scholarship for P.R.) for financial support. We also thank M. Hund for help with the AFM-measurements.

The authors declare no competing financial interest.

4.6 Supporting Information

Volatility of the casting solvents

The vapor pressures at $20\,^{\circ}\mathrm{C}$ are given by $p^0_{THF} = 173 mbar$ and $p^0_{DMF} = 3.8 mbar$, i.e. THF has a 48-fold vapor pressure compared to DMF (see Table S1). Assuming a similar diffusivity of the two solvents (similar values of λ) we expect a similar ratio of 48:1 for the evaporation rates.

Evaporation rates were measured for the pure solvents. The data are displayed in Table S1.

Table S1. Measured loss of weight for the pure solvents THF and DMF starting from $70\mu L$ and $50\mu L$ respectively.

THF ($70\mu L$**)**		**DMF (**$50\mu L$**)**	
Time [sec]	Mass [mg]	Time [sec]	Mass [mg]
0	61.2	0	48
5	54.2	5	43
15	48.5	10	42.2
25	43	20	42
35	37	30	41.9
45	32	40	41.7
55	27	50	41.4
65	22	60	41.1
75	17	70	40.8
85	13	80	40.5
95	8	90	40.4
105	5	100	39.9
115	2	110	39.8
125	1	120	39.4
135	0	130	39
-	-	140	38.8
-	-	150	38.4
-	-	160	38.2
-	-	170	37.6
-	-	180	37.6

The experiments confirmed the expectations and rendered a ratio 43:1 relative to equal volumes ($10\mu L$).

Anisotropic PS-P4VP-scattering patterns

Kinetic studies using in-situ synchrotron SAXS were also performed with PS-*b*-P4VP diblock copolymers. Evidence of the ordered cylindrical phase (OC) mentioned in the trajectories described in Figures 4.4 and 4.5 was obtained at higher evaporation times where anisotropic scattering patterns were found after 70 seconds.

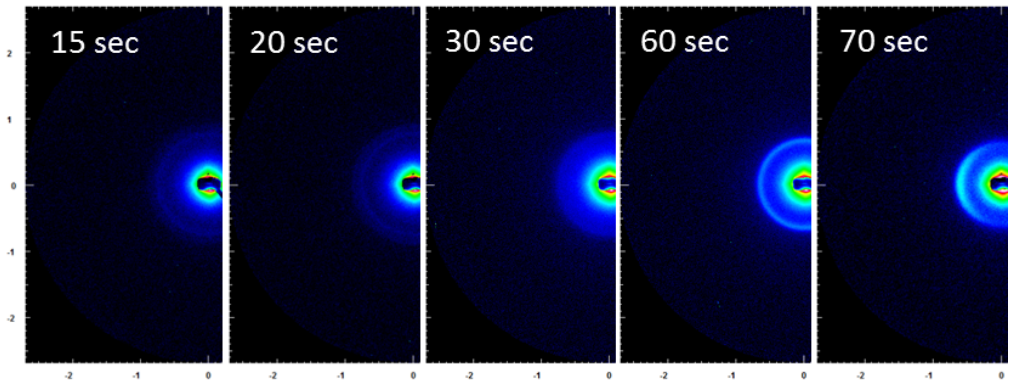

Figure S1. Evolution of scattering patterns of an evaporating PS-*b*-P4VP ($M_n = 100k$, $f(4VP) = 0.25$) solution in DMF/THF: 7/3. The anisotropic scattering pattern appears after 70 seconds.

Anisotropic patterns were found for PS-P4VP block copolymers likely due to the better solubility of P4VP in DMF which results in a different swelling behavior and a more stable OC-phase than found for PS-P2VP.

AFM images of the ternary phase diagram (see figure 4.4)

Series black: 15wt% SVP-1 in DMF

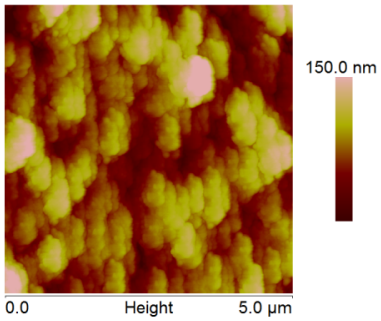

Figure S2. AFM height image of a polymer membrane cast from a solution of 15 wt% S2VP-1 in pure DMF after an evaporation time of 40 seconds.

Series purple: 15wt% SVP-1 in DMF/THF: 70/30

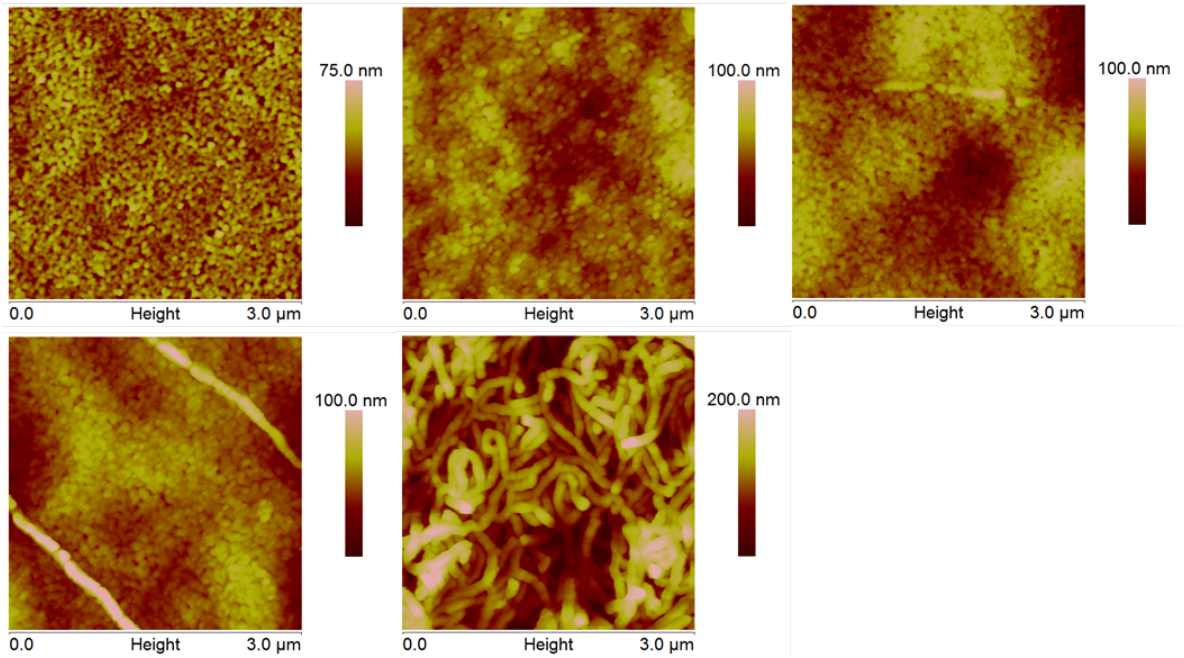

Figure S3. AFM height image of a polymer membranes cast from a solution of 15 wt% S2VP-1 in DMF/THF: 70/30. The evaporation times are 0 sec, 15 sec, 30 sec, 40 sec and 60 sec respectively.

Series yellow: 15wt% SVP-1 in DMF/THF: 50/50

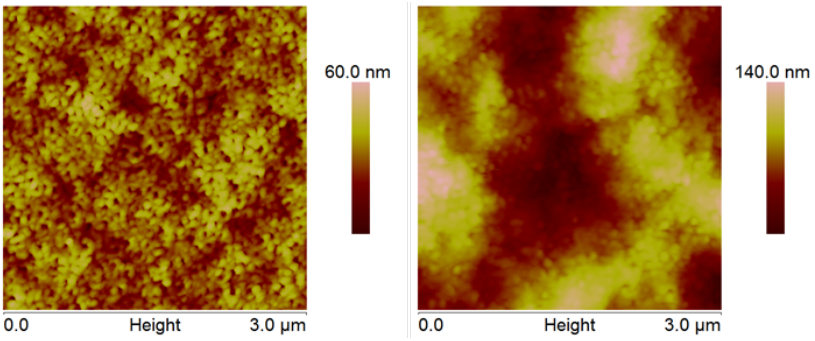

Figure S4. AFM height image of a polymer membranes cast from a solution of 15 wt% S2VP-1 in DMF/THF: 50/50. The evaporation times are 0 sec and 15 sec respectively.

Series green: 15wt% SVP-1 in DMF/THF: 30/70

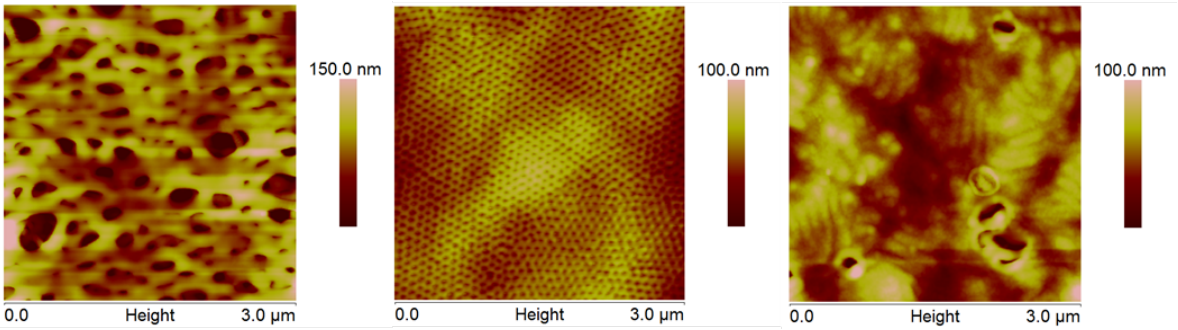

Figure S5. AFM height images of polymer membranes cast from a solution of 15 wt% S2VP-1 in DMF/THF: 30/70. The evaporation times are 0 sec, 15 sec, 30 sec, 40 sec and 60 sec respectively.

Series blue: 15wt% SVP-1 in pure THF

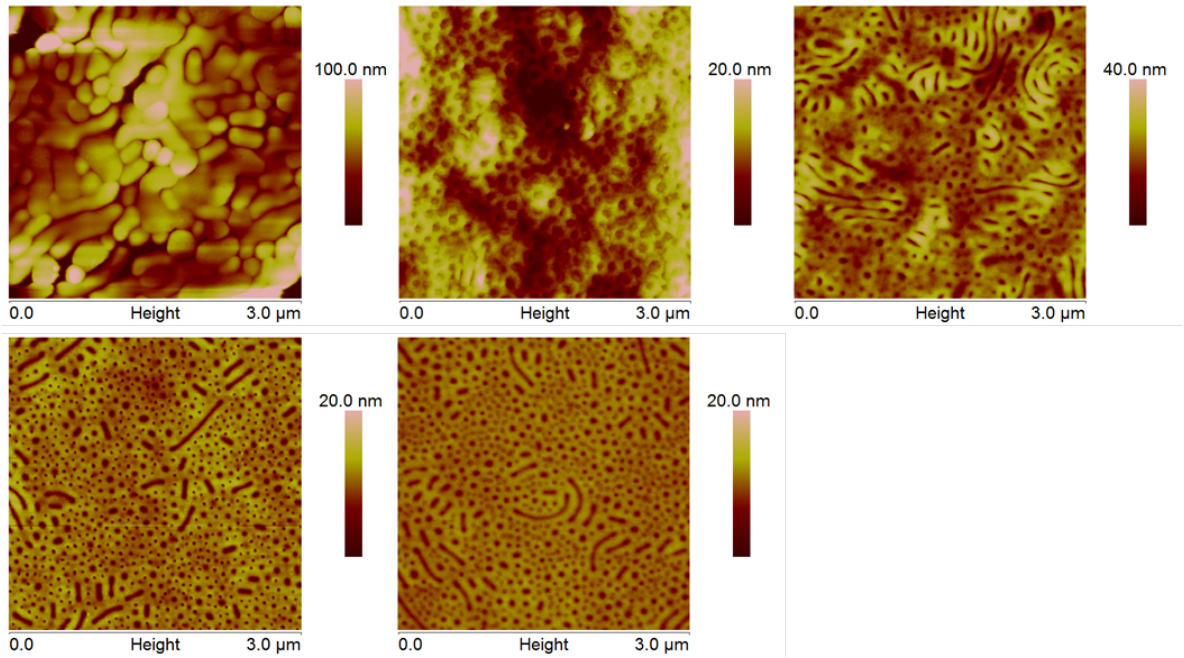

Figure S6.AFM height images of olymer membranes cast from a solution of 15 wt% S2VP-1 in pure THF. The evaporation times are 0 sec, 15 sec, 30 sec and 60 sec. The last image was taken from a completely dried membrane.

Series orange: 10 wt% SVP-1 in pure THF

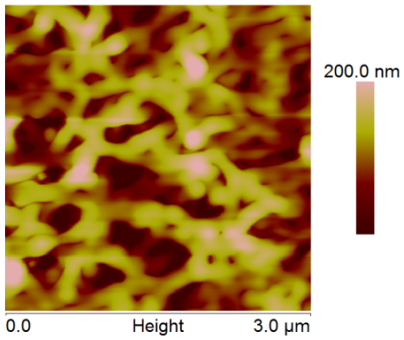

Figure S7. AFM height image of a polymer membrane cast from a solution of 10 wt% S2VP-1 in pure THF.

Series red: 20 wt% SVP-1 in pure THF

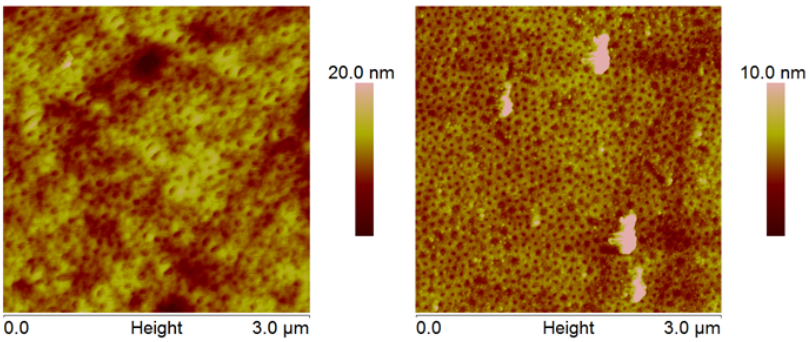

Figure S8. AFM height images of polymer membranes cast from a solution of 20 wt% S2VP-1 in pure THF.

5 Evaporation-induced Block Copolymer Self-assembly into Membranes Studied by *in situ* Synchrotron-SAXS

[1]Corinna Stegelmeier, [1]Alexander Exner, [1]Stephan Hauschild, [2]Volkan Filiz, [3]Jan Perlich, [3]Stephan V. Roth, [2,4]Volker Abetz, [1]Stephan Förster*

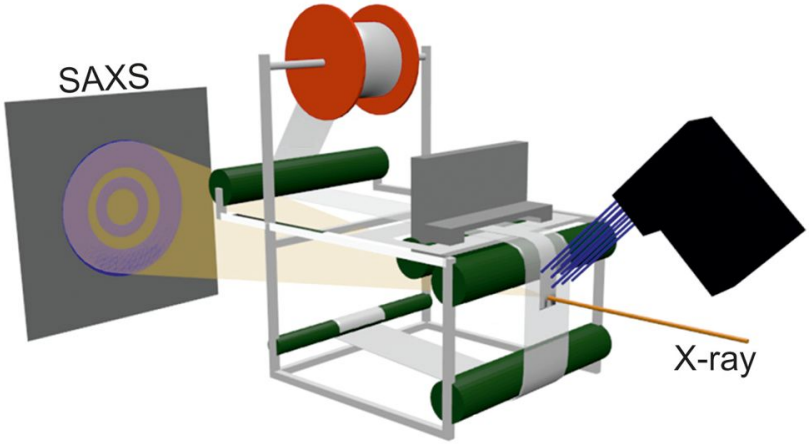

[1]Physical Chemistry 1, University of Bayreuth, Universitätsstrasse 30, 95447 Bayreuth, Germany
[2]Institute of Polymer Research, Helmholtz-Zentrum Geesthacht, Max-Planck-Strasse 1, 21502 Geesthacht, Germany
[3]HASYLAB DESY Hamburg, Notkestrasse 85, 22607 Hamburg, Germany
[4]Institute of Physical Chemistry, University of Hamburg, Grindelallee 117, 20146 Hamburg, Germany

5.1 Abstract

Amphiphilic diblock copolymers can spontaneously form integral asymmetric isoporous membranes by evaporation-induced self-assembly. The critical structural evolution steps occur within the first hundred seconds after solvent casting. By using synchrotron X-ray scattering employing a specially designed solvent casting apparatus we were able to follow the kinetics

of the structural evolution *in situ*. At an initial time of 20 seconds after solvent-casting we observe the first structural features on length scales *d* of 30 - 70 nm, signaled by a weak maximum in the low-*q* region of the measured scattering curves. During the subsequent period the length scales increase continuously until after around 100 seconds they reach a plateau value d_∞ of 80 - 120 nm, the size depending on the molecular weight of the block copolymer. Interestingly, the time evolution of the characteristic length scales follow a simple exponential saturation curve for all block copolymers, irrespective of molecular weight, composition and addition of ionic additives, in agreement with theoretical models on two-dimensional ordered block copolymer domain formation. In addition we could show that immersion in water during solvent evaporation leads to a nearly instantaneous increase of the characteristic length scale to its plateau value. The addition of salts such as Cu^{2+} leads to compaction of the structures with smaller characteristic length scales, but still following the same kinetic evolution.

5.2 Introduction

Among the most common wet film formation methods to prepare well-defined homogeneous thin films with defined thickness are spin-coating and doctor-blading. They both involve the evaporation of solvent, a process whose pathway significantly influences the structure of the resulting film, depending on local concentration gradients of the dissolved components. Transient structures may be formed, being trapped by rapid changes in molecular mobility such that the resulting film structure corresponds to a frozen non-equilibrium state. Thus the film formation process of multi-component systems, which are very common e.g. in industrial formulations, can be very complex. The structural pathways that lead to the final structure may in many cases be reconstructed from the analysis of the starting and final structure of the film. Still, only a fast *in situ* structural characterization technique that would allow to monitor the structural evolution in real time would give valuable information about the actual evaporation and self-assembly process, and the temporal evolution into the final structure.

Scattering techniques are particularly suitable to study fast structure formation processes *in situ*, as they do not require sample preparation or fixation to determine the sample structure at given times during the process. Mostly *in situ* X-ray scattering has been used, particularly to investigate the self-assembly of block copolymers into ordered structures during

solvent annealing or evaporation-induced self-assembly.[54,37,125,39,126] One of the recent very promising developments in this area is the spontaneous formation of integral asymmetric isoporous membranes via a simple block copolymer solvent-casting/evaporation procedure.[22] The method involves dissolving a block copolymer in a mixed-solvent system which is cast into a thin film, from which the more volatile solvent evaporates to induce the formation of a dense nanoporous skin. This structure is then trapped by immersion in water, a procedure which remarkably yields in one step integral asymmetric isoporous membranes with a high density of very uniform open pores in the top separation layer (skin) above a macroporous, asymmetric sublayer providing mechanical support. Such membranes are of high interest for water-purification and protein separation.

The success of this method very delicately depends on many material and process parameters. So far intensive work has been done to characterize and understand the complex structure formation process using established methods of electron and scanning force microscopy to reconstruct the structural evolution.[120,118,93] However, only *in situ* studies would provide relevant details about the structural evolution to understand the significance of various factors on the structure during membrane formation. Very recently, time-resolved GISAXS-studies were carried out during the membrane formation process[102]. With a time-resolution of 20 seconds it was possible to observe the appearance and growth of a characteristic length scale which corresponded to the d-spacing of the ordered pores. GISAXS probes changes of the surface and also sub-surface structure, depending on the incidence angle. It would be highly interesting to obtain *in situ* structural information of the complete film cross-section during evaporation, particularly in the first 100 seconds where the critical structural changes take place.

We report the first *in situ* investigation of the structural evolution of the evaporating block copolymer film using transmission synchrotron small-angle scattering (SAXS) during the first 200 seconds after solvent casting with a time resolution of 5 seconds. For the *in situ* investigation we designed an apparatus that allows one to prepare a thin homogeneous wet film of well-defined thickness using doctor blading on a tape that is translated through the X-ray beam to probe fast evaporation-induced structural changes *in situ*. Unexpectedly, we find that the growth of the characteristic length scales follows a common, simple exponential saturation curve, irrespective of block copolymer molecular weight, composition and the addition of ionic additives, in agreement with theoretical predictions on ordered block copolymer domain

formation.

5.3 Experimental Part

Block copolymers

The PS-*b*-P4VP block copolymers were synthesized by living anionic polymerization in tetrahydrofuran at $-70\,^{\circ}C$ following standard procedures reported in literature[98,127]. Table 5.1 summarizes the block copolymers used in this work. All polydispersities are <1.1.

Table 5.1. Molecular weights of the P4VP-*b*-PS block copolymers used in this study. Column 3 lists the molar fraction of the hydrophilic P4VP-block while columns 4 and 5 summarize the plateau values d_∞ and the characteristic growth times τ obtained by an exponential saturation fit.

	M [g/mol]	f(4VP)	d_∞ [nm]	τ [s]
S4VP-1	100 000	0.25	63.2	51
S4VP-2	180 500	0.14	115	28
S4VP-3	252 000	0.25	123	27
S4VP-1+$CuCl_2$	100 000	0.25	56.8	50

Sample preparation

In order to investigate the influence of block copolymer molecular weight, block length ratio, addition of metal ions, and immersion in water on the phase separation behavior, solutions of P4VP-PS (15 - 25 wt%) with different molecular weights and composition (see Table 5.1) were prepared in solvent mixtures of THF and DMF (30/70) and used for the phase separation studies with the device described in the following paragraphs.

Synchrotron small-angle X-ray scattering

The SAXS-experiments were performed at HASYLAB/DESY Hamburg at the beamline BW4 (λ = 0.138 nm) with a sample-detector-distance of 8 to 11 m. For the detection of the scattering patterns a PILATUS 300K fast-readout-detector or a MarCCD-camera was used.

In situ SAXS film formation experiments

For the experiments a continuous film-casting device was developed as depicted in fig. 5.1. It

casts a thin polymer film from a viscous solution onto a moving support film. We used commercially available parcel tape (TESA®-film), which is optically transparent and transparent to X-rays with negligible background scattering over the whole q-range of interest (0.02 – 0.2 nm^{-1}). The polymer solutions can be continuously cast via syringe pumps and a doctor blade, which is positioned on top of the continuously moving tape. It is wound-up by a motor with variable speed.

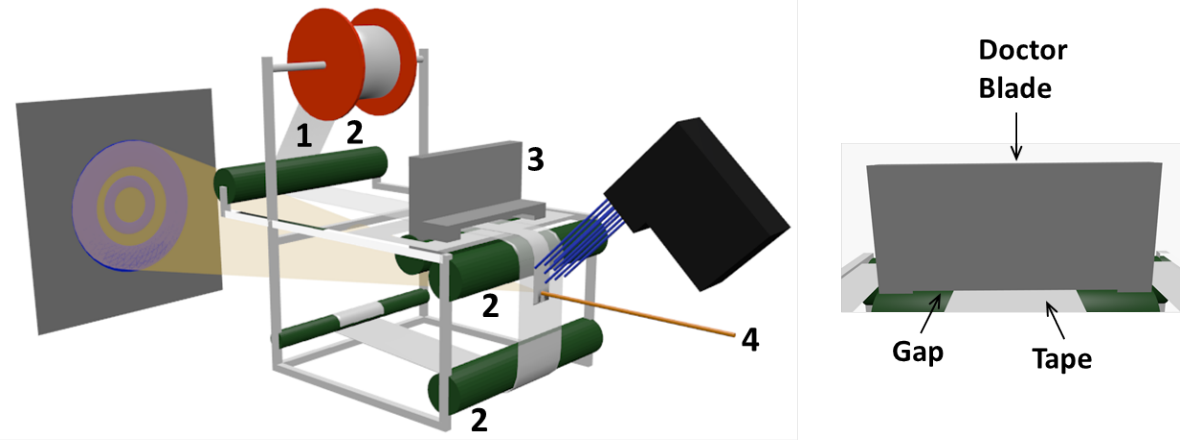

Figure 5.1. Schematic drawing of the automatic film casting apparatus (left) and a close up of the doctor blade (right). The arrows in the close up indicate the position where the polymer solution (not depicted) is cast into a film of 200 μm in thickness through the gap. Included is also the inkjet printer used for simulating the phase inversion with water. 1 = moving tape, 2 = guide roller, 3 = doctor blade, 4 = X-ray beam.

This setup allows one to prepare a homogeneous film with well-defined thickness in the range of 50 - 200 μm. The film is transported over guide rolls into the X-ray beam, which probes the film structure after a certain distance from the doctor blade. Depending on the films translation velocity, this distance corresponds to a certain evaporation time after film preparation.

The doctor blade consists of two metal plates with a variable gap, in the present study of 200 μm, thus providing a constant film thickness. The moving tape is transported by a motor with adjustable speed and around three guide rollers. After the first guide roller the tape reaches the doctor blade where the polymer solution is applied to the substrate using a syringe pump with a flow rate of 0.5 to 1.0 mL/min. The solution is immediately cast into a thin film with a thickness of approximately 200 μm given by the gap height, and directed around the second guide roller until it arrives at the position, where it is illuminated by the X-ray beam.

Subsequently the polymer film is wound up via a third guide roller. For the time scales to be probed in the experiment, we performed a stopped-tape experiment, where first the film is doctor bladed on the moving tape and then stopped at the position of the X-ray beam to follow the structural evolution at this position.

The initial dead time of the experiment corresponds to the time needed for translating the tape from the doctor blade to the position of the X-ray beam, which is ca. 5 seconds. In tests using continuously moving tapes we found that during this initial phase the solution is homogeneous, with very low featureless small-angle scattering, and no noticeable changes in the scattering patterns. After the tape is stopped, the structural evolution can be probed with a temporal resolution limited by the frame rate of the detector and the minimum signal-to-noise ratio needed for high quality scattering patterns. For the experiments discussed below, we used exposure times of down to 5 seconds to continuously follow the film formation process. This setup requires a low-noise detector with a short read-out-time to minimize the accumulation time of each frame and thus to optimize the time-resolution. The device can be placed and aligned in a synchrotron beam and can be remotely controlled from outside the synchrotron hutch. The supporting structure is adjustable in height and length to position the sample area probed by the X-ray beam relative to the position of the doctor blade.

Set up including inkjet printer

To mimic the immersion in water, we used a HSAJet® Micron MCHP1 inkjet printer to homogeneously spray an excess volume of water onto the film with a defined amount per unit area. The inkjet printer (see fig. 5.1) was positioned such that after an arbitrary evaporation time (ca. 30 - 40 s) water could be sprayed on the film for 5 s approx. 3 cm above the spot where the X-ray hits the tape. The wetted part of the film was subsequently transferred into the beam as fast as possible.

With this casting apparatus in principle every kind of evaporation process can be studied *in situ*. The only practical limitation is that the drying film adheres well to the tape surface and has a sufficiently high viscosity to prevent gravitational flow down the vertically moving tape at the position of the X-ray beam. By using different gap heights and tape velocities, the shear rates upon film formation could be varied to also study alignment and orientation processes during film formation. Technically, it is also possible to use this apparatus for GISAXS or GISANS measurements.

5.4 Results and Discussion

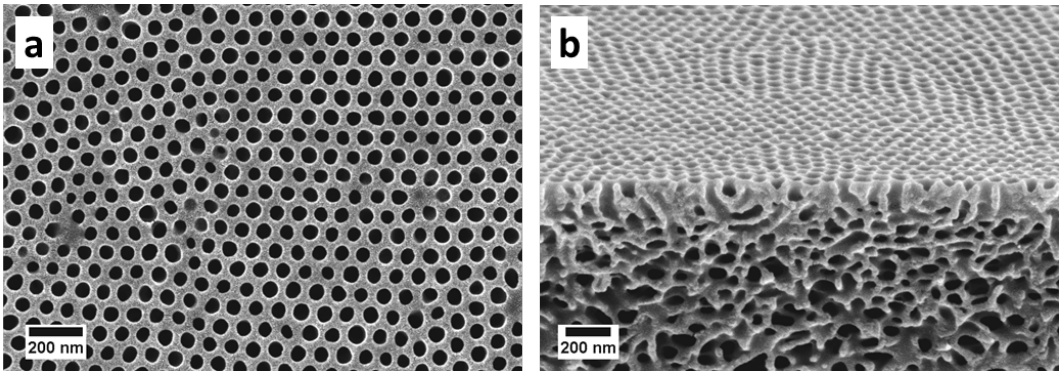

Figure 5.2. (a) SEM surface image of a nanoporous integral asymmetric membrane prepared from a solution containing 22 wt% of block copolymer S4VP-3 in DMF/THF: 60/40, immersed in water after an evaporation time of 11 sec. (b) SEM cross sectional image of a membrane (22 wt% of S4VP-3 in DMF/THF: 60/40, immersed in water after an evaporation time of 11 sec), showing the cylindrical pores in the top layer. The pore-to-pore distance in the top layer is 81 nm.

For our investigations we chose a set of different P4VP-PS block copolymers varying in molecular weight and composition in a DMF/THF solvent mixture (see Table 5.1) which is used to form integral asymmetric membranes as shown in Fig. 5.2. The SEM-images show the regular array of uniform pores at the membrane surface together with an SEM-image of the cross-section visualizing the top pore layer together with the bicontinuous support structure. The samples were obtained by solvent evaporation for 11 seconds and subsequent immersion in water, following a standard procedure to prepare integral asymmetric membranes.[22]

A) Temporal evolution

Fig. 5.3a shows a series of scattering patterns measured for an evaporating block copolymer solution of 25wt% S4VP-1 in a solvent mixture consisting of 70 wt% DMF and 30 wt% THF during the first three minutes after doctor blading. This is the time during which most of the solvent evaporates. The first measurement is made 10 s after doctor blading. We observe a weak Debye-Scherrer ring appearing after 35 seconds. Its intensity increases and its position moves to smaller q-values towards the primary beam position during subsequent measurements. Since the measured scattering patterns are all isotropic, data reduction proceeded by measuring the bare support film for background subtraction followed by azimuthal averaging

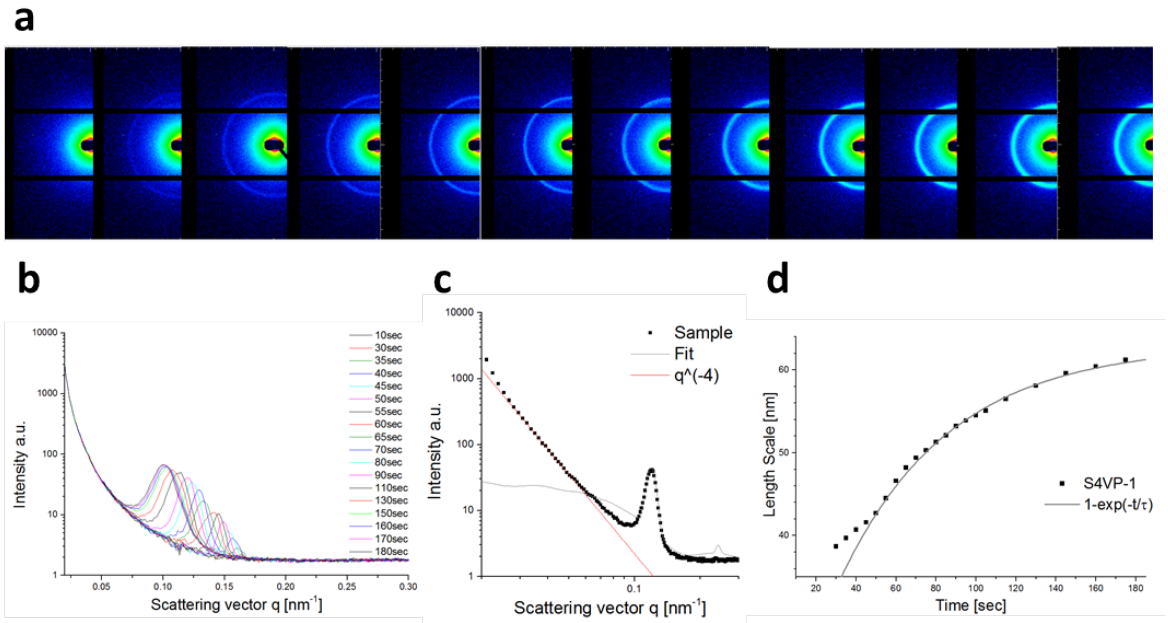

Figure 5.3. 2D-scattering patterns measured for an evaporating block copolymer solution of 25wt% S4VP-1 in a solvent mixture consisting of 70 wt% DMF and 30 wt% THF 10, 35, 40, 45, 50, 55, 60, 65, 70, 90, 125 and 185 seconds after film casting; (b) sectorially averaged 1D-intensities obtained from scattering patterns detected every 5 seconds, (c) scattering curve measured after 90 seconds together with a fit to the observed peak (grey line) and a straight line indicating a q^{-4}-Porod law (red line), (d) characteristic length scale obtained from the peak position as a function of evaporation time together with a fit to a $[1 - exp^{(-t/\tau)}]$-law.

the 2D-patterns to obtain the corresponding scattering curves *I(q)* (for details see Supporting Information).

The obtained series of scattering curves is shown in Fig. 5.3b. The shift of the peak to lower q-values is clearly observable. It reaches a minimum *q*-value of $0.099 nm^{-1}$ after approximately 160 seconds. The scattering curves are characterized by a strong increase at low q-values following approximately a q^{-4}-Porod scaling typical for the surface scattering of the developing pore system. The peak in the intermediate q-range can be described by a Gaussian peak shape function as shown by the fit (solid gray line) in Fig. 5.3c. The peak position q^* can be related to a corresponding characteristic length scale d^* via $d^* = \frac{2\pi}{q^*}$. The increase of this characteristic length scale with time is shown in Fig. 5.3d.

The increase of the characteristic length d^* upon evaporation is at first counter-intuitive, but can be explained by the onset of microphase separation and increasing interfacial segregation

of the system during evaporation of THF, which is a slightly selective solvent for PS.[93,102,121] The evaporation of THF increases the concentration of DMF, which is a selective solvent for the P4VP-block. This leads to the onset of microphase separation with corresponding chain stretching of the block copolymer. The subsequent evaporation-induced further increase of the domain spacing d^* related to the increasing interfacial chain segregation has very recently been quantitatively investigated and successfully described on the basis of theoretical predictions for the intermediate segregation regime.[48] The observed peak widths indicate a certain variance of the pore-to-pore distances. The measured FWHM for samples during solvent evaporation is shown in Fig. S6, indicating a ca. 40% increase until the domain size reaches the plateau value which is likely due to spatial inhomogeneities of the solvent evaporation process during the experiment.

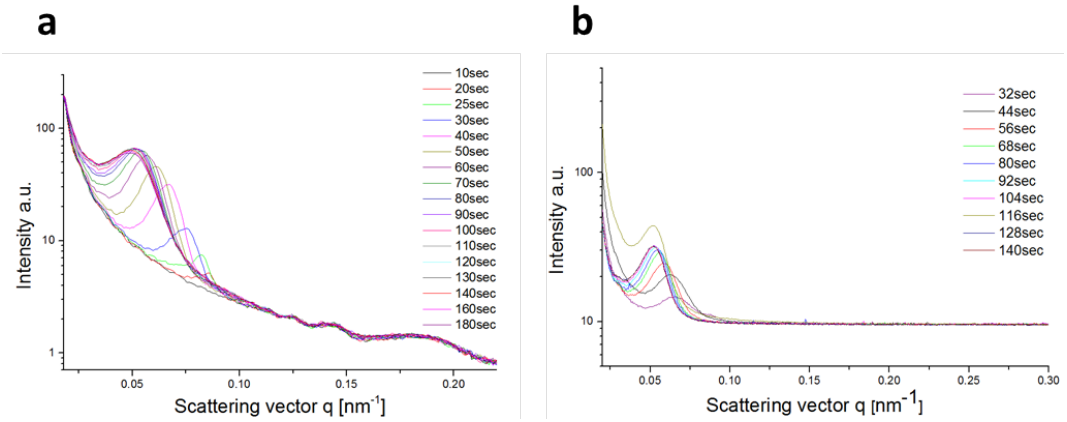

Figure 5.4. (a) Series of sectorially averaged scattering intensities for the higher molecular weight block copolymer S4VP-3 (15 wt% in DMF/THF: 70/30, and (b) the more compositionally asymmetric block copolymer S4VP-2 (20 wt% in DMF/THF : 70/30). Both show qualitatively the same behavior as S4VP-1, i.e. a shift of the peak position to lower q-values and an increase in intensity upon solvent evaporation.

Fig. 5.4a shows the series of measured scattering curves for the higher molecular weight block copolymer S4VP-3 at a concentration of 15 wt% in DMF/THF: 70/30. The first measurement is made 10 s after doctor blading. The first peak is observed after 15 seconds at a peak position of $q = 0.08 nm^{-1}$, which corresponds to a pore-to-pore distance of 79 nm, in good agreement with the pore-to-pore distance of 81 nm observed in the SEM-images in Fig. 5.2, which were obtained after an evaporation time of 11 seconds and then immersed in water to trap the structure. Due to the higher molecular weight of the block copolymer, the peak positions are

observed at smaller q-values, below 0.1 nm^{-1} compared to the lower molecular weight S4VP-1, where peaks are observed between 0.15 and 0.1 nm^{-1}. Fig. 5.4b shows the measured scattering curves for the compositionally more asymmetric block copolymer S4VP-2 (f_{PVP} = 0.14) at a concentration of 20 wt% in DMF/THF : 70/30. Also here we observe a systematic shift of the peak position to lower q-values during evaporation. The first measurement is taken after 20 s while the peak was first observed after 32 seconds.

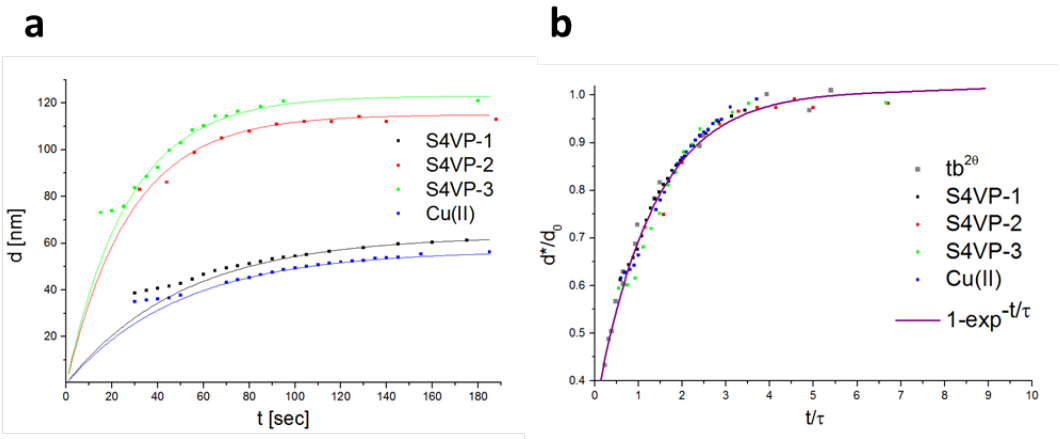

Figure 5.5. (a) Characteristic length scales during evaporation as a function of time for the three block copolymers S4VP-1, S4VP-2, S4VP-3 and the block copolymer/salt-system S4VP-1/Cu(II). Solid lines indicate fits to a simple exponential saturation curve, (b) the same data, rescaled to a reduced time and a reduced length scale showing the common behavior of all investigated block copolymer systems, together with a theoretical prediction indicated by $tb^{2\theta}$.[97].

Fig. 5.5a shows the characteristic length scales during evaporation as a function of time for the three block copolymers S4VP-1, S4VP-2, S4VP-3 and the block copolymer/salt-system S4VP-1/Cu(II). They all show the same trend, i.e. the characteristic length scales reach a plateau value after ca. 60 to 100 seconds. The solid lines indicate a fit to a simple exponential increase described by

$$d^* = d_\infty(1 - exp[-\frac{t}{\tau}]) \tag{5.1}$$

This simple equation describes the data surprisingly well, except in a time regime at very short times, where a linear increase starting from an offset d_0 is observed. A fit to eq. 5.1 allows to determine the plateau values d_∞ and the characteristic growth times τ. These values are summarized in table 5.1. We observe that the plateau value d_∞ increases with

increasing molecular weight of the block copolymer, similar as the growth times τ decreases with increasing molecular weight, although not as systematically. The ratio between plateau value d_∞ and initial offset d_0 is 0.6 for all neat block copolymer systems.

Ordered domain growth usually proceeds via a sequence of characteristic growth regimes involving different transport mechanisms. For many systems, after an initial transient regime the characteristic size of the domains grows with a power law $d \sim t^n$, where n is the domain growth exponent, whose value depends on the domain shape, nucleation mode and rate-determining growth process, i.e. either diffusion- or surface reaction-limited growth. In our case of the evaporation-induced ordered block copolymer domain formation we do not observe a power-law dependence. The observed exponential saturation curve is, however, in good agreement with a theoretical study of two-dimensional ordered block copolymer domain growth based the Cahn-Hilliard-Cook model.[97] Accordingly, after an initial phase with an approximately linear behavior, the study similarly reports a simple exponential saturation of the domain growth to an upper limit of the characteristic length scale. Their master curve (Fig. 4 in ref. [15]) is reproduced in Fig. 5.5b which well superimposes on the measured data points of the present study, indicating that the observed domain growth behavior may be a characteristic feature of a two-dimensional structure such as the ordered skin-layer of the evaporating block copolymer film.

B) Water immersion

For isoporous membrane preparation the cast solvent-swollen polymer film is immersed in a non-solvent like water after a certain evaporation time, preferably when the film has just developed the highly symmetric hexagonally ordered pore structure in a matrix of the glassy PS-block. To effectively trap the ordered porous structure the cast film including the support is quickly plunged into a water bath. To investigate possible structural changes during water immersion *in situ*, we used a special setup involving an inkjet printer to spray in a well-defined and reproducible way a pre-defined volume of water onto the film mimicking the immersion process in the water bath.

Fig. 5.6 shows the measured scattering curves upon solvent evaporation, with immersion in water after 45 seconds for the block copolymer S4VP-1 at the same concentration and solvent composition investigated before (25 wt%, DMF/THF 70/30). During the initial evaporation phase we observe the appearance and low-q shift of a peak as described before. The first

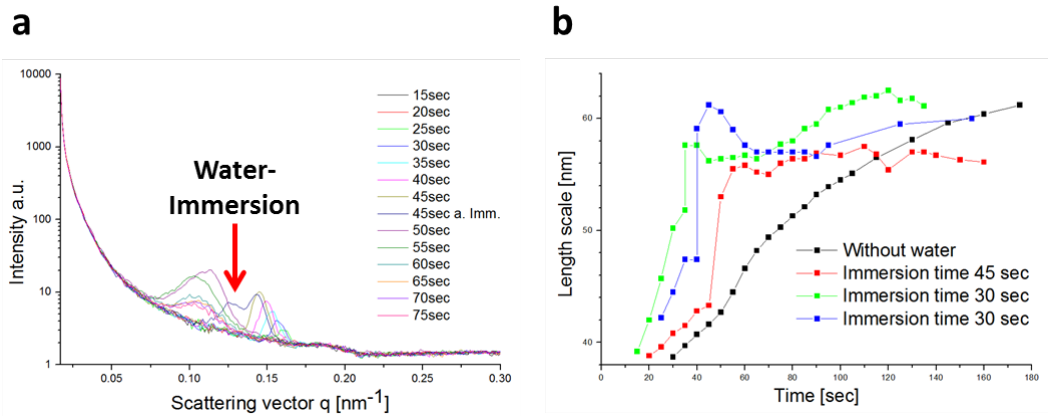

Figure 5.6. (a) Scattering intensities and (b) calculated length scales of an evaporating polymer solution of S4VP-1 (25 wt%) in DMF/THF 70/30. Water was sprayed onto the film after 30 s (green and blue line) and after 45 s (red line).

measurement after water immersion shows two peaks, the first one shifted to *slightly* lower *q* ($0.145 nm^{-1}$) compared to the previous measurement ($q^* = 0.147 nm^{-1}$), and the second peak of similar intensity appearing at *much* lower *q*-value ($q^* = 0.126 nm^{-1}$). The observation of two separate peaks is related to the coexistence of sample domains that have already structurally responded to the water immersion and sample domains, where water immersion has not yet affected the structure. In the subsequent measurement we observe only one peak shifted to still lower *q* ($q^* = 0.115 nm^{-1}$) until in the following measurements it only slightly changes its position, which corresponds well to the final position of the evaporation experiment without solvent immersion. Upon water immersion we see a quite pronounced increase of the FWHM as shown in Fig. S6, indicating pronounced sample inhomogeneities induced by this process.

Fig. 5.6b shows the measured characteristic length scales d^* for the three immersion experiments together with the experiment without water immersion. The two experiments at immersion times of 30 s serve to investigate the reproducibility of the structural changes upon immersion with water. We observe in all cases, that the immersion does not freeze or fix the structure, as we expected, but rather induces a rapid increase of the characteristic length scale, within 2 seconds, to the final saturation length scale *d*. This length scale is equal to the length scale d_∞ obtained for the dry sample after slow evaporation of solvent. The transient time of 2 seconds is of the order of magnitude that is expected for the diffusion of water ($D \sim 10^{-9} m^2/s$) over a distance equal to the thickness of 100 μm of the film (1.7 s). We note

that the observed jump to the length scale d_∞ upon immersion in water means that the inkjet water immersion process does not fully trap the structure and therefore does not effectively mimic the real water immersion process in the water bath, as was used for the preparation of the porous membranes shown in Fig. 5.2. It shows that only a fast immersion process in a large excess of the non-solvent water can fully trap the transient pore structure. This is in line with our observation that all samples that we investigated at the synchrotron, where none of them was treated using fast excess water immersion, had lost the pore structure in the surface layer when investigated two days later after returning from the synchrotron. This demonstrates the importance of the structure trapping process for success porous membrane production.

C) Addition of Salt

Because the stability region of the ordered pore phase is small, methods have been developed to increase the stability. One method is based on the use of coordinating metal salts such as $CuCl_2$ [26–28]. The metal ions coordinate to the nitrogen of the pyridine groups, thereby crosslinking the PVP-domains and improving the stability of the ordered pore network and thus broadening the time frame for the membrane preparation where the pore-network is stable.

Fig. 5.7 shows the measured scattering curves during evaporation of solvent for the block

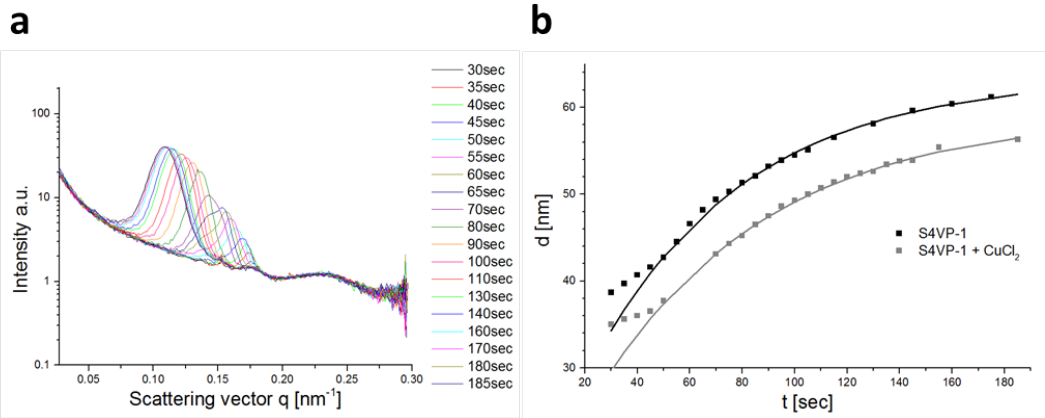

Figure 5.7. (a) Scattering curves and (b) calculated length scales of a solution of the block copolymer S4VP-1 (25 wt%, DMF/THF 30/70) containing 0.15 wt% $CuCl_2$ as a complexing agent (gray line) and for comparison the pure polymer solution (black line). The experimental data follow the fit of an exponential saturation (solid gray and black lines).

copolymer S4VP-1 (25 wt%, DMF/THF 30/70) containing 0.15 wt% of copper(II)-chloride. We observe a similar intensity increase and low-q shift of the peaks as in the experiment with the

block copolymer solution without added salt. A comparison of the length scales shows that in case of added Cu^{2+}, the characteristic length scales d^* are $\sim 10\%$ smaller throughout the evaporation process. The plateau value is $d_\infty = 63nm$ without Cu^{2+}, and $d_\infty = 57nm$ with added Cu^{2+}. This indicates a compaction of the structure, but the structural evolution is practically the same in both cases, i.e. $\tau = 51s$ without Cu^{2+}, and $\tau = 50s$ with added Cu^{2+}. This compaction may be expected when considering the additional attractive interaction mediated by the coordinative bonds.

5.5 Conclusions

In this work we investigated the formation of integral asymmetric block copolymer membranes by evaporation-induced self-assembly *in situ* for block copolymers of different molecular weights, composition, addition of salt, and immersion in water during the first 200 seconds, where the critical structural evolution steps occur. We observe that during solvent evaporation and development of ordered domains the characteristic length scales follow a simple exponential saturation curve, irrespective of molecular weight, composition and addition of ionic additives, in agreement with theoretical models on two-dimensional ordered block copolymer domain formation. The addition of salts such as Cu^{2+} leads to compaction of the structures with smaller characteristic length scales, but still following the same kinetic behavior as without ionic additives. Further we observe that immersion in water during solvent evaporation does not freeze the sample structure, as was expected, but leads to a nearly instantaneous fast increase of the characteristic length scale to its final plateau value. These studies thus provide new important insights into the membrane self-assembly behavior, which helps identifying the narrow time window for the film immersion in water to obtain the required isoporous membrane structure. The observed systematic characteristics aid to better guide and predict structural evolution during evaporation-induced self-assembly to obtain the desired final topology.

Acknowledgment:

We thank the EU (Project #228652, *SELFMEM*) and the German Science Foundation (SFB 840 –TP B9, C. S.) for financial support. Also we thank Franz Fischer (UBT) for helping us during the development of the film casting apparatus, Kristian Buhr (HZG) for the preparation of the membrane shown in Figure 5.2 and Brigitte Lademann (HZG) for the synthesis of S4VP-3.

5.6 Supporting Information

Background Subtraction

To further illustrate the procedure of data analysis Figure S1 exemplarily shows the scattering intensities of one measurement frame (taken from the series depicted in Figure 3) together with the background data which were obtained by measuring the pure tape material (TESA-film). The background intensities were corrected by the ratio of accumulation times for the two measurements (5 s and 5 min respectively) and then subtracted from the sample intensity to render the blue line which was then evaluated as described in Figure 5.3.

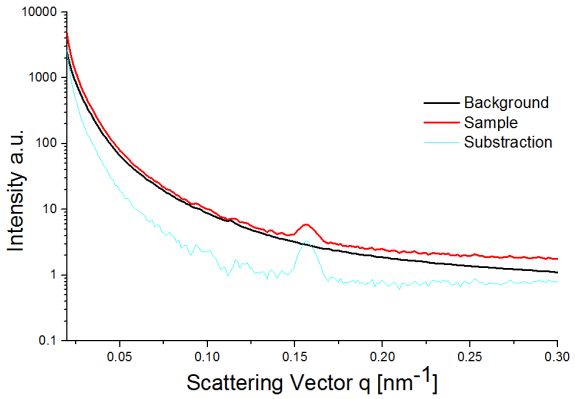

Figure S1. Scattering intensities of the supporting tape (TESA®-film, black line) and a measurement taken during an evaporation series (red line). The blue line shows the corrected scattering intensity obtained by subtraction of the background.

Scattering patterns of the series depicted in Figures 5.3-5.7

In the following the background subtracted scattering patterns of every series in this work are depicted.

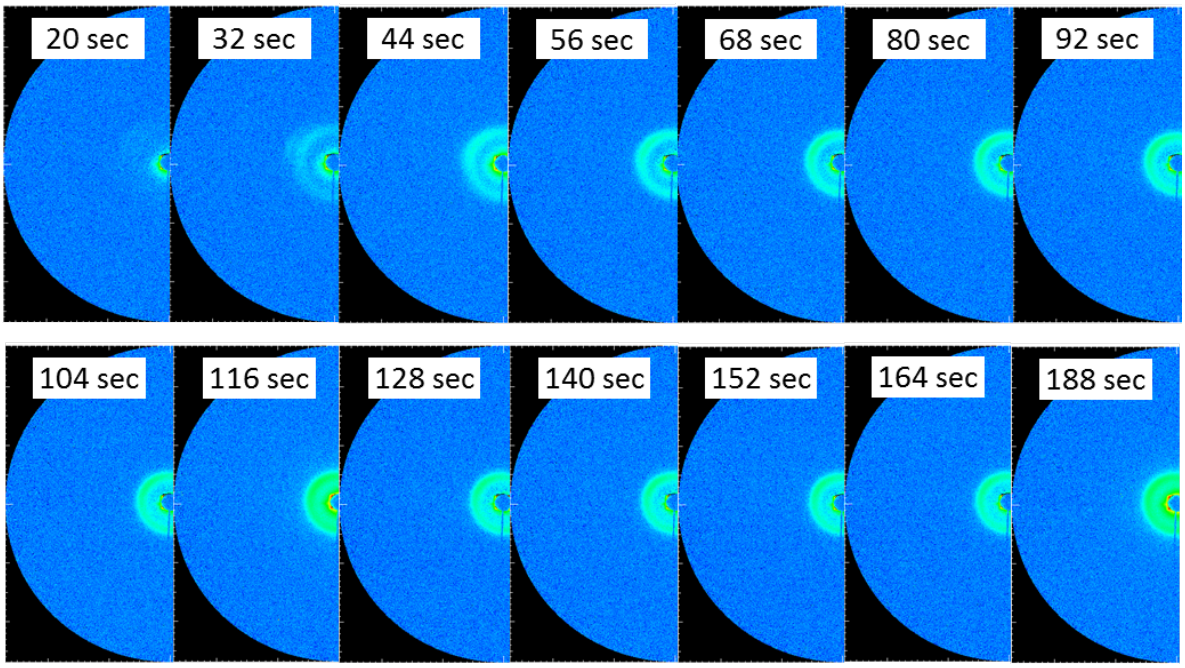

Figure S2. Measured scattering patterns of an evaporating polymer solution of S4VP-2; 20 wt%; DMF/THF : 70/30; Measurement: 10 s frames every 12 s

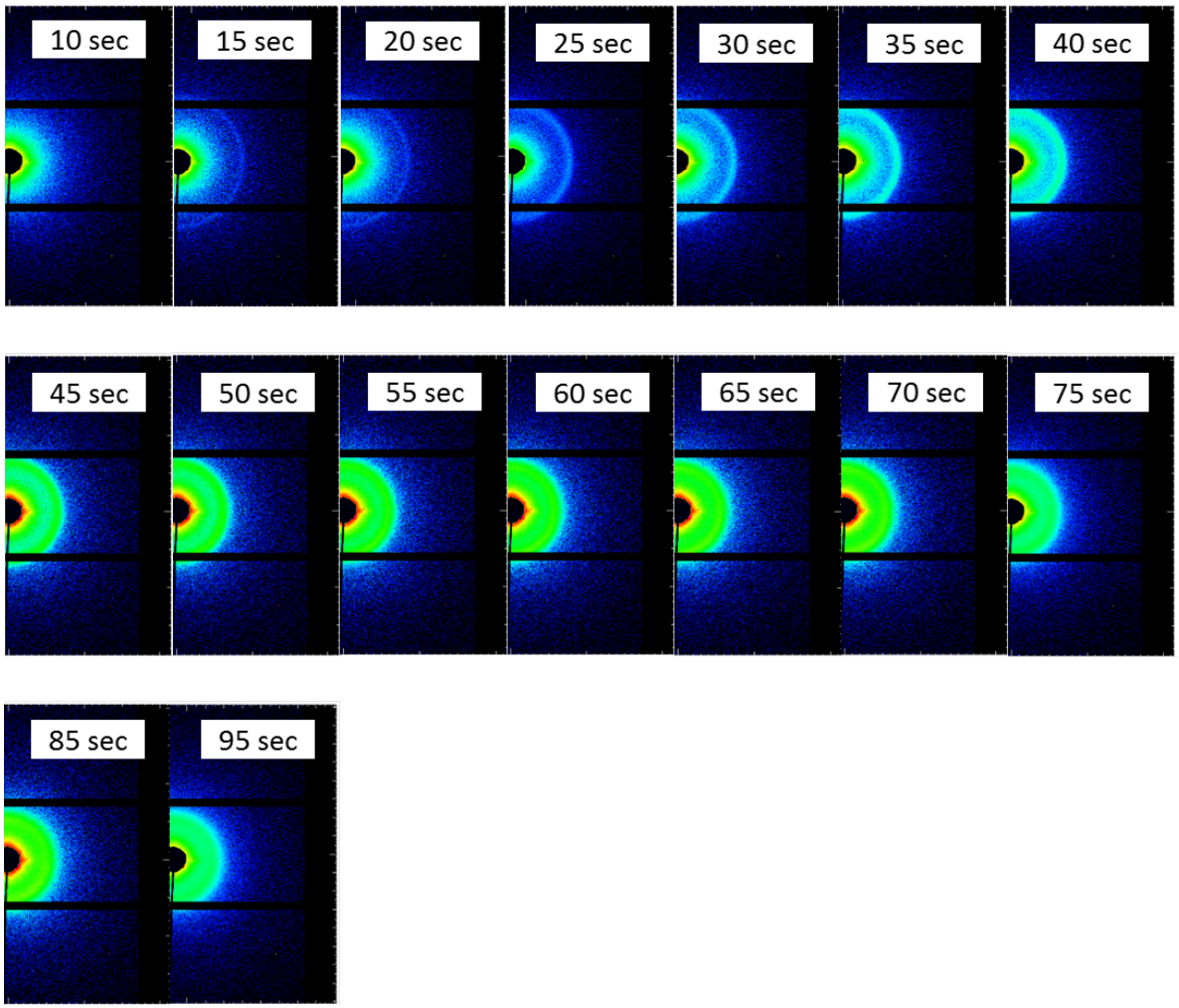

Figure 5.8. Figure S3. Background subtracted scattering patterns of an evaporating polymer solution of S4VP-3; 15 wt%; DMF/THF : 70/30; Measurement: 5 s frames every 5 s

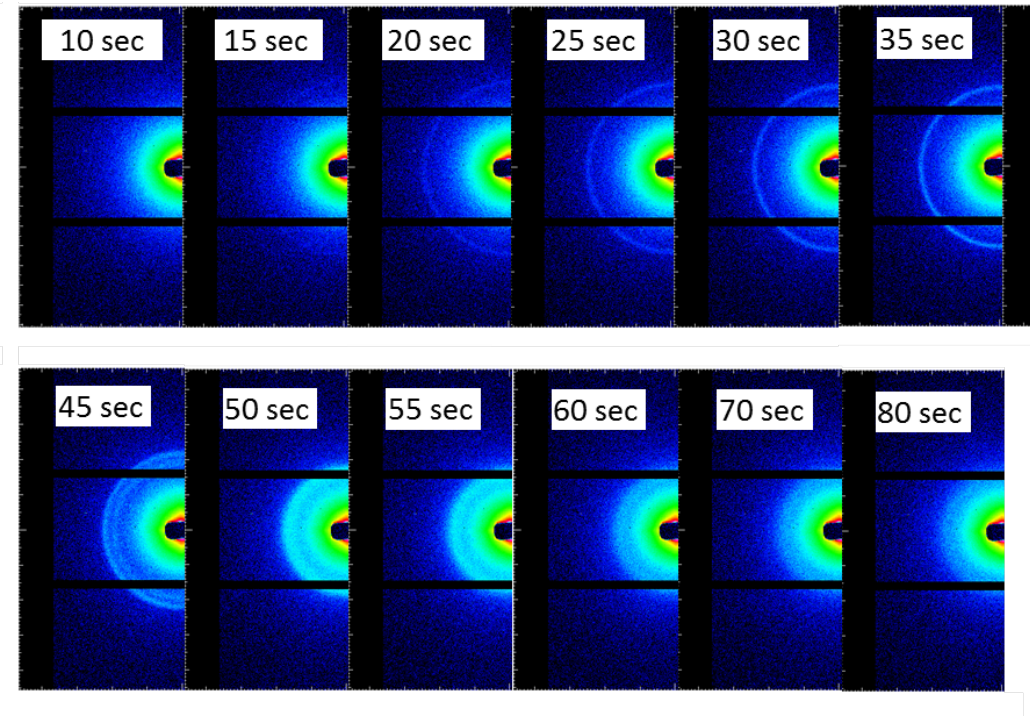

Figure S4. Background corrected scattering patterns of an evaporating polymer solution of S4VP-1; 25 wt%; DMF/THF : 70/30; Measurement: 5 s frames every 5 s. Immersion time in water: 45 s.

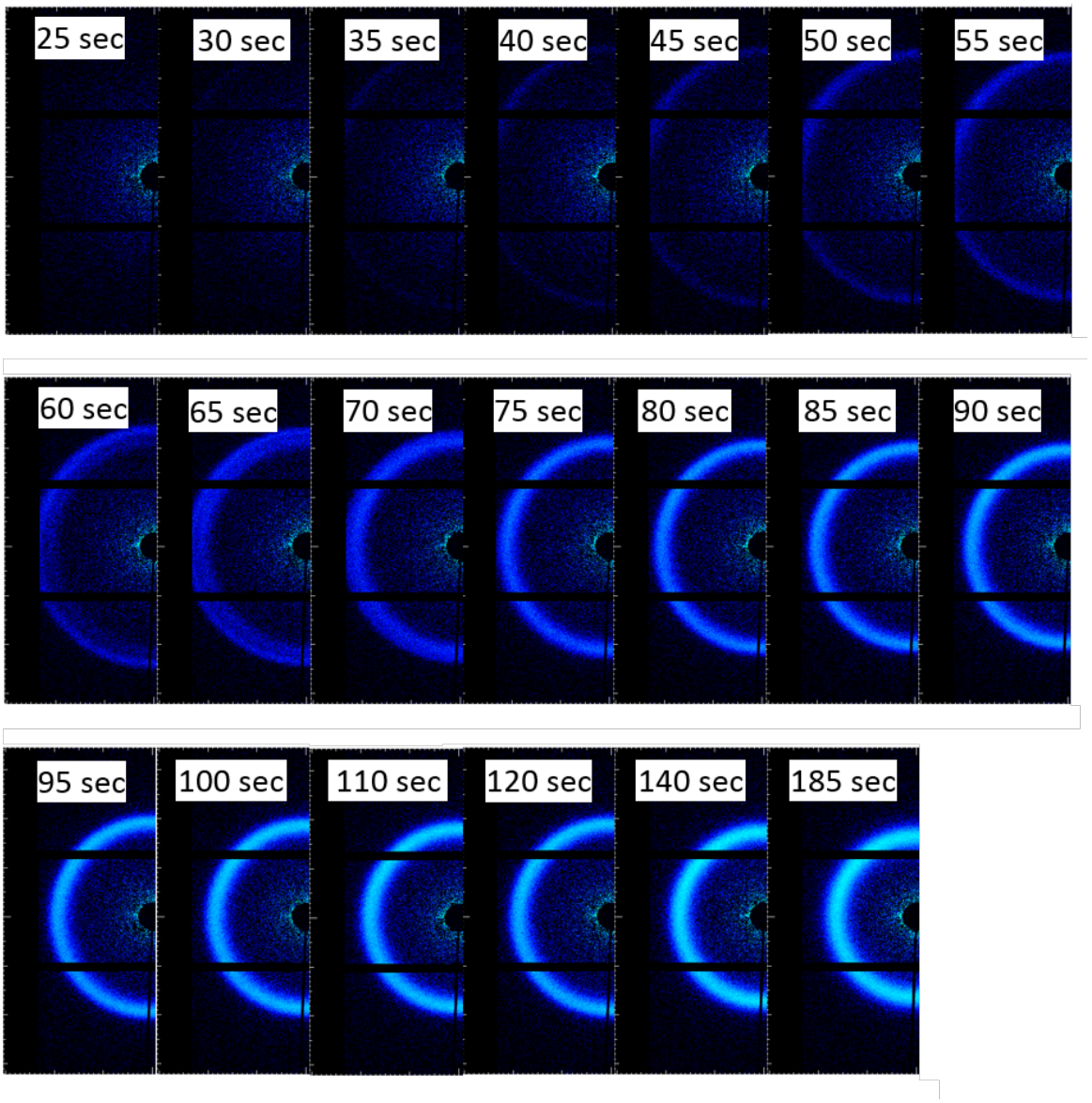

Figure S5. Background corrected scattering patterns of an evaporating polymer solution of S4VP-1; 25 wt%; DMF/THF : 70/30; Measurement: 5 s frames every 5 s. As an additive the solution contained 0.15 wt% of copper(II)-chloride.

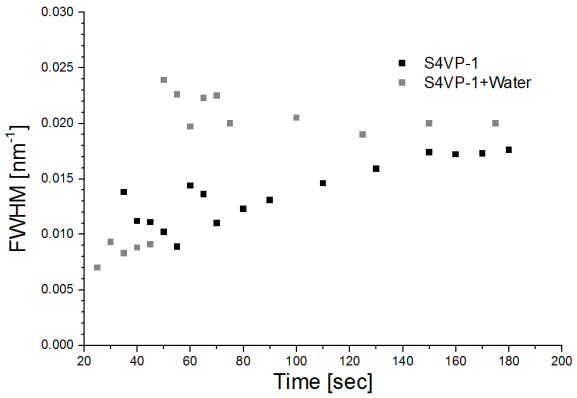

Figure S6. FWHM-values measured for a sample S4VP-1 (25 wt%; DMF/THF : 70/30) with and without water immersion.

6 Functionalization and Stabilization of Self-Assembled Blockcopolymer Membranes by Nanoparticles

[1]*Corinna Stegelmeier,* [1]*Sara Mehdizadeh Taheri,* [1]*Sascha Ehlert,* [1]*Katharina Ottermann,* [2]*Andreas Fery,* [1]*Stephan Förster*

[1] Physical Chemistry I, University of Bayreuth, Universitätsstrasse 30, 95447 Bayreuth, Germany

[2] Physical Chemistry II, University of Bayreuth, Universitätsstrasse 30, 95447 Bayreuth, Germany

6.1 Abstract

Self-assembled integral asymmetric block copolymer membranes are receiving increased attention because of the elegant one-step preparation method and the resulting well-defined high-density nanopore structure. In order to specifically functionalize these membranes it would be desirable to incorporate functional nanoparticles. We show with the example of superparamagnetic nanoparticles that the incorporation of nanoparticles in a controlled way is possible by applying a mixed polymer coating that specifically directs them to the interface of the poly(styrene-*block*-2-vinylpyridine) block copolymer domains. We find that the polymer coating in addition prevents nanoparticle aggregation and *via* stabilization of the interface broadens the time window for the kinetic stabilization of the desired nanoporous membrane structure.

6.2 Introduction:

Ensuring reliable access to clean and affordable water is one of the greatest global challenges of this century. In this respect, membrane-based water and wastewater treatment systems are gaining much interest for efficient purification and filtration.[128,129] To meet new material demands nanocomposite membranes are increasingly considered, which contain added

nanoparticles to provide improved material properties or new material functions. Nanoparticles can improve adsorption properties because of their high surface area and specific surface interactions. Commonly investigated materials include carbon nanotubes (CNTs) for metal and organic contaminant removal, as well as Fe_3O_4- and TiO_2-nanoparticles as effective, affordable adsorbents for heavy metals and radionuclides.[130]. For separation applications Fe_3O_4-nanopoarticles with superparamagnetic properties have been investigated that allow easy separation in weak magnetic fields[131]. For (photo)catalysis mostly TiO_2-nanoparticles are used. Nanoparticles with antimicrobial properties for disinfection and biofouling include Ag-, ZnO-, TiO_2-, Ce_2O_4, Al_2O_3, CNTs, and fullerenes[132].

The addition of nanoparticles will have a significant effect on the membrane formation mechanism. As optimization of membrane structure and properties with addition of nanoparticles may require to screen a large number of material and processing parameters, a rational design for nanocomposite membranes would greatly afford this procedure. If successful, the integration of nanoparticles may even allow one to tune membrane microstructure to improve stability and permeability.

Different methods to incorporate nanoparticles into polymer membranes have been considered. These include the integration of nanoparticles *via* surface self-assembly onto prefabricated membranes, or the addition to the membrane casting solution. It is also possible to synthesize the nanoparticles within the membrane by incorporating inorganic precursors *via* metal-coordinating groups and subsequent chemical reaction.[133,87] Favorably, the method of loading the nanoparticles into the membranes can be integrated in existing membrane fabrication technology requiring minimum changes in existing manufacturing processes.[134]

One of the most efficient and promising methods to prepare integral asymmetric membranes with a very high density of uniform pores in the nanometer range is based on block copolymer self-assembly during a phase inversion process.[22] The method involves dissolving an amphiphilic block copolymer in a mixed-solvent system to produce a casting solution, which is doctor-bladed into a film. The more volatile solvent is then evaporated for a period of tens of seconds before immersing the film in a coagulation bath containing a non-solvent, mostly pure water, to induce phase inversion to obtain the desired integral asymmetric membrane structure with a top layer with a high density of uniform pores (typically > 1014 pores/m^2). It would be highly desirable to use this method to directly integrate nanoparticles into block copolymer membranes. Many methods to load nanoparticles into block copolymer scaffolds have been

worked out in recent years.[92,81,80,91,135]

A complication of the described membrane preparation method is the narrow time window during which the desired ordered pore structure can be trapped. Typically a precise evaporation time, which is in the range of 10-30 seconds depending on the block copolymer/solvent system, has to be used to trap the ordered pore structure by immersion in water. If the membrane is immersed too early, then spinodal-type pore networks are obtained, whereas at longer evaporation times ordered non-porous cylinder morphologies are developing. The transient structures that develop during solvent evaporation have been recently investigated in detail.[93]

If nanoparticles are added, this will likely affect the stability ranges of the transient structures such that new optimized membrane formation conditions would have to be found. We were therefore seeking a rational design of the nanoparticle/block copolymer system to afford stabilization of the desired pore structure. As was recently shown[136] nanoparticles can be directed to the interface of block copolymer domains by a mixed surface coating of the corresponding two homopolymers. We expected that this method to direct nanoparticles to the interface would allow the controlled localization of the nanoparticles within the block copolymer membrane and could also stabilize the domain structure similarly as amphiphilic nanoparticles in Pickering emulsions.[137] The stabilization of the nanoporous transient structure has recently been approached with the use of transition metal salts that selectively stabilize domains by complex formation.[28,27]

In this work we describe the controlled integration of nanoparticles into the block copolymer domains of the membrane. We chose superparamagnetic iron oxide Fe_2O_3-nanoparticles as an example because of their stability and potential use for magnetic seaparation. As block copolymers we used the established poly(styrene-*block*-2-vinylpyridine) (PS-P2VP) system. The molecular weight and composition of the block copolymer, i.e. PS(760)-P2VP(200), was selected to target a P2VP-cylinder in a PS-matrix morphology. The mixed polymer coated nanoparticles were loaded into the block copolymer domains by mixing in the *N,N*-dimethylformamide (DMF) / tetrahydrofuran (THF) solvent mixture. The PS-matrix structure develops by the evaporation of THF as the more volatile solvent. The membrane structure is trapped after evaporation times from 5-20 seconds by immersion in water. The obtained nanocomposite membranes structures were characterized using atomic force- (AFM), scanning electron- (SEM) and transmission electron microscopy (TEM).

6.3 Experimental Part

Preparation of the polymer-coated nanoparticles

Polymer coated iron oxide nanoparticles were prepared from the nanoparticles stabilized with oleic acid, which had an average diameter of 12.1 nm. The oleic acid ligands were exchanged with end-functionalized P2VP and PS homopolymers. As efficient end-groups that coordinatively bind to the surface of the nanoparticles we used multidentate amino ligands such as pentaethyl hexamine (PEHA). The ligand exchange proceeds by adding an excess polymer ligand in solution to the dissolved nanoparticles, followed by quantitative and subsequently selective precipitation to remove oleic acid and excess free polymer ligand to obtain pure polymer coated nanoparticles. Using different homopolymer ratios (30:70; 50:50 and 70:30) yielded three different mixed polymer coated nanoparticles, which were used for the block copolymer membrane preparation. Also nanoparticles with pure P2VP- and PS-coatings were prepared. Details of the ligand exchange procedure can be found in ref[99].

Preparation of the Hybrid Films

Highly concentrated and viscous solutions of PS-P2VP containing a small amount (0.1wt% -1wt%) of PS and P2VP-coated nanocomposites were prepared in organic solvent mixtures of DMF and THF (40/60). The solutions were doctor bladed into films of approximately 200 μm in thickness *via* the NIPS-method[22,25,26,23] and were allowed to dry for variable short periods of time (seconds) until they were immersed in a non-solvent bath containing water at room temperature. The membranes were dried and prepared for characterization with electron microscopy.

Atomic Force Microscopy (AFM)

The surface topographies of the polymer films were characterized using the commercial atomic force microscope Dimension 3100 equipped with a NanoScope® IV AFM controller both from Vecco Instruments Inc., USA in the Tapping ModeTM. The images were detected using standard cantilevers (OMCL-AC160TS, Olympus, japan) with typical spring constants of 42 N/m and tapping frequencies of 300 kHz with a standard silicon tip (radius 10 nm). The obtained data were processed with the Nanoscope Analysis software.

Scanning Electron Microscopy (SEM)

For the characterization with SEM the block copolymer samples were sputter coated with a platinum layer of 1.3 nm using the Cressington sputter coater 208HR. The Film surfaces were characterized using a Zeiss LEO 1530 scanning electron microscope with a field emission electron gun. The instrument was operated at 2.0 kV and the images were detected using an Inlens SE-detector.

Transmission Electron Microscopy (TEM)

Prepared polymer films were embedded in epoxy resin and microtomed using the Leica Ultra microtome UC7 at room temperature. The ultrathin sections were placed on copper grids and characterized with a Zeiss CEM902 transmission electron microscope operated at 80 kV.

6.4 Results and Discussion

Nanoparticle Coating

The mixed coating of the nanoparticles with P2VP- and PS-homopolymer was achieved *via* a recently established ligand exchange procedure.[65] With this method the oleic acid coating of the nanoparticles, which was required for their synthesis, is replaced by the mixed polymeric P2VP- and PS-ligands.

Figure 6.1 shows TEM images of the obtained polymer-coated nanoparticles. The nanoparticles are well separated and no agglomerated particles are visible which proves a successful exchange of the oleic acid with the P2VP and PS-polymers respectively. A TEM image of the oleic acid stabilized Fe_2O_3 nanoparticles prior to ligand exchange can be found in the supporting information for comparison (see Fig S1).

The polymer-coated nanoparticles were additionally characterized using dynamic light scattering (DLS). Assuming a "brush-like" dense polymer layer around the inorganic core a dependence of the hydrodynamic radius on the polymers molecular weight would be expected as has been shown before for PEO and PS ligands.[100,138] Figure 6.2a shows the normalized size distributions obtained from DLS for nanoparticles coated with two P2VP ligands with different molecular weights (2.5k and 3.7k). For comparison, the original nanoparticles coated with oleic acid are also shown. We observe a shift of the hydrodynamic radius from 6 nm for the oleic acid coated nanoparticles to 10 nm for the P2VP-coated nanoparticles, irrespective

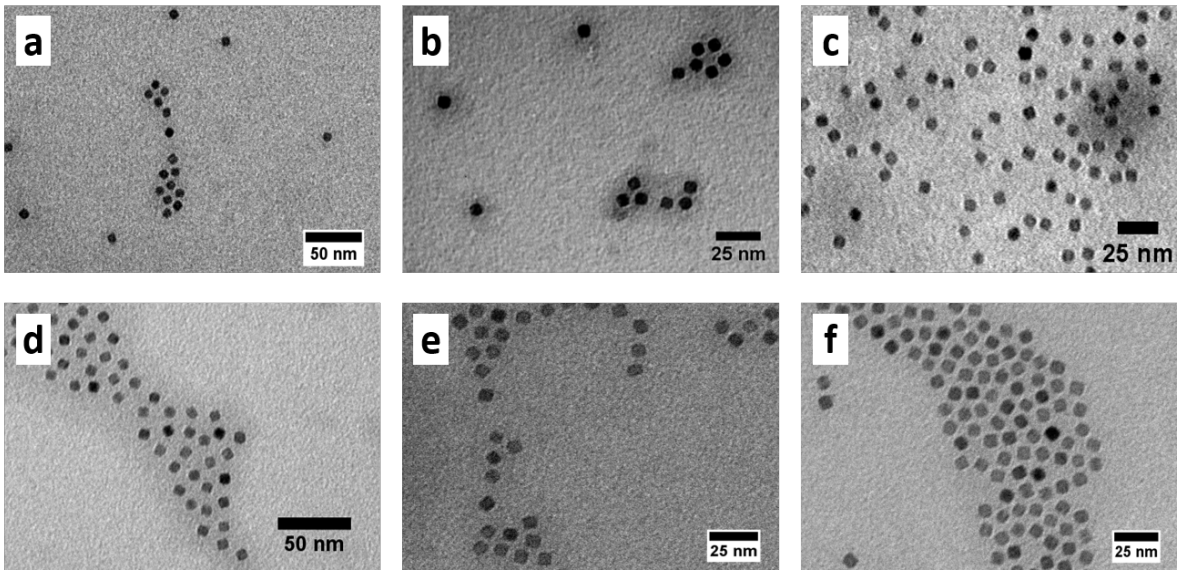

Figure 6.1. TEM images of nanocomposite particles from chloroform solution. The particles were coated with mixtures of PS and P2VP in varying compositions of $30_{PS}/70_{P2VP}$ (a), $50_{PS}/50_{P2VP}$ (b), $70_{PS}/30_{P2VP}$ (c) and with pure PS (d) and pure P2VP-1 (e) and P2VP-2 (f) respectively.

of the molecular weight. The measured 6 nm hydrodynamic radius is in good agreement with the radius obtained from the TEM-images. The shift to a 10 nm hydrodynamic radius for the P2VP-coated nanoparticles is smaller than expected, and independent of molecular weight. This indicates that P2VP is arranged more in the form of a "train-like" conformation on the nanoparticle surface. This more compact shell-structure gives rise to smaller hydrodynamic radii compared to polymer brush structures, where the polymers are only attached with their end-groups. This also indicates that the nitrogen-groups of the vinylpyridine chain can coordinate to the nanoparticle surface.

Figure 6.2b shows the normalized size distribution measured by DLS for the nanoparticles with mixed polymer coatings. The results are summarized in Table 6.1. Included is the size distribution for the oleic acid coated nanoparticles (6nm) as well as the P2VP-coated nanoparticles (10nm) for comparison. We observe the pure PS-coating to have a hydrodynamic radius in the expected range, i.e. 25 nm, which is consistent with a spherical brush structure and in good agreement with previous studies. The mixed PS/P2VP-coatings all have similar hydrodynamic radii with values of 17 nm well in between the two pure homopolymer cases indicating a compacted brush conformation. Further ligand exchange experiments using ligand polymers

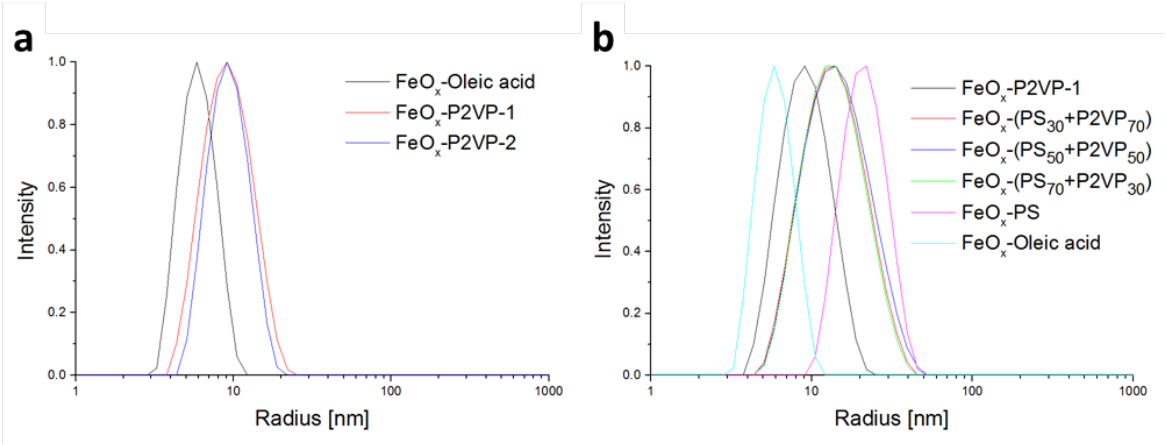

Figure 6.2. DLS intensities of P2VP coated iron oxide nanocomposites using homopolymer ligands of different molecular weights. The original nanoparticles (black line) show a radius of 6.07 nm, the corresponding nanocomposites with P2VP of ca. 2500 g/mol (red line) and P2VP of ca. 3700 g/mol (blue line) have slightly bigger radiuses of 9.62 and 9.59 nm respectively.

without anchor groups showed that also non-functionlized P2VP homopolymers were able to adsorb to the nanoparticle surface, albeit in low amounts (see supporting information). The amino anchor group was found to be necessary for a quantitative exchange of the oleic acid ligands.

Nanocomposite Membrane Preparation

An important aim of the block copolymer membrane casting procedure is to find the conditions in terms of block copolymer molecular weight and composition, polymer concentration, THF/DMF-ratio and evaporation time to trap the desired nanoporous membrane structure. Since with the addition of nanoparticles these conditions could possibly change quite considerably, we started from a well-investigated PS-P2VP block copolymer system where suitable conditions for nanoporous membrane formation had already been optimized.[22,93] When cast from a DMF/THF (40/60) mixture at a polymer concentration of 32.5 wt% the porous membrane structure can be obtained by trapping after 15 seconds evaporation time by immersion in water. SEM images (top and cross-sectional view) of the desired membrane structure are shown in Fig. 5. As seen in Fig. 5a we observe a very regular pore structure in the top layer with pore diameters of 18 nm. The cross-sectional image shows the top layer containing the vertically oriented cylindrical nanopores supported by a continuous larger sponge-like pore

Table 6.1. Hydrodynamic radii of the oleic acid and polymer-coated nanoparticles particles obtained from DLS measurements in chloroform.

Sample	Radius [nm]
$FeO_x - OleicAcid$	6.1
$FeO_x - P2VP - 1$	9.6
$FeO_x - P2VP - 2$	9.6
$FeO_x - PS$	22
$FeO_x - PS_{30} + P2VP_{70}$	15
$FeO_x - PS_{50} + P2VP_{50}$	16
$FeO_x - PS_{70} + P2VP_{30}$	15

structure underneath with pore diameters from 25 nm close to the top layer up to several hundred nanometers further away from the surface. This illustrates the typical integral asymmetric membrane structure that is desired for applications.

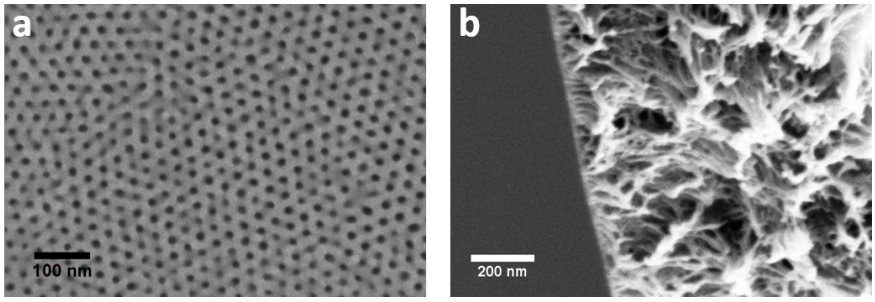

Figure 6.3. SEM images of the surface (a) and the interior (b) of an integral asymmetric membrane prepared from a solution containing 32.5 wt% of PS-P2VP with an immersion time of 15 sec.

For the preparation of the block copolymer nanocomposite membranes the same conditions were used. Before solvent casting the block copolymer and the polymer-coated nanoparticles (0.5, 1 wt%) were dissolved in the DMF/THF-mixture. The amount of nanoparticles was kept at low loading ratios to avoid morphological transitions into other block copolymer morphologies induced by changes in the relative microdomain volume. Yet, the amount should be suitable for magnetic separation. Indeed, we observed the nanoparticle-loaded membranes to be magnetic (see Fig. S6 in the Supporting Information). Nanoparticles with different mixed polymer coatings with compositions P2VP/PS of 30/70, 50/50 and 70/30 were used. The obtained films were characterized using atomic force microscopy (AFM) and transmission electron mi-

croscopy (TEM) on ultramicrotomed thin sections. Ultrathin sections had thicknesses of only 50 nm to clearly identify the microdomain location of individual nanoparticles in the membrane using TEM.

Stabilization of the nanopore structure

Since the time window where the nanoporous membrane structure can be trapped is usually very small and sensitively depends on the process parameters, we were encouraged to find that in the case of added nanoparticles it was possible by using exactly the same conditions. We also found that the time window of the evaporation times was increased, which is very relevant for the successful preparation of membranes.

AFM images of membranes containing 0.5 wt% of nanoparticles are shown in Fig. 6.4. The complete set of images can be found in the Supporting Information. Different top layer morphologies can be identified depending on the nanoparticle content, composition of the polymer layer, and evaporation time. As shown recently, the sequence of morphologies during evaporation is a disordered spinodal network (SpN), followed by the ordered porous structure (PN), which then transforms into a cylindrical phase (OC).[93] This is also observed with the pure PS-P2VP (see Supporting Information, Fig. S5). In the present case we find the spinodal network phase merging into the desired porous morphology after approx. 20 sec ($SpN \rightarrow PN$) which then very quickly transforms into the ordered cylindrical phase ($PN \rightarrow OC$). The nanocomposite membranes showed a larger stability region of the ordered porous structure (PN). The PN-structure develops already during the first seconds after solvent casting and eventually transforms into ordered cylindrical OC-phase.

The high P2VP-content 30/70 mixture exhibits the transition into the nanoporous phase ($SpN \rightarrow PN$) already after 2 seconds with the subsequent formation of the cylinder phase ($PN \rightarrow OC$) already after 8 seconds. The 50/50 mixture shown in the middle panel also shows a very fast transition into the nanoporous phase after 2 seconds with the subsequent formation of the cylinder phase after 10 seconds. The high PS-content 70/30-mixture also showed a very fast stabilization of the nanoporous phase after 3 seconds, with a considerably prolonged stabilization of this phase where after 20 seconds the transition into the ordered cylinder phase was observed. The complete set of AFM images corresponding to varied evaporation times can be found in the Supporting Information.

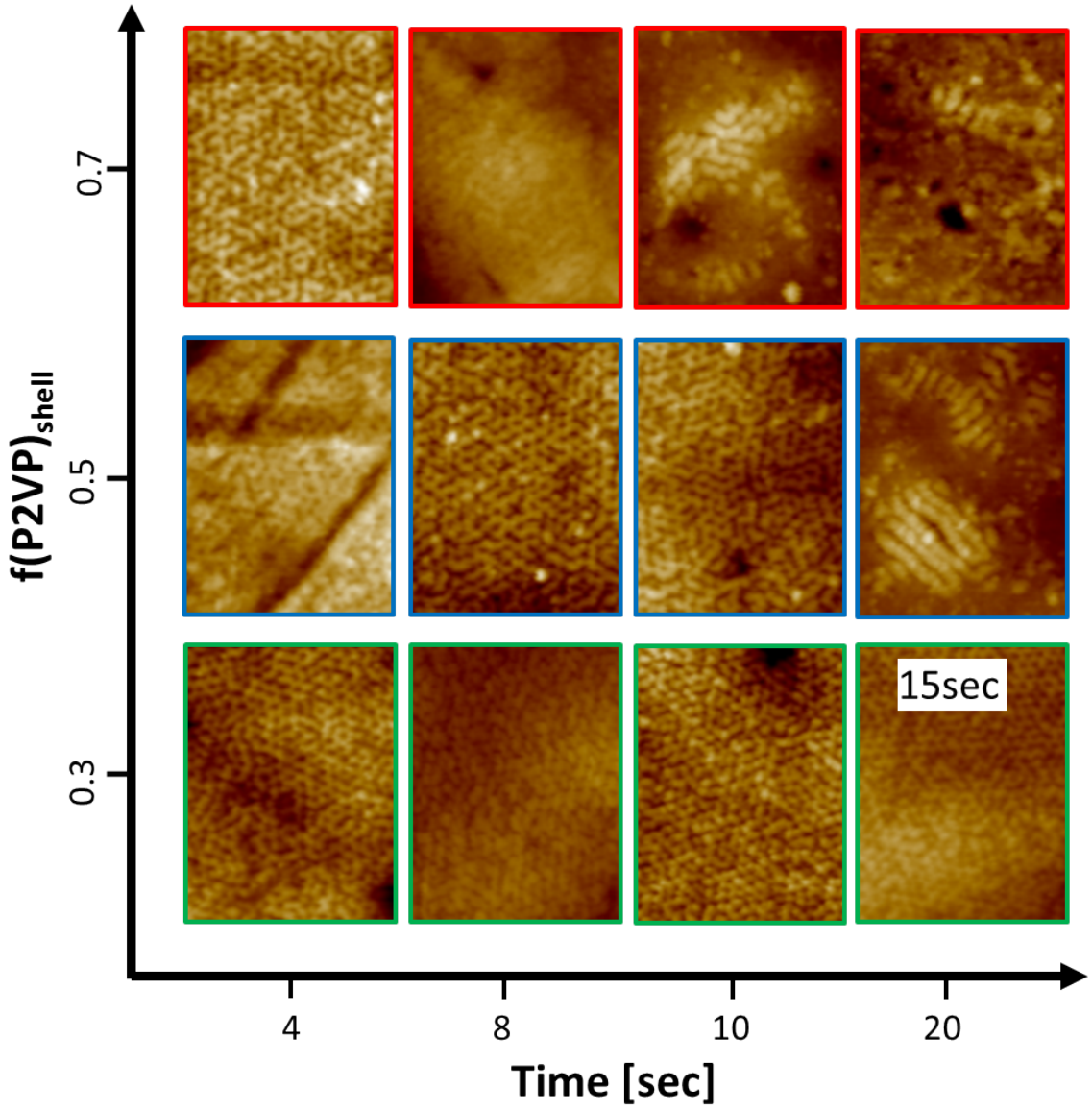

Figure 6.4. AFM images of membranes prepared from casting solutions containing 32 wt% of PS-P2VP and 0.5wt% of nanocomposite particles in DMF/THF : 40/60. The nanoparticle shells consist of different homopolymer ratios PS/P2VP. Red frames: 30/70; blue frames: 50/50; green frames: 70/30. Evaporation times are varied between 4 and 20 sec.

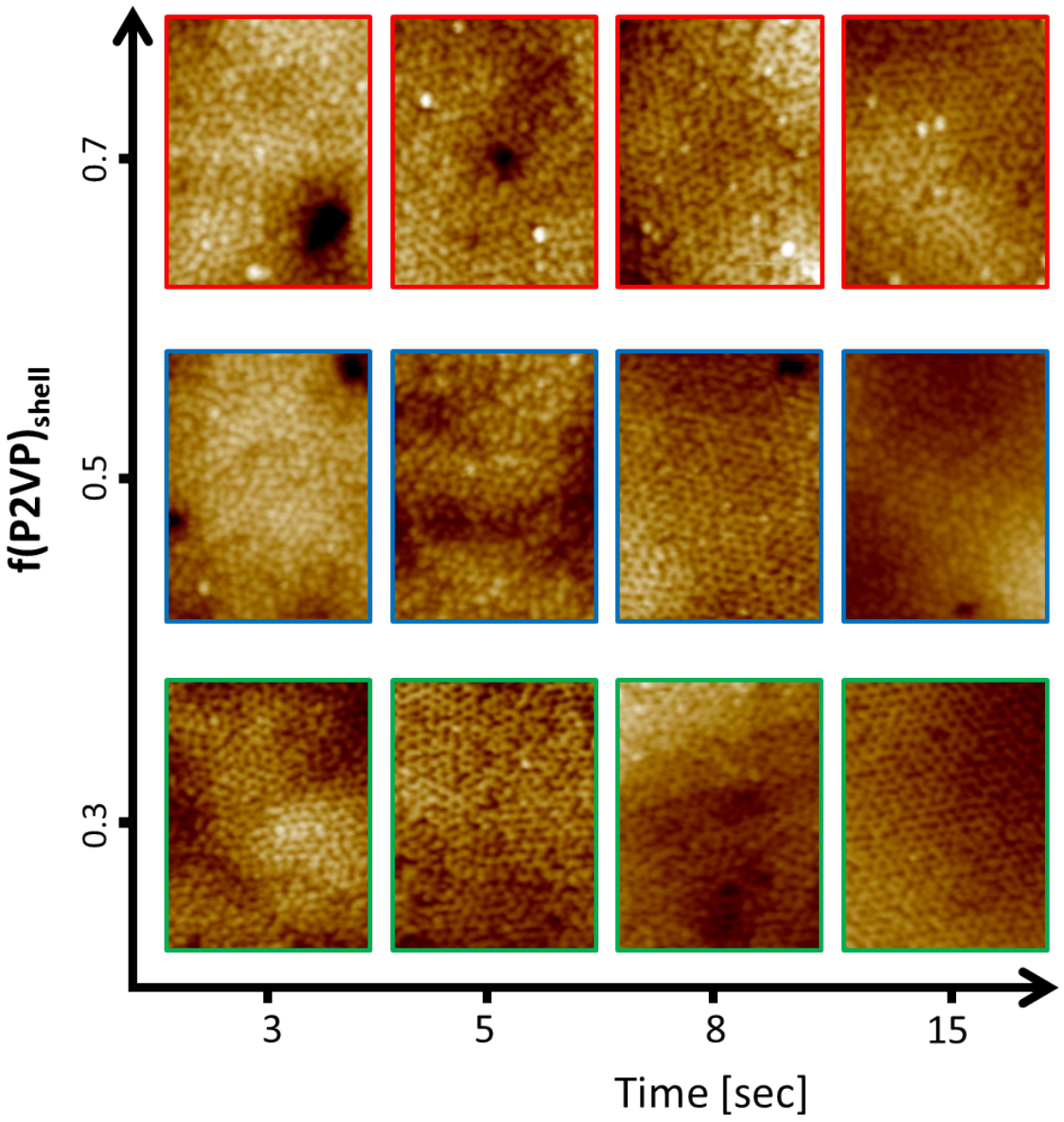

Figure 6.5. AFM images of nanocomposite membranes prepared from casting solutions containing 32 wt% of PS-P2VP and 1wt% of nanocomposite particles in DMF/THF : 40/60. The nanoparticle shells consist of different homopolymer ratios PS/P2VP. Red frames: 30/70; blue frames: 50/50; green frames: 70/30. Evaporation times are varied between 3 and 15 sec.

An increase of the nanoparticle content to 1 wt% lead to further stabilization of the desired nanoporous phase. The stability range of this phase was between 2 and 20 seconds for the P2VP/PS 70/30- and 50/50-mixed nanoparticle coating, and similarly between 2 and 22 sec-

onds for the 30/70-mixed coating. Figure 6.5 shows AFM images of membranes containing 1wt.% of nanoparticles. The complete set of images can be found in the Supporting Information.

The shift of the stability window to shorter evaporation times together with its broadening is very useful for successful membrane formation. Figure 6.6 shows a scheme outlining in detail the stability regions of the found morphologies.

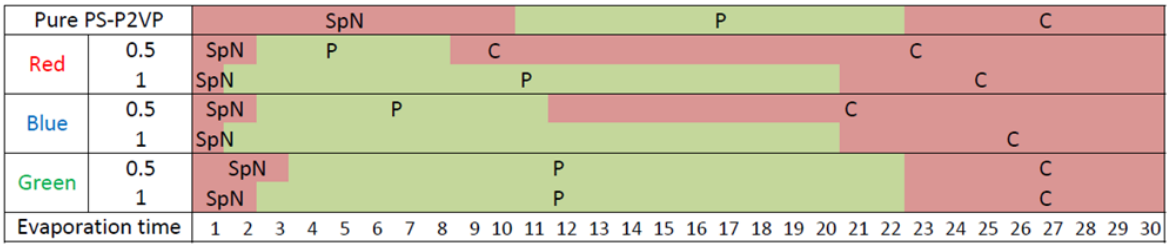

Figure 6.6. Summary of the morphologies found on nanocomposite membranes including different nanoparticle batches (red, blue and green series) at different concentrations and evaporation times. The green blocks (labeled "P") represent the stability regions of the highly porous and continuous PS-matrix while the red blocks stand for the morphologies occurring before and after, the spinodal network (SpN) and the cylindrical phase (OC). For comparison, the pure PS-P2VP morphologies are filled in the diagram as well.

We find our observations of shifted morphology stability in line with theoretical predictions derived from SCFT/DFT theory on the influence of domain-selective nanoparticles on the morphology of block copolymers. The addition of nanoparticles can drive phase transitions from between different block copolymer morphologies.[139] Shifts of morphological stability regions have for example been observed upon the addition of domain-selective CdSe-particles for different block copolymer systems[80,87,139].

We assume that the nanoparticles localize in the domain interfaces and thus stabilize domain segregation already in very early states during evaporation. As the nanoporous phase is the first well-defined ordered fully segregated morphology during solvent evaporation, this morphology is stabilized by the added nanoparticles. Their low mobility further provides kinetic stability against subsequent phase transitions. Thus the $PN \rightarrow OC$ transition is delayed by the nanoparticles, thus stabilizing the porous network structure. Similar to our observations, Sun et al.[140] showed that CdS nanoparticles can stabilize a BCC structure in PS-PEO block copolymers against further structural transformation. For lower nanoparticle loadings,

we observe a dependence of the nanopore stability on the mixing ratio of the coating. As the $PN \rightarrow OC$ transition is driven by an increase of the P2VP-volume fraction due to swelling with DMF, it can be delayed by PS-rich nanoparticle coatings.

Nanoparticle localization

In order to determine the nanoparticle location inside the block copolymer membrane, the membranes were microtomed into ultrathin sections of approx. 50 nm in thickness and examined using transmission electron microscopy (TEM) after selectively staining the P2VP-domains with iodine. Figure 6.8 shows the obtained cross sectional images of nanocomposite membranes with different shell compositions. The amount of nanocomposites was 0.5 wt%. The images show three different shades of gray. Figure 6.7 illustrates which polymer domain is assigned to which gray scale.

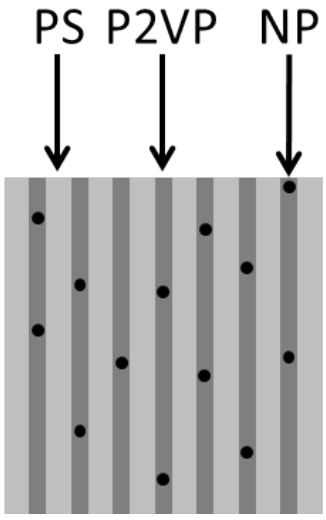

Figure 6.7. Schematic illustration of the gray scales observed in the TEM images. Dark gray stained domains are assigned to the P2VP domains, while medium gray domains represent the PS domains. Everything brighter is attributed to the epoxy resin the samples were embedded in prior to microtome cutting. The black spots are the iron oxide nanoparticles.

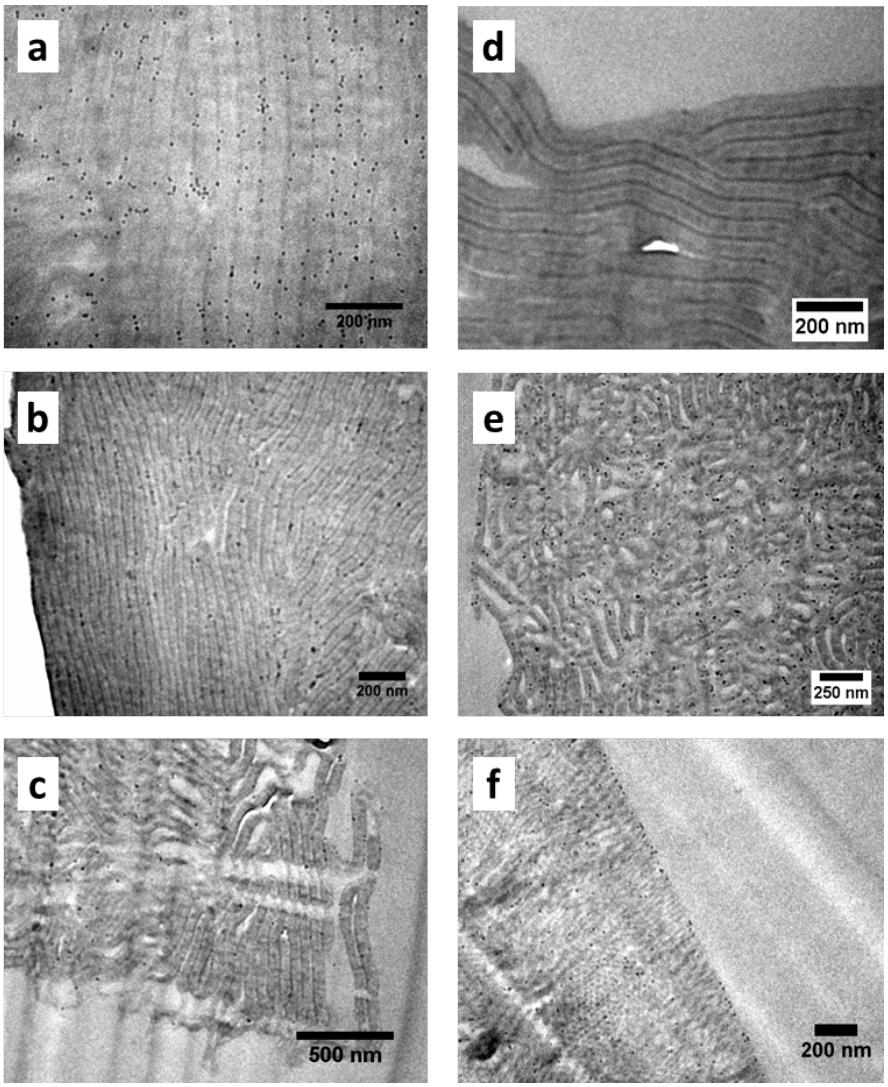

Figure 6.8. Ultrathin TEM cross sections of nanocomposite membranes with nanoparticles with different shells. (a) $70_{PS}/30_{P2VP}$, (b) $50_{PS}/50_{P2VP}$, (c) $30_{PS}/70_{P2VP}$. For comparison, nanoparticles coated with pure P2VP (d) and pure PS (e) were also embedded. (f) TEM image of the mesoporous surface area. Nanoparticle content is 0.5 wt.%

The TEM images show the cross-sections of the cylindrical domains. The domain sizes can be determined to be 19 nm for the P2VP-domains and 46 nm for the PS-domains. The diameter of the nanoparticles is 12 nm, not encluding their polymer coating. They are thus comparable in diameter to the cylindrical P2VP-microdomain size. From Figs. 6.8a-e it can be observed that the nanoparticles prefer different localizations in the block copolymer microdomains, depending on their coating composition. Nanoparticles with a PS-rich coating mixture (PS/P2VP

70/30) shown in Fig. 6.8a show a selective localization in the interface of the P2VP- and PS microdomains. Nanoparticles with a higher P2VP-content (PS/P2VP 30/70 and 50/50) are localized almost in the center of the P2VP-microdomain. Since the P2VP-microdomain is of comparable size, this position would still allow to segregate the PS-chains of the polymer shell to the interface to the PS-microdomains. For reference, we also investigated the localization of nanoparticles coated with pure PS or P2VP homopolymer. As expected, they selectively localize in the PS- and P2VP-microdomains, respectively, as shown in Fig. 6.8d and e.
Fig. 6.8f shows a cross-section of the polymer membrane near the surface. We observe a slight enrichment of nanoparticles at the surface of the membrane likely due to a steric repulsion of the solvent-swollen polymer coating from the narrow pores in the top layer, whose lengths can be estimated from the TEM-image to by ca. 200 nm, after which they merge with the supporting sponge-like polymer network. The localization of nanoparticles on the surface of the membranes can in certain cases also be imaged by AFM as shown in Fig. 6.9. A similar segregation of nanoparticles form block copolymer domains has recently been reported by Kim et al.[141].

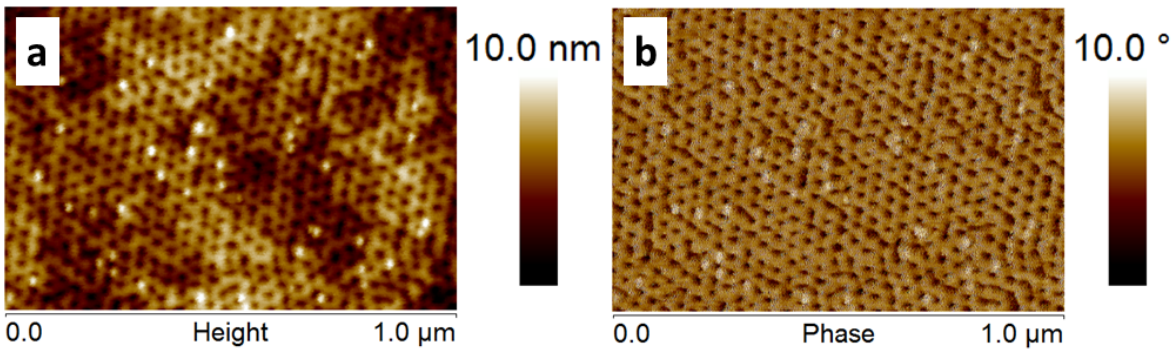

Figure 6.9. AFM height (a) and phase (b) image of a porous PS-P2VP membrane surface. The bright, round objects represent the nanoparticles, which were transported from the pore channels to the surface

6.5 Conclusions

Ironoxide nanoparticles coated with a mixed PS/P2VP-shell were successfully incorporated into PS-P2VP block copolymer membranes using the phase inversion method. DLS measurements showed the P2VP-chains to form a train-like conformation when adsorbed to the nanoparticle surface. Nanoparticle polymer hybrid membranes containing the mixed polymer-

coated nanoparticles at 0.5 and 1 wt% were characterized with electron- and atomic force microscopy. We find the nanoparticles to localize close or at the block copolymer microdomain interface. Thereby they affect the kinetic stability of the desired nanoporous top layer structure which develops during solvent evaporation. Amounts of only 0.5 wt% lead to a very early pore formation already after 2 seconds. At a concentration of 1 wt% the kinetic stability of the nanopore structure was enhanced to more than 20 seconds. Thus the addition of selectively functionalized nanoparticles not only stabilizes the desired pore structure, but also provides additional functionality as in the case of superparamagnetic nanoparticles for separation purposes.

Acknowledgement

We thank the EU (Project #228652, SELFMEM) and the German Science Foundation (SFB 840-TP B9, C.S.) for financial support as well as Markus Hund for help with the AFM-measurements.

6.6 Supporting Information

TEM image the FeO_x nanoparticles before ligand exchange. The nanoparticles are stabilized with oleic acid.

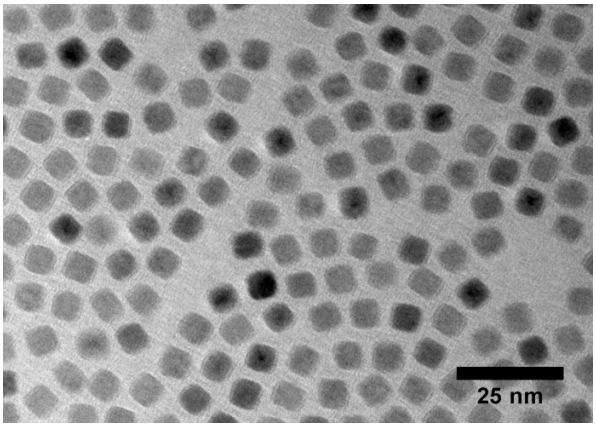

Figure S1. TEM image of the cubic FeO_x nanoparticles obtained with a Zeiss EM922 Omega.

Thermogravimetric Analysis

To further analyze the binding behavior of the vinylpyridine-ligands, TGA measurements of P2VP coated ironoxide nanoparticles were carried out to determine the polymer content of the sample.

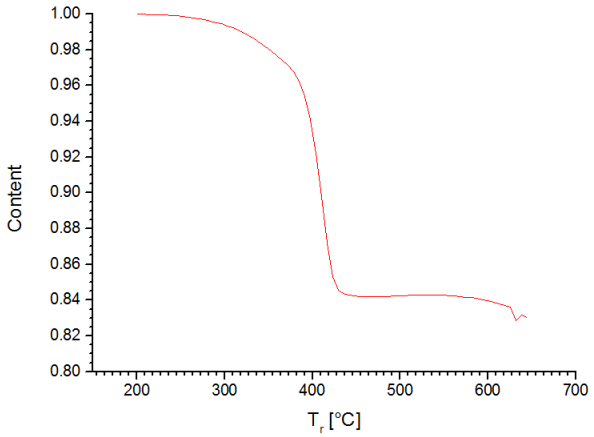

Figure S2. Overview of the loss of mass of the nanocomposite particles upon heating above the decomposition temperature obtained by TGA.

Figure S2 shows, that only 15 wt% of the total mass decomposes when the temperature of the sample is increased to over $600\,^{\circ}C$. These findings reveal an unusually high inorganic content of the nanocomposites with approx. 85 wt%, which is not expected for a "brush-like" polymer-coating on the nanoparticle.

Ligand exchange with unfunctionalized P2VP-1

Since poly-2-vinylpyridine has another binding site in the polymer repeating unit, it is important to determine the actual binding group to the metaloxide surface which can be the amino endgroup and/or the pyridine's nitrogen atom. Unfunctionalized P2VP-homopolymer used for a comparable ligand exchange reaction clearly yielded a much smaller amount of nanocomposites with a high fraction of unexchanged nanoparticles as becomes evident from figure S3. At the addition of precipitation solvent, a dark solid appears indicating a partly successful ligand exchange. The solution however stays dark even after addition of more diethyl ether proving, that a high amount of nanoparticles did not react with the unfunctionalized P2VP.

Figure S3. Photograph of the negative control after precipitation with diethyl ether.

Thus it is safe to assume that the multivalent amino endgroup is neccessary for a quantitative binding to the ironoxide surface. However, the pyridine side groups also bind to the surface but merely support the stability of the bonding. This type of bonding can be described as "train-like". According to the HSAB principle Fe^{2+} is considered a hard Lewis acid to which both, the amino endgroup and the pyridine side groups, both considered hard Lewis bases,

bond. If the hard acid Fe^{2+} is replaced by a soft acid, like Cd^{2+}, the binding should be energetically different because the overlap of the electron orbitals is not optimal for hard and soft reactants. To prove this, a pair of ligand exchanges was carried out using oleic acid stabilized cadmium selenide nanoparticles and P2VP homopolymer with and without a multivalent amino endgroup. Figure S4 shows photographs taken after precipitation with diethyl ether.

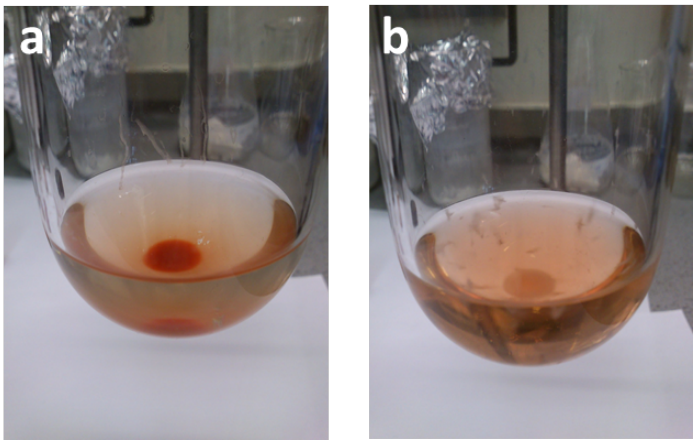

Figure S4. Photographs of (a) a successful precipitation of P2VP coated CdSe nanoparticles above a colorless precipitation solvent (diethyl ether) and (b) an unsuccessful ligand exchange of the same nanoparticles with unfunctionalized P2VP homopolymer.

Figure S4a shows successfully precipitated cadmium selenide nanoparticles coated with poly-2-vinylpyridine which, at the addition of diethyl ether, become insoluble. The addition of precipitation solvent to the negative control (figure S4b) merely causes the precipitation of P2VP but the red nanoparticles remain solved. Thus the hard Lewis bases on the pyridine side groups don't bind to the soft Lewis acid Cd^{2+} in the CdSe nanoparticles. Only the functional amino anchor group acts as a ligand, which is probably due to entropic effects since three molecules of oleic acid are set free upon bonding.

SEM images of pure membranes of PS-P2VP (without nanocomposite particles)

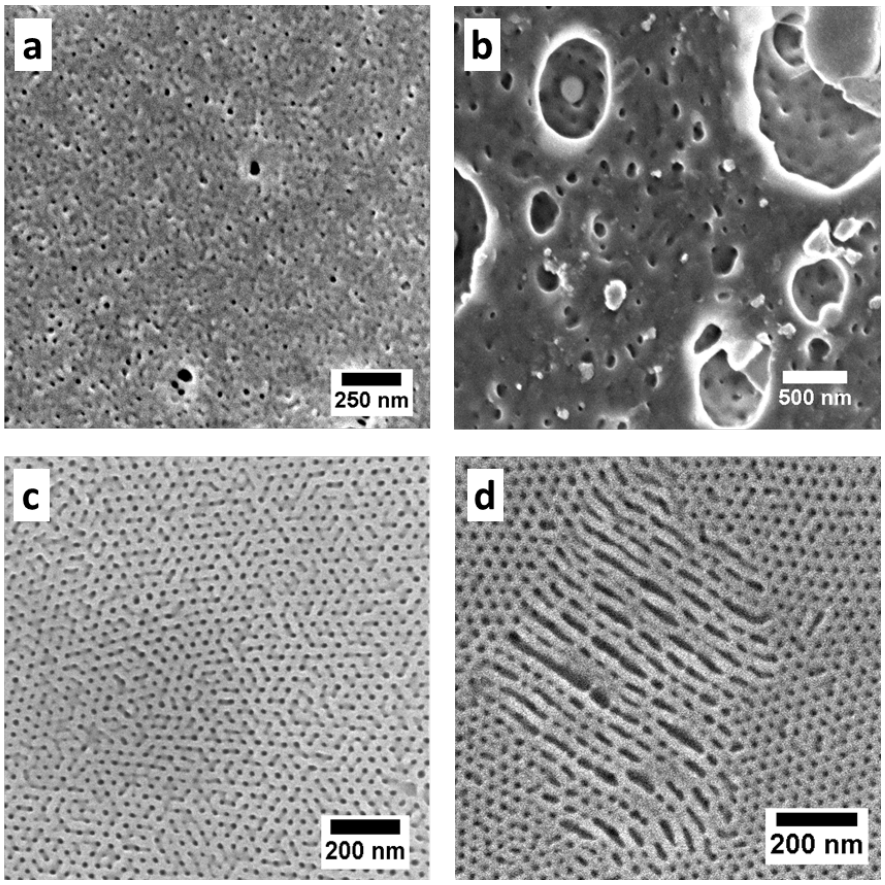

Figure S5. SEM images of membranes prepared from pure PS-P2VP. The films were cast from highly viscous solutions of 30 wt% PS-P2VP in DMF/THF : 40/60. The solvent evaporated for (a) 0 sec, (b) 10 sec and (c+d) 20 sec respectively.

Figure S5 shows, that the pore formation in solutions of 30 wt% pure block copolymer in DMF/THF : 40/60 occurs after 20 sec. Until approx. 10 sec (fig S5a and b) we observed a structure similar to the spinodal network explained in ref[93] which transforms into the porous network (fig. S5c). The porous structure already shows the first signs of matrix collapse and the distinct formation of cylinders in other spots (fig. S5d), leading to the assumption, that shortly after 20 sec only cylinders would have been observable.

Magnetic behavior of Nanocomposite Membranes

The prepared nanocomposite membranes show magnetic characteristics due to the particles close to the film surface.

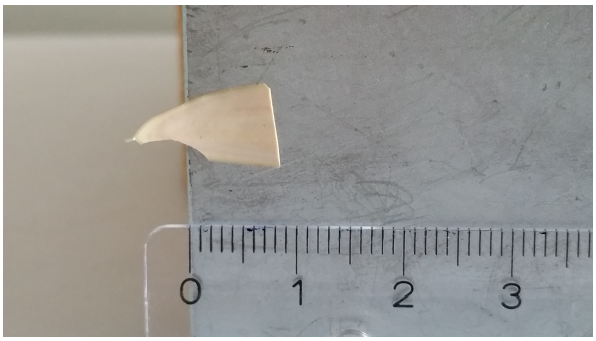

Figure S6. Photograph of a magnetic membrane.

Complete AFM series

The following three figures summarize the systematic study of the nanoparticle shell composition on the found surface morphology. The figures contain all images of the red, blue and green series mentioned in the discussions of figures 6.4 and 6.5.

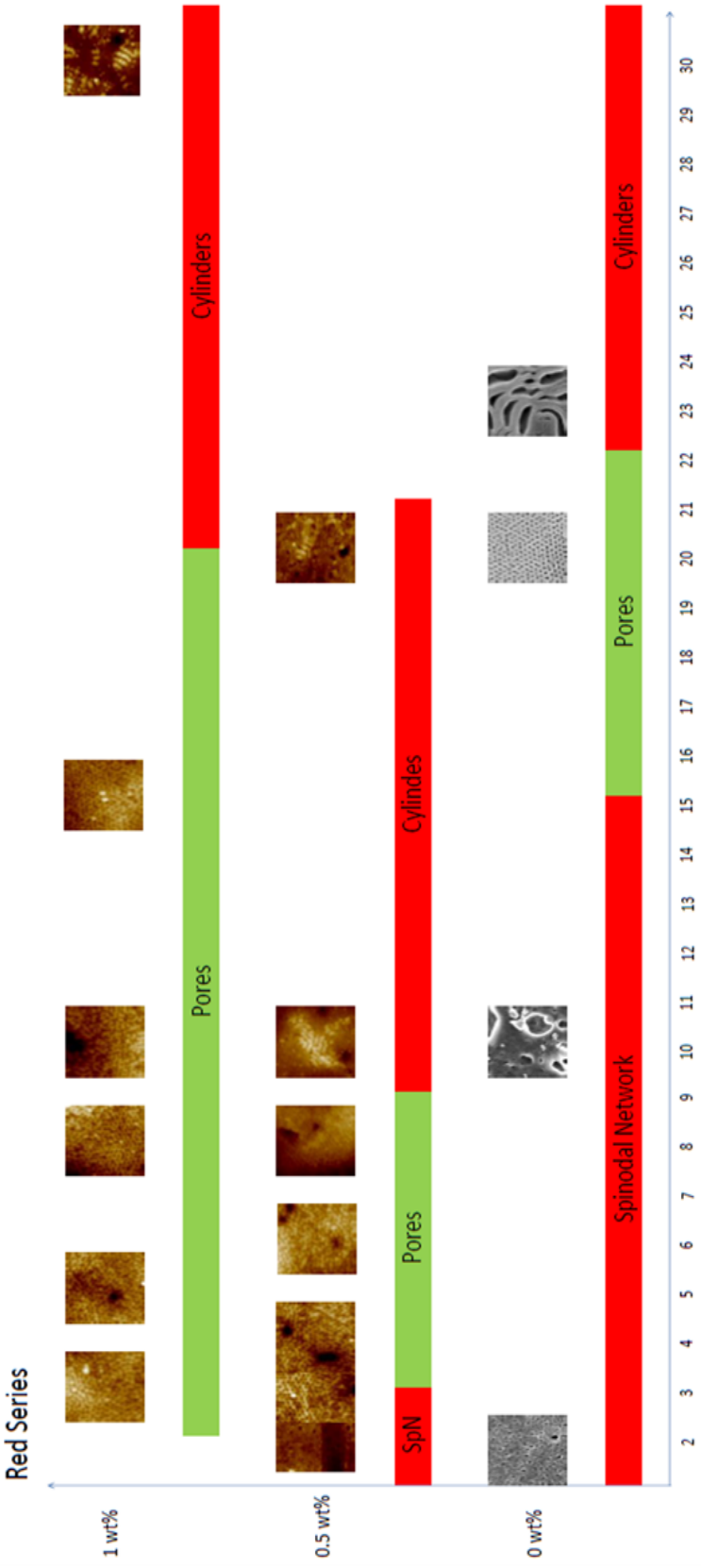
Red Series
1 wt%
0.5 wt%
0 wt%
Cylinders
Pores
Cylindes
Pores
SpN
Spinodal Network
Pores
Cylinders
2 3 4 5 6 7 8 9 10 11 12 13 14 15 16 17 18 19 20 21 22 23 24 25 26 27 28 29 30

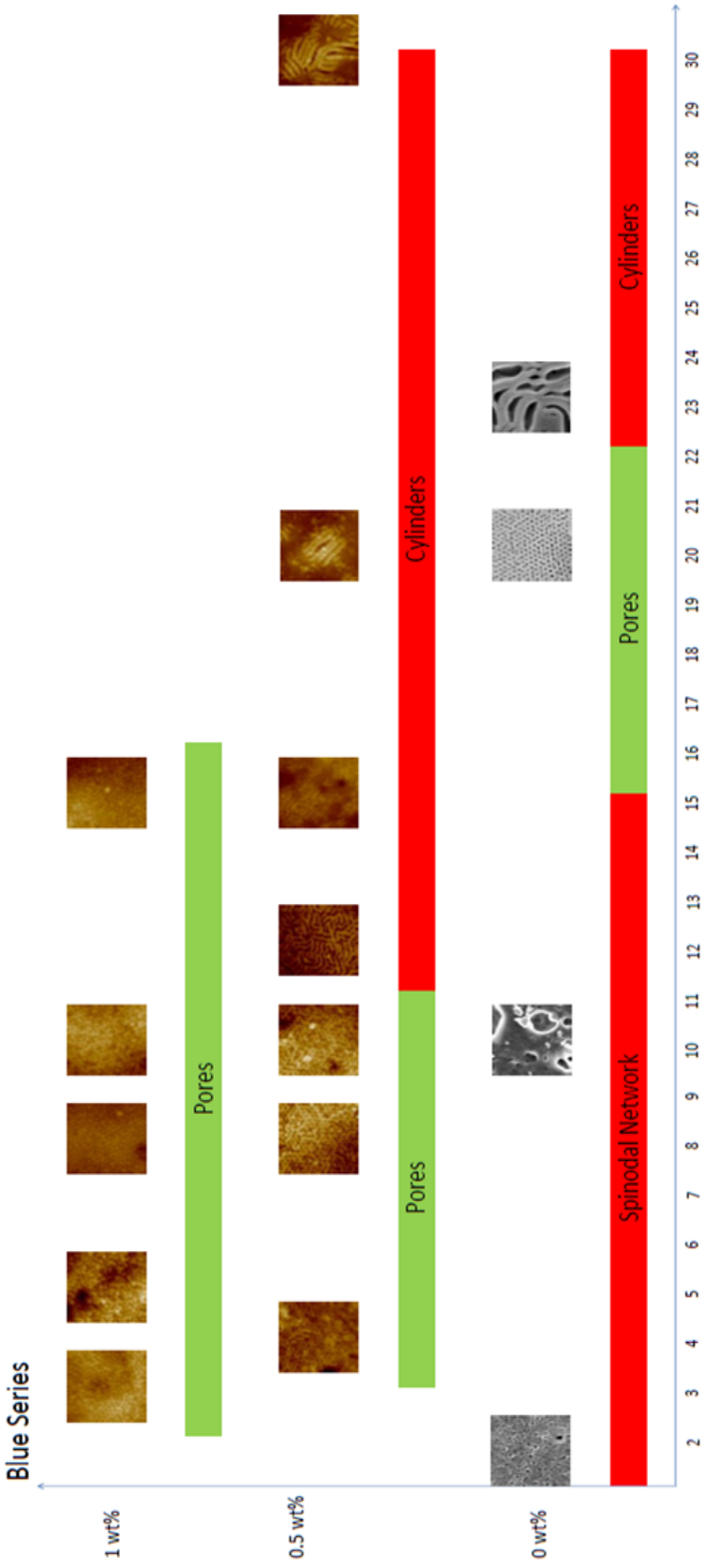
Blue Series
1 wt%
0.5 wt%
0 wt%
Pores
Cylinders
Pores
Spinodal Network
Pores
Cylinders
2
3
4
5
6
7
8
9
10
11
12
13
14
15
16
17
18
19
20
21
22
23
24
25
26
27
28
29
30

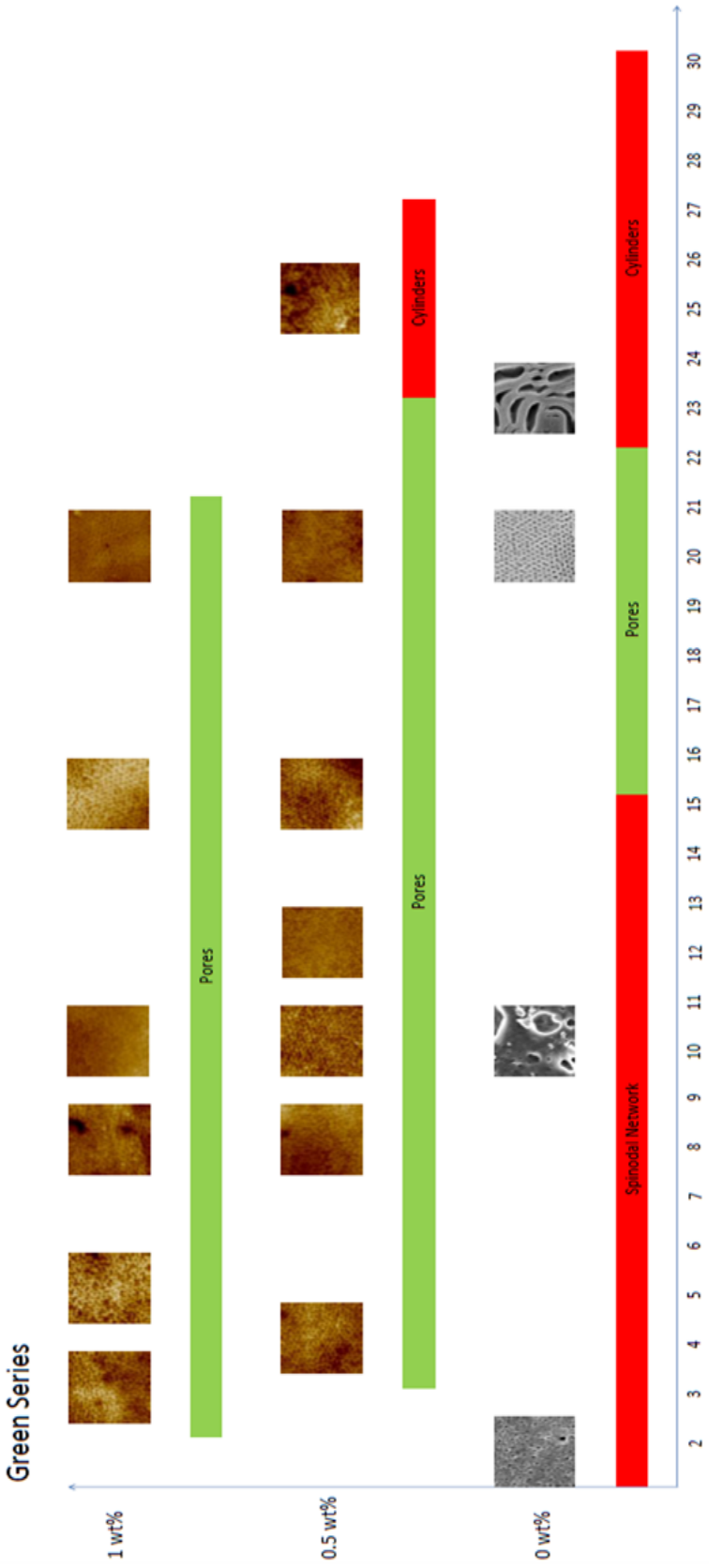
Green Series
1 wt%
0.5 wt%
0 wt%
Pores
Cylinders
Pores
Spinodal Network
Pores
Cylinders
2 3 4 5 6 7 8 9 10 11 12 13 14 15 16 17 18 19 20 21 22 23 24 25 26 27 28 29 30

Analytical data for the polymers P2VP-1, P2VP-2 and PS

GPC Elugram:

The elugrams of the three homopolymers used for Ligand exchange with FeO_x-Nanoparticles are shown in figure S7. The P2VP polymers (black and red line) were solved in *N,N*-dimethylformamide at concentration of 1 mg/mL. The solvent was purchased from AppliChem GmbH and used without further purification. The GPC measurement was conducted using a Degasys DG-2410 degasser in combination with a G1310A isocratic pump by Agilent keeping a constant solvent flow of 1 mL/min at $70\,^{\circ}C$ column temperature. The Pore sizes were 10^6 Å, 10^5 Å, 10^3 Å, and 10^2 Årespectively. The polymers were detected by the change of refractive index in the eluted solutions. Toluene was used as an internal standard together with a P2VP-calibration using 10 well defined polymer standards purchased by PSS Polymer Standards Service GmbH. Data evaluation was conducted using the Chromatographica V1.0.28 software.

PS was solved in tetrahydrofuran purchased from AppliChem without further purification. It was degassed with a Gastorr BG-12 degasser and kept at a constant flow of 1 mL/min using an Intelligent pump AI 301 by FLOM. The columns with decreasing pore sizes of 10^6 Å, 10^5 Å, 10^3 Å, and 10^2 Åwere kept at room temperature. The eluted solutions were analyzed using an UV1000 detector by Spectra Systems and a RI2000 refractive index detector by Schambeck SFD GmbH. Data evaluation was conducted using toluene as internal standard and a PS calibration consisting of 10 well defined PS standards purchased by PSS Polymer Standards Service GmbH together with the Chromatographica V1.0.28 software.

All GPC results are summarized in table S1.

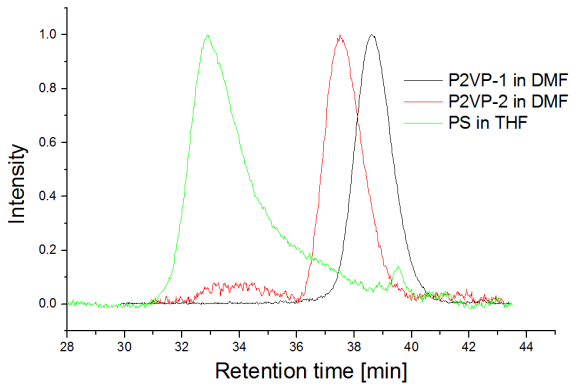

Figure S7. GPC chromatograms of the synthesized polymer ligands.

Table S1. Analytical data for the used polymers obtained by GPC.

Polymer	M_n [g/mol]	M_w [g/mol]	M_w/M_n
P2VP-1	2330	2477	1.06
P2VP-2	3588	3825	1.07
PS	9096	10120	1.11
PS-P2VP	100000		1.01

NMR spactra

All following NMR spectra were measured in deuterated chloroform at a concentration of approx. 10 mg/mL with a Bruker Ultrashield 300 NMR at 300 MHz. Calibration was done using the solvent signal at 7.26 ppm.

PS-PEHA:

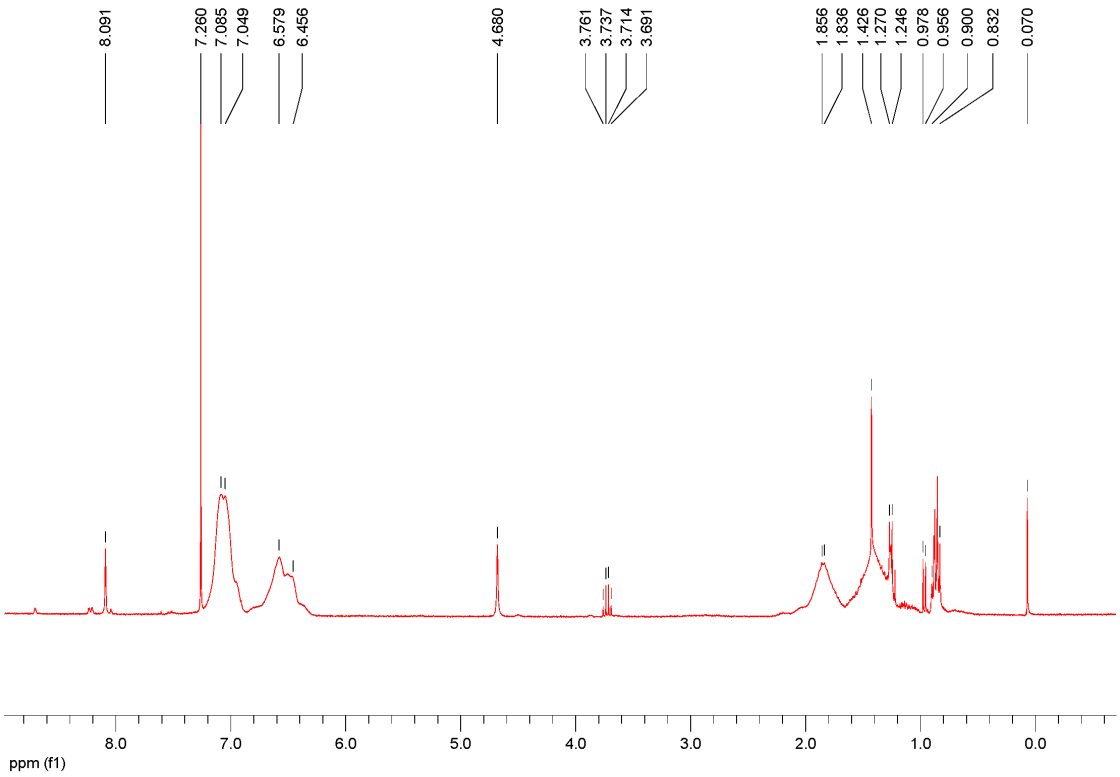

P2VP-1-PEHA:

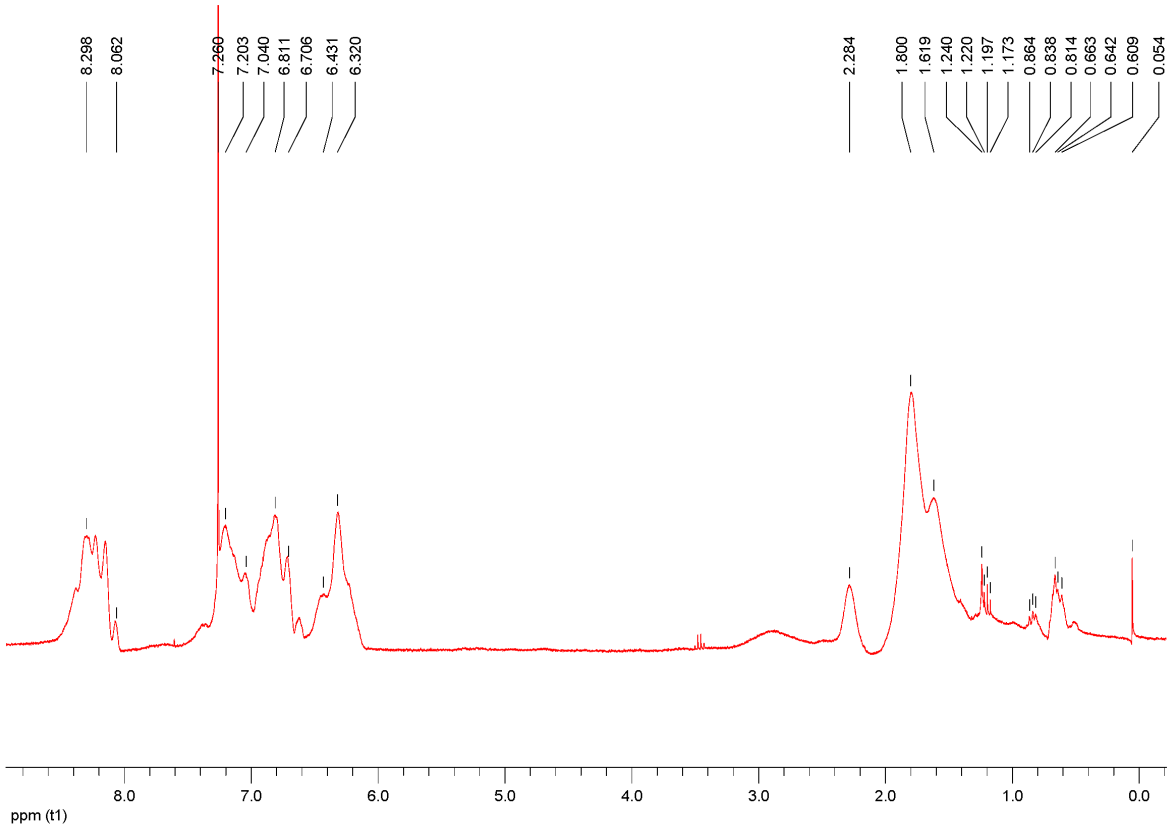
8.298
8.062
7.260
7.203
7.040
6.811
6.706
6.431
6.320
2.284
1.800
1.619
1.240
1.220
1.197
1.173
0.864
0.838
0.814
0.663
0.642
0.609
0.054
8.0
7.0
6.0
5.0
4.0
3.0
2.0
1.0
0.0
ppm (t1)

P2VP-2-PEHA:

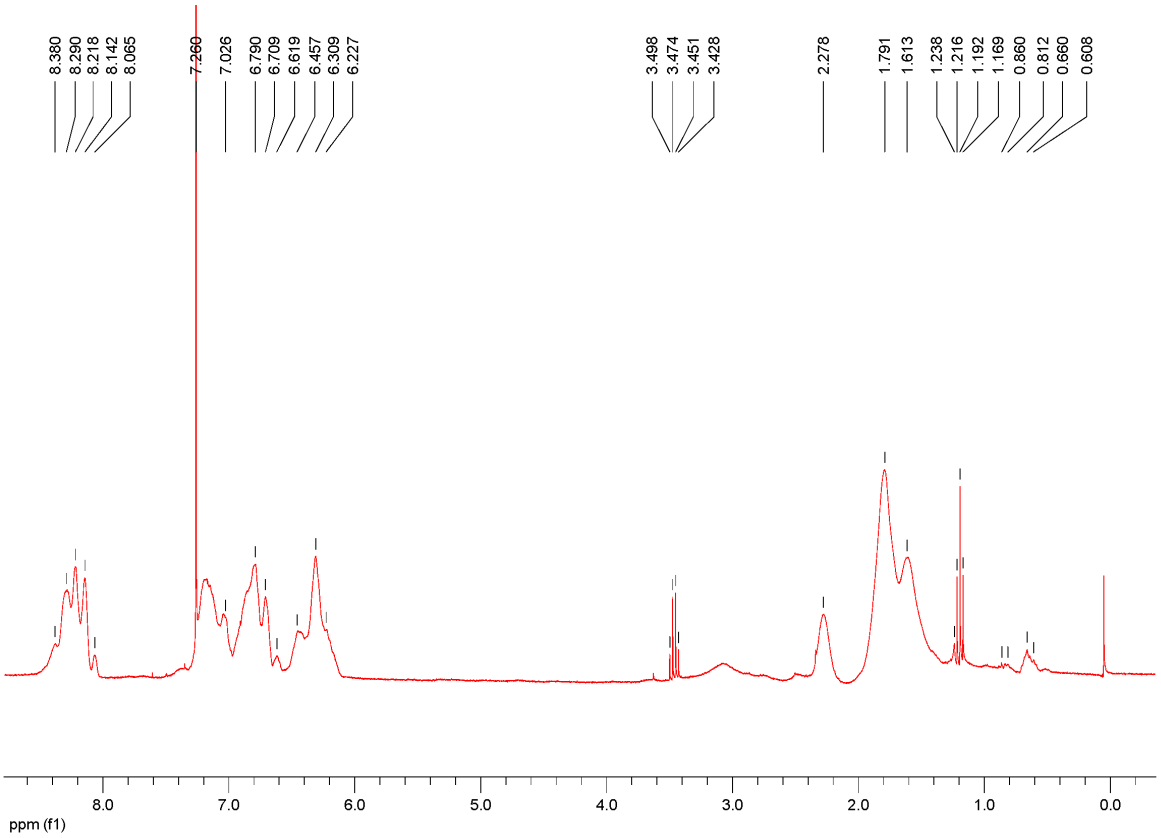
8.380
8.290
8.218
8.142
8.065
7.260
7.026
6.790
6.709
6.619
6.457
6.309
6.227
3.498
3.474
3.451
3.428
2.278
1.791
1.613
1.238
1.216
1.192
1.169
0.860
0.812
0.660
0.608
8.0
7.0
6.0
5.0
4.0
3.0
2.0
1.0
0.0
ppm (f1)

Bibliography

[1] C. Fong, T. Le, C. J. Drummond, *Chem. Soc. Rev.* **2012**, *41*, 1297–1322.

[2] L. Zhang, A. Eisenberg, *Science* **1995**, *268*, 1728–1731.

[3] J. C. M. van Hest, D. A. P. Delnoye, M. W. P. L. Baars, M. H. P. van Genderen, E. W. Meijer, *Science* **1995**, *268*, 1592–1595.

[4] G. Riess, *Prog. Polym. Sci.* **2003**, *28*, 1107–1170.

[5] F. S. Bates, *Science* **1991**, *251*, 898–905.

[6] F. S. Bates, G. H. Fredrickson, *Physics Today* **1999**, *52*, 32–38.

[7] B. Tieke, *Makromolekulare Chemie - eine Einführung*, Wiley-VCH, **2014**.

[8] S. Förster, T. Plantenberg, *Angew. Chem. Int. Ed.* **2002**, *41*, 688–714.

[9] F. S. Bates, G. H. Fredrickson, *Annu. Rev. Phys. Chem.* **1990**, *41*, 525–557.

[10] M. Szwarc, M. Levy, R. Milkovich, *J. Am. Chem. Soc.* **1956**, *78*, 2656–2657.

[11] T. P. Lodge, *Macromol. Chem. Phys.* **2003**, *204*, 265–273.

[12] S. Förster, M. Antonietti, *Adv. Mater.* **1998**, *10*, 195–217.

[13] Y. Mai, A. Eisenberg, *Chem. Soc. Rev.* **2012**, *41*, 5969–5985.

[14] D. E. Discher, F. Ahmed, *Annu. Rev. Biomed. Eng.* **2006**, *8*, 323–341.

[15] M. W. Matsen, M. Schick, *Phys. Rev. Lett.* **1994**, *72*, 2660–2663.

[16] M. W. Matsen, F. S. Bates, *Macromolecules* **1996**, *29*, 1091–1098.

[17] A. K. Khandpur, S. Förster, F. S. Bates, I. W. Hamley, A. J. Ryan, W. Bras, K. Almdal, K. Mortensen, *Macromolecules* **1995**, *28*, 8796–8806.

[18] P. J. Flory, *J. Chem. Phys.* **1942**, *10*, 51–61.

[19] M. L. Huggins, *J. Chem. Phys.* **1941**, *9*, 440–440.

[20] L. Leibler, *Macromolecules* **1980**, *13*, 1602–1617.

[21] A. N. Semenov, *Sov. Phys. JETP* **1985**, *61*, 733–742.

[22] K.-V. Peinemann, V. Abetz, P. F. W. Simon, *Nat. Mater.* **2007**, *6*, 992–996.

[23] F. Schacher, T. Rudolph, F. Wieberger, M. Ulbricht, A. H. E. Müller, *ACS Appl. Mater. Interfaces* **2009**, *1*, 1492–1503.

[24] W. A. Phillip, B. O'Neill, M. Rodwogin, M. A. Hillmyer, E. L. Cussler, *ACS Appl. Mater. Interfaces* **2010**, *2*, 847–853.

[25] A. Jung, S. Rangou, C. Abetz, V. Filiz, V. Abetz, *Macromol. Mater. Eng.* **2012**, *297*, 1–9.

[26] S. P. Nunes, R. Sougrat, B. Hooghan, D. H. Anjum, A. R. Behzad, L. Zhao, N. Pradeep, I. Pinnau, U. Vainio, K.-V. Peinemann, *Macromolecules* **2010**, *43*, 8079–8085.

[27] S. P. Nunes, A. R. Behzad, B. Hooghan, R. Sougrat, M. Karunakaran, N. Pradeep, U. Vainio, K.-V. Peinemann, *ACS Nano* **2011**, *5*, 3516–3522.

[28] M. Gallei, S. Rangou, V. Filiz, K. Buhr, S. Bolmer, C. Abetz, V. Abetz, *Macromol. Chem. Phys.* **2013**, *214*, 1037–1046.

[29] A. Jung, V. Filiz, S. Rangou, K. Buhr, P. Merten, J. Hahn, J. Clodt, C. Abetz, V. Abetz, *Macromol. Rapid Commun.* **2013**, *34*, 610–615.

[30] H. Strathmann, *Introduction to Membrane Science and Technology*, Wiley-VCH, **2011**.

[31] L. Breitbach, E. Hinke, E. Staude, *Die Angewandte Makromolekulare Chemie* **1991**, *184*, 183–196.

[32] B. Van der Bruggen, *J. Appl. Polym. Sci.* **2009**, *114*, 630–642.

[33] N. Nady, M. C. Franssen, H. Zuilhof, M. S. Mohy Eldin, R. Boom, K. Schroën, *Desalination* **2011**, *275*, 1–9.

[34] D. Grosso, F. Babonneau, P.-A. Albouy, H. Amenitsch, A. R. Balkenende, A. Brunet-Bruneau, , J. Rivory, *Chem. Mater.* **2002**, *14*, 931–939.

[35] D. Grosso, F. Babonneau, G. J. de A. A. Soler-Illia, P.-A. Albouy, H. Amenitsch, *Chem. Commun.* **2002**, 748–749.

[36] F. Cagnol, D. Grosso, G. J. A. A. Soler-Illia, E. L. Crepaldi, F. Babonneau, H. Amenitsch, C. Sanchez, *J. Mater. Chem.* **2003**, *13*, 61–66.

[37] D. Grosso, A. R. Balkenende, P. A. Albouy, A. Ayral, H. Amenitsch, F. Babonneau, *Chem. Mater.* **2001**, *13*, 1848–1856.

[38] D. Grosso, F. Cagnol, G. J. de A. A. Soler-Illia, E. L. Crepaldi, H. Amenitsch, A. Brunet-Bruneau, A. Bourgeois, C. Sanchez, *Adv. Funct. Mater.* **2004**, *14*, 309–322.

[39] B. Smarsly, D. Grosso, T. Brezesinski, N. Pinna, C. Boissiere, M. Antonietti, C. Sanchez, *Chem. Mater.* **2004**, *16*, 2948–2952.

[40] B. Lee, J. Yoon, W. Oh, Y. Hwang, K. Heo, K. S. Jin, J. Kim, K.-W. Kim, M. Ree, *Macromolecules* **2005**, *38*, 3395–3405.

[41] S. Hu, J. Rieger, Y. Lai, S. V. Roth, R. Gehrke, , Y. Men, *Macromolecules* **2008**, *41*, 5073–5076.

[42] S. Hu, J. Rieger, Z. Yi, J. Zhang, X. Chen, S. V. Roth, R. Gehrke, Y. Men, *Langmuir* **2010**, *26*, 13216–13220.

[43] Y. Men, J. Rieger, S. V. Roth, R. Gehrke, X. Kong, *Langmuir* **2006**, *22*, 8285–8288.

[44] C. M. Papadakis, Z. Di, D. Posselt, D.-M. Smilgies, *Langmuir* **2008**, *24*, 13815–13818, pMID: 19053660.

[45] Z. Di, D. Posselt, D.-M. Smilgies, C. M. Papadakis, *Macromolecules* **2010**, *43*, 418–427.

[46] Z. Di, D. Posselt, D.-M. Smilgies, R. Li, M. Rauscher, I. I. Potemkin, C. M. Papadakis, *Macromolecules* **2012**, *45*, 5185–5195.

[47] M. Y. Paik, J. K. Bosworth, D.-M. Smilges, E. L. Schwartz, X. Andre, C. K. Ober, *Macromolecules* **2010**, *43*, 4253–4260, pMID: 21116459.

[48] X. Gu, I. Gunkel, A. Hexemer, W. Gu, T. P. Russell, *Advanced Materials* **2014**, *26*, 273–281.

[49] Y. Rho, C. Kim, T. Higashihara, S. Jin, J. Jung, T. J. Shin, A. Hirao, M. Ree, *ACS Macro Lett.* **2013**, *2*, 849–855.

[50] M. Al-Hussein, M. Schindler, M. A. Ruderer, J. Perlich, M. Schwartzkopf, G. Herzog, B. Heidmann, A. Buffet, S. V. Roth, P. Müller-Buschbaum, *Langmuir* **2013**, *29*, 2490–2497.

[51] G. Herzog, G. Benecke, A. Buffet, B. Heidmann, J. Perlich, J. F. H. Risch, G. Santoro, M. Schwartzkopf, S. Yu, W. Wurth, S. V. Roth, *Langmuir* **2013**, *29*, 11260–11266.

[52] D. Sen, O. Spalla, O. Taché, P. Haltebourg, A. Thill, *Langmuir* **2007**, *23*, 4296–4302.

[53] I. Shyjumon, M. Rappolt, B. Sartori, H. Amenitsch, P. Laggner, *Rev. Sci. Instrum.* **2008**, *79*, 043905.

[54] J. Schuster, R. Koehn, M. Doeblinger, A. Keilbach, H. Amenitsch, T. Bein, *J. Am. Chem. Soc.* **2012**, *134*, 11136–11145.

[55] A. P. Alivisatos, *J. Phys. Chem.* **1996**, *100*, 13226–13239.

[56] H. Weller, *Angew. Chem. Int. Ed. Engl.* **1993**, *32*, 41–53.

[57] S. Kango, S. Kalia, A. Celli, J. Njuguna, Y. Habibi, R. Kumar, *Prog. Polym. Sci.* **2013**, *38*, 1232–1261.

[58] F. Lüdersdorff, *Verhandlungen Verein. Beförderung Gewerbefleiss. Preussen* **1833**, *12*, 224.

[59] H. M. Chen, R.-S. Liu, *J. Phys. Chem. C* **2011**, *115*, 3513–3527.

[60] E. P. Plueddemann, H. A. Clark, L. E. Nelson, K. R. Hoffman, *Mod Plast* **1962**, *39*, 135.

[61] E. P. Plueddemann, *J. Adhes.* **1970**, *2*, 184–201.

[62] J. Zhao, M. Milanova, M. M. Warmoeskerken, V. Dutschk, *Colloid. Surface. A* **2012**, *413*, 273–279.

[63] P. Mansky, Y. Liu, E. Huang, T. P. Russell, C. Hawker, *Science* **1997**, *275*, 1458–1460.

[64] J. Park, K. An, Y. Hwang, J.-G. Park, H.-J. Noh, J.-Y. Kim, J.-H. Park, N.-M. Hwang, T. Hyeon, *Nat. Mater.* **2004**, *3*, 891–895.

[65] S. Ehlert, T. Lunkenbein, J. Breu, S. Förster, *Colloid. Surface. A* **2014**, *444*, 76–80.

[66] D. Celik, M. Krueger, C. Veit, H. F. Schleiermacher, B. Zimmermann, S. Allard, I. Dumsch, U. Scherf, F. Rauscher, P. Niyamakom, *Sol. Energ. Mat. Sol. C.* **2012**, *98*, 433–440.

[67] C. Brinker, G. Scherer, *Sol-gel science: physics and chemistry of sol-gel science processing, inorganic*, Academic Press, Toronto, **1990**.

[68] G.-H. Hsiue, W.-J. Kuo, Y.-P. Huang, R.-J. Jeng, *Polymer* **2000**, *41*, 2813–2825.

[69] J. V. Crivello, K. Y. Song, R. Ghoshal, *Chem. Mater.* **2001**, *13*, 1932–1942.

[70] E. J. A. Pope, M. Asami, J. D. Mackenzie, *J. Mater. Res.* **1989**, *4*, 1018–1026.

[71] P. Hajji, L. David, J. F. Gerard, J. P. Pascault, G. Vigier, *J Polym Sci, Part B: Polym Phys* **1999**, *37*, 3172–3187.

[72] Y. Ou, F. Yang, Z.-Z. Yu, *J Polym Sci, Part B: Polym Phys* **1998**, *36*, 789–795.

[73] S. Wang, S. Yang, C. Yang, Z. Li, J. Wang, W. Ge, *J. Phys. Chem. B* **2000**, *104*, 11853–11858.

[74] Y. Nakao, *J. Chem. Soc., Chem. Commun.* **1993**, 826–828.

[75] W. E. van Zyl, M. Garcia, B. A. G. Schrauwen, B. J. Kooi, J. T. M. De Hosson, H. Verweij, *Macromol. Mater. Eng.* **2002**, *287*, 106–110.

[76] H. Zhao, R. K. Li, *Polymer* **2006**, *47*, 3207–3217.

[77] N. Erdem, A. A. Cireli, U. H. Erdogan, *J. Appl. Polym. Sci.* **2009**, *111*, 2085–2091.

[78] A. K. Boal, F. Ilhan, J. E. DeRouchey, T. Thurn-Albrecht, T. P. Russell, V. M. Rotello, *Nature* **2000**, *404*, 746–748.

[79] S.-W. Yeh, K.-H. Wei, Y.-S. Sun, U.-S. Jeng, K. S. Liang, *Macromolecules* **2003**, *36*, 7903–7907.

[80] A. Noro, K. Higuchi, Y. Sageshima, Y. Matsushita, *Macromolecules* **2012**, *45*, 8013–8020.

[81] B. J. Kim, J. Bang, C. J. Hawker, E. J. Kramer, *Macromolecules* **2006**, *39*, 4108–4114.

[82] T. Lunkenbein, M. Kamperman, Z. Li, C. Bojer, M. Drechsler, S. Förster, U. Wiesner, A. H. E. Müller, J. Breu, *J. Am. Chem. Soc.* **2012**, *134*, 12685–12692.

[83] U. Borchert, Dissertation, University of Hamburg, **2006**.

[84] M. Misner, H. Skaff, T. Emrick, T. Russell, *Adv. Mater.* **2003**, *15*, 221–224.

[85] T. Thurn-Albrecht, J. Schotter, G. A. Kästle, N. Emley, T. Shibauchi, L. Krusin-Elbaum, K. Guarini, C. T. Black, M. T. Tuominen, T. P. Russell, *Science* **2000**, *290*, 2126–2129.

[86] Y. Boontongkong, R. E. Cohen, *Macromolecules* **2002**, *35*, 3647–3652.

[87] P. Madhavan, P.-Y. Hong, R. Sougrat, S. P. Nunes, *ACS Appl. Mater. Interfaces* **2014**, *6*, 18497–18501.

[88] R. B. Thompson, V. V. Ginzburg, M. W. Matsen, A. C. Balazs, *Science* **2001**, *292*, 2469–2472.

[89] J. U. Kim, B. O'Shaughnessy, *Phys. Rev. Lett.* **2002**, *89*, 238301.

[90] K. Tsutsumi, Y. Funaki, Y. Hirokawa, T. Hashimoto, *Langmuir* **1999**, *15*, 5200–5203.

[91] S. Zou, R. Hong, T. Emrick, G. C. Walker, *Langmuir* **2007**, *23*, 1612–1614.

[92] Y. Lin, A. Böker, J. He, K. Sill, H. Xiang, C. Abetz, X. Li, J. Wang, T. Emrick, S. Long, Q. Wang, A. Balazs, T. P. Russell, *Nature* **2005**, *434*, 55–59.

[93] C. Stegelmeier, V. Filiz, V. Abetz, J. Perlich, A. Fery, P. Ruckdeschel, S. Rosenfeldt, S. Förster, *Macromolecules* **2014**, *47*, 5566–5577.

[94] S. Rangou, K. Buhr, V. Filiz, J. I. Clodt, B. Lademann, J. Hahn, A. Jung, V. Abetz, *J. Membr. Sci.* **2014**, *451*, 266–275.

[95] A. Jung, Dissertation, University of Hamburg, **2013**.

[96] J. Hahn, V. Filiz, S. Rangou, B. Lademann, K. Buhr, J. I. Clodt, A. Jung, C. Abetz, V. Abetz, *Macromol. Mater. Eng.* **2013**, *298*, 1315–1321.

[97] I. Podariu, Z. Shou, A. Chakrabarti, *Physical Review E* **2000**, *62*, 3059–3062.

[98] M. Antonietti, S. Heinz, M. Schmidt, C. Rosenauer, *Macromolecules* **1994**, *27*, 3276–3281.

[99] S. M. Taheri, S. Fischer, M. Trebbin, S. With, J. H. Schröder, J. Perlich, S. V. Roth, S. Förster, *Soft Matter* **2012**, *8*, 12124–12131.

[100] M. S. Nikolic, M. Krack, V. Aleksandrovic, A. Kornowski, S. Förster, H. Weller, *Angew. Chem. Int. Ed.* **2006**, *45*, 6577–6580.

[101] R. M. Dorin, D. S. Marques, H. Sai, U. Vainio, W. A. Phillip, K.-V. Peinemann, S. P. Nunes, U. Wiesner, *ACS Macro Lett.* **2012**, *1*, 614–617.

[102] D. S. Marques, R. M. Dorin, U. Wiesner, D.-M. Smilgies, A. R. Behzad, U. Vainio, K.-V. Peinemann, S. P. Nunes, *Polymer* **2014**, *55*, 1327–1332.

[103] W. A. Phillip, R. Mika Dorin, J. Werner, E. M. V. Hoek, U. Wiesner, M. Elimelech, *Nano Lett.* **2011**, *11*, 2892–2900.

[104] M. M. Pendergast, M. Dorin, W. A. Phillip, U. Wiesner, E. M. V. Hoek, *J. Membr. Sci.* **2013**, *444*, 461–468.

[105] R. M. Dorin, H. Sai, U. Wiesner, *Chem. Mater.* **2014**, *26*, 339–347.

[106] R. M. Dorin, W. A. Phillip, H. Sai, J. Werner, M. Elimelech, U. Wiesner, *Polymer* **2014**, *55*, 347–353.

[107] J. Hahn, V. Filiz, S. Rangou, J. Clodt, A. Jung, K. Buhr, C. Abetz, V. Abetz, *J Polym Sci, Part B: Polym Phys* **2013**, *51*, 281–290.

[108] M. Radjabian, J. Koll, K. Buhr, U. A. Handge, V. Abetz, *Polymer* **2013**, *54*, 1803–1812.

[109] M. Radjabian, J. Koll, K. Buhr, U. Vainio, C. Abetz, U. A. Handge, V. Abetz, *Polymer* **2014**, *55*, 2986–2997.

[110] N. Hadjichristidis, S. Pispas, G. Floudas, *Block Copolymers: Synthetic Strategies, Physical Properties, and Applications*, Wiley, Hoboken NJ, **2003**.

[111] C. Stegelmeier, A. Exner, S. Hauschild, V. Filiz, V. Abetz, S. Förster, *Macromolecules* **2015**, *48*, 1524–1530.

[112] S. V. Roth, R. Döhrmann, M. Dommach, M. Kuhlmann, I. Kröger, R. Gehrke, H. Walter, C. Schroer, B. Lengeler, P. Müller-Buschbaum, *Rev. Sci. Instrum.* **2006**, *77*, 085106.

[113] M. W. Zemansky, *Heat and Thermodynamics*, 5th ed. Aufl., McGraw-Hill, **1968**.

[114] J. Brandrup, E. H. Immergut, E. A. Grulke, A. Abe, D. R. Bloch, *Polymer Handbook*, Wiley, New York, **1999**.

[115] C. Stegelmeier, Dissertation, University of Bayreuth, **2014**.

[116] C. Chatelain, T. Balois, P. Ciarletta, M. B. Amar, *New. J. Phys.* **2011**, *13*, 115013.

[117] H. Sai, K. W. Tan, K. Hur, E. Asenath-Smith, R. Hovden, Y. Jiang, M. Riccio, D. A. Muller, V. Elser, L. A. Estroff, S. M. Gruner, U. Wiesner, *Science* **2013**, *341*, 530–534.

[118] L. Oss-Ronen, J. Schmidt, V. Abetz, A. Radulescu, Y. Cohen, Y. Talmon, *Macromolecules* **2012**, *45*, 9631–9642.

[119] R. D. Peters, P. Stasiak, M. W. Matsen, K. Dalnoki-Veress, *ACS Macro Lett.* **2013**, *2*, 441–445.

[120] S. P. Nunes, M. Karunakaran, N. Pradeep, A. R. Behzad, B. Hooghan, R. Sougrat, H. He, K.-V. Peinemann, *Langmuir* **2011**, *27*, 10184–10190.

[121] D. S. Marques, U. Vainio, N. M. Chaparro, V. M. Calo, A. R. Bezahd, J. W. Pitera, K.-V. Peinemann, S. P. Nunes, *Soft Matter* **2013**, *9*, 5557–5564.

[122] P. Madhavan, K.-V. Peinemann, S. P. Nunes, *ACS Appl. Mater. Interfaces* **2013**, *5*, 7152–7159.

[123] J. I. Clodt, S. Rangou, A. Schröder, K. Buhr, J. Hahn, A. Jung, V. Filiz, V. Abetz, *Macromol. Rapid Commun.* **2013**, *34*, 190–194.

[124] S. H. Kim, M. J. Misner, T. Xu, M. Kimura, T. P. Russell, *Adv. Mater.* **2004**, *16*, 226–231.

[125] Y. F. Zhao, S. C. J. Loo, Y. Z. Chen, F. Y. C. Boey, J. J. Ma, *Biomed. Mater. Res.* **2008**, *85*, 1032–1042.

[126] A. Baruth, M. Seo, C. H. Lin, K. Walster, A. Shankar, M. A. Hillmyer, C. Leighton, *ACS Appl. Mater. Interfaces* **2014**, *6*, 13770–13781.

[127] S. Förster, M. Zisenis, E. Wenz, M. Antonietti, *J. Chem. Phys.* **1996**, *104*, 9956–9970.

[128] X. Qu, J. Brame, Q. Li., P. J. J. Alvarez, *Acc. Chem. Res.* **2013**, *46*, 834–846.

[129] A. F. Ismail, P. S. Goh, *Adv. Mater. Research* **2014**, *896*, 3–6.

[130] K. Yang, B. S. Xing, *Chem. Rev.* **2010**, *110*, 5989–6008.

[131] C. T. Yavuz, J. T. Mayo, W. W. Yu, A. Prakash, J. C. Falkner, S. Yean, L. L. Cong, H. J. Shipley, A. Kan, M. Tomson, D. Natelson, V. L. Colvin, *Science* **2006**, *314*, 964–967.

[132] Q. L. Li, S. Mahendra, D. Y. Lyon, L. Brunet, M. V. Liga, D. Li, P. J. J. Alvarez, *Water Res.* **2008**, *42*, 4591–4602.

[133] S. B. Hamouda, Q. T. Nguyen, D. Langevin, C. Chappey, S. Roudesli, *React. Funct. Polym.* **2007**, *67*, 893–904.

[134] M. M. Pendergast, E. M. V. Hoek, *Energy Environ. Sci.* **2011**, *4*, 1946–1971.

[135] J. J. Chiu, B. J. Kim, E. J. Kramer, D. J. Pine, *J. Am. Chem. Soc.* **2005**, *127*, 5036–5037.

[136] R. Liang, J. Xu, W. Li, Y. Liao, K. Wang, J. You, J. Zhu, W. Jiang, *Macromolecules* **2014**, *48*, 256–263.

[137] S. U. Pickering, *J. Chem. Soc.* **2001**, *91*, 1907.

[138] S. Ehlert, S. M. Taheri, D. Pirner, M. Drechsler, H.-W. Schmidt, S. Förster, *ACS Nano* **2014**, *8*, 6114–6122.

[139] J. Y. Lee, R. B. Thompson, D. Jasnow, A. C. Balazs, *Macromolecules* **2002**, *35*, 4855–4858.

[140] Y.-S. Sun, U.-S. Jeng, K. S. Liang, S.-W. Yeh, K.-H. Wei, *Polymer* **2006**, *47*, 1101–1107.

[141] B. Kim, J. Chiu, G.-R. Yi, D. Pine, E. Kramer, *Adv. Mater.* **2005**, *17*, 2618–2622.

List of Publications

Published:

- Corinna Stegelmeier, Volkan Filiz, Volker Abetz, Jan Perlich, Andreas Fery, Pia Ruckdeschel, Sabine Rosenfeldt, Stephan Förster
  "Topological Paths and Transient Morphologies during Formation of Mesoporous Block Copolymer Membranes"
  Macromolecules **2014**, *47*, 5566-5577.

- Corinna Stegelmeier, Alexander Exner, Stephan Hauschild, Volkan Filiz, Volker Abetz, Jan Perlich, Stephan V. Roth and Stephan Förster
  "Blockcopolymer membrane self-assembly studied by in-situ synchrotron-SAXS"
  Macromolecules **2015**, 48, 1524-1530.

Submitted:

- Sascha Ehlert, Corinna Stegelmeier, Daniela Pirner, Stephan Förster
  "A General Route to Optically Transparent Highly Filled Polymer Nanocomposites"
  Macromolecules **2015**.

Manuscript intended for submission:

- Corinna Stegelmeier, Sara Mehdizadeh Taheri, Sascha Ehlert, Katharina Ottermann, Andreas Fery and Stephan Förster
  "Functionalization and Stabilization of Self-Assembled Blockcopolymer Membranes by Nanoparticles".

Poster Presentations:

- C. Stegelmeier, A. Exner, J. Perlich, and S. Förster
  "Assembling wormlike micelles into mesoporous membranes"
  Conference of the European Colloid and Interface Society ECIS 2011, Berlin, Germany.

- C. Stegelmeier, A. Exner, J. Perlich, and S. Förster
  "Assembling wormlike micelles into mesoporous membranes"
  World Filtration Congress (WFC) 2012, Graz, Austria.

Danksagung

Zu allererst gilt mein Dank meinem Doktorvater Prof. Stephan Förster, für die interessante Themenstellung sowie die intensive Betreuung während der letzten Jahre angefangen mit meiner Diplomarbeit an der Universität Hamburg. Ich bedanke mich für die wissenschaftlichen Freiheiten, die er mir gelassen hat aber auch für jede gute und aufschlussreiche Diskussion und jeden Ratschlag, der letztendlich zum Gelingen dieser Arbeit beigetragen hat.
Herrn Prof. Hans-Werner Schmidt danke ich für die Begutachtung dieser Arbeit.

Meinen Laborkollegen Nonio Wolter, Tobias Güttler, Daniela Pirner und Maria Ritter danke ich für viele interessante Gespräche und die gute Zusammenarbeit bei Polymerisationen oder bei der GPC- und NMR-Analytik.
Für eine besonders gute Zusammenarbeit auf Messzeiten gilt mein Dank Alexander Exner, Stephan Hauschild und Jan Perlich aber auch für die freundliche Unterstützung bei der Datenauswertung Sabine Rosenfeldt und Martin Dulle.
Bei Adina Jung und Volkan Filiz möchte ich mich für die gute Zusammenarbeit im Rahmen des SELFMEM-Projektes und die schöne Zeit auf Projekt-Meetings bedanken.
Sara Mehdizadeh Taheri und Sascha Ehlert danke ich für die Unterstützung und die vielen praktischen Ratschläge im Labor bei der Präparation der Nanocomposite.
Des Weiteren möchte ich meinen Praktikanten Sabrina Sachau, Pia Ruckdeschel, Stephanie Schindler und Katharina Ottermann sowie sämtlichen Mitarbeiter-Praktikanten für ihre unerschöpfliche Mitarbeit danken, ohne die diese Arbeit nicht möglich gewesen wäre.
Für die freundliche Hilfe und konstruktive Unterstützung bei SEM-, TEM- und AFM-Messungen und Probenpräparation danke ich Beate Förster, Martina Heider, Markus Drechsler, Carmen Kunert und Markus Hund.
Carolin Fürst, Sascha Ehlert, Adina Jung, Marina Stegelmeier und Michaela Meyns danke ich für das Korrekturlesen dieser Arbeit.

Bei Elisabeth Düngfelder und Jenniffer Hennessy bedanke ich mich für die Erledigung aller organisatorischen Angelegenheiten sowie für viele nette Gespräche.
Für die stetige Hilfsbereitschaft im Labor, das herzliche Willkommen in Bayreuth und für die vielen Geschichten über die fränkische Kultur möchte ich mich herzlich bei Karlheinz Lauterbach bedanken, der unsere ganze Gruppe offen an der Universität Bayreuth aufgenommen

hat.
All meinen Frängisch-Lehrern über die Jahre möchte ich dafür danken, dass sie mir geholfen haben die Hamburg-Bayreuth-Sprachbarriere zu überwinden und dabei meinen linguistischen Sprachhorizont zu erweitern.
Dem gesamten PC1-Lehrstuhl danke ich für eine unvergessliche Zeit. Es herrschte stets eine extrem angenehme Atmosphäre, insbesondere bei Grillfesten, Kanutour oder Kickerturnieren, was mir von Anfang bis Ende meine Zeit in Bayreuth verschönert hat. Danke dafür!

Als letztes danke ich meiner Familie sowie allen Freunden und Komilitonen aus der Heimat für ihre moralische Unterstützung.

Hiermit erkläre ich, dass keine Tatsachen vorliegen, die mich nach den gesetzlichen Bestimmungen über die Führung akademischer Grade zur Führung eines Doktorgrades unwürdig erscheinen lassen.

Hiermit erkläre ich mich einversanden, dass die elektronische Fassung meiner Dissertation unter Wahrung meiner Urheberrechte und des Datenschutzes einer gesonderen Überprüfung hinsichtlich der eigenständigen Anfertigung der Dissertation unterzogen werden kann.

Hiermit erkläre ich eidesstattlich, dass ich die Dissertation selbstständig verfasst und keie anderen anl die von mir angegebenen Quellen und Hilfsmittel benutzt habe.

Ich habe die Dissertation nicht bereits zur Erlangung eines akademischen Grades anderweitig eingereicht und habe auch nicht bereits diese oder eine gleichartige Doktorprüfung endgültig nicht bestanden.

Hiermit erkläre ich, dass ich keine Hilfe von gewerblichen Promotionsberatern bzw. -vermittlern in Anspruch genommen habe und auch künftig nicht nehmen werde.

.....

Ort, Datum, Unterschrift